THESIS FOR THE DEGREE OF DOCTOR OF PHILOSOPHY

# Computational Techniques for Turbulence Generated Noise

MATTIAS BILLSON

Division of Thermo and Fluid Dynamics
CHALMERS UNIVERSITY OF TECHNOLOGY
Göteborg, Sweden, 2004

Computational Techniques for Turbulence Generated Noise
Mattias Billson
ISBN 91-7291-423-8



Doktorsavhandlingar vid Chalmers tekniska högskola
Ny serie nr 2105
ISSN 0346-718X

Division of Thermo and Fluid Dynamics
Chalmers University of Technology
SE-412 96 Göteborg
Sweden
Telephone +46-(0)31-7721000

Printed at Chalmers Reproservice
Göteborg, Sweden

# Computational Techniques for Turbulence Generated Noise

MATTIAS BILLSON
Division of Thermo and Fluid Dynamics
Chalmers University of Technology

## ABSTRACT

Computational techniques for the noise generated by high Mach number subsonic jets have been investigated. The main focus has been on the hybrid noise prediction method SNGR (Stochastic Noise Generation and Radiation), which is based on unsteady source modeling for the inhomogeneous linearized Euler equations (ILEE).

The unsteady source model developments include a time filtering technique and the use of a convective operator to evolve the source field in the inhomogeneous mean flow of a jet. The unsteady source modeling also includes anisotropy in terms of Reynolds stresses as well as length scales.

Inhomogeneous linearized Euler equations in conservative formulation are derived and it is shown that when a proper source field is specified, the proposed ILEE accurately predict the sound generation and propagation in inhomogeneous flows.

The proposed SNGR method has been applied to three high Mach number subsonic jets. It is found that, when properly calibrated, the results from the method in terms of sound pressure level directivity are in good agreement with measurements. The spectral content in the emitted sound however, shows some discrepancies, especially at low frequencies. The model is found to accurately predict the increased sound emission of an increased jet exit Mach number, but that a heated jet could not be properly evaluated due to numerical instabilities.

An anisotropic model of the two-point velocity correlation tensor for homogeneous turbulence is proposed whose functional form is determined by six scalar correlation functions. The model is still under development but is believed to enable more accurate statistical Lighthill's analogy based noise predictions from anisotropic turbulence.

**Keywords:** jet noise, aeroacoustic, SNGR, source terms, linearized Euler, CAA, absorbing boundary conditions, anisotropic, correlation

# List of Publications

This thesis is based on the work contained in the following papers and reports:

I M. Billson, L.-E. Eriksson and L. Davidson,
"Acoustic Source Terms for the Linear Euler Equations on Conservative Form.",
The 8th AIAA/CEAS Aeroacoustics Conference, AIAA 2002-2582
Breckenridge, Colorado, 2002.
Revised and submitted for journal publication

II M. Billson, L.-E. Eriksson and L. Davidson,
"Jet Noise Prediction Using Stochastic Turbulence Modeling",
The 9th AIAA/CEAS Aeroacoustics Conference, AIAA 2003-3282
Hilton Head, South Carolina, 2003.
Revised and submitted for journal publication

III M. Billson, L.-E. Eriksson, L. Davidson and P. Jordan,
"Modeling of Synthetic Anisotropic Turbulence and Its Sound Emission",
The 10th AIAA/CEAS Aeroacoustics Conference, AIAA 2004-2857
Manchester, United Kingdom, 2004.

IV M. Billson, L.-E. Eriksson and L. Davidson,
"Jet Noise Modeling Using Synthetic Anisotropic Turbulence",
The 10th AIAA/CEAS Aeroacoustics Conference, AIAA 2004-3028
Manchester, United Kingdom, 2004.

V M. Billson, L.-E. Eriksson, P. Jordan and L. Davidson
"Anisotropic Formulation of the Velocity Correlation Tensor",
Internal report 04/02, Division of Thermo and Fluid Dynamics,
Department of Mechanical Engineering, Chalmers University of Technology, Göteborg 2004.

## Division of work between paper authors

The work leading up to this thesis has been done in collaboration with other researchers. The respondent is the first author of all papers on which this thesis is based, and the respondent produced all results.

Theoretical and model developments presented in the Papers I, II and IV have been carried out in discussions with the supervisors Lars-Erik Eriksson and Lars Davidson. The theoretical results in Paper III and V are a result of an joint effort between the respondent, Peter Jordan and the supervisors.

# Acknowledgments

Of all the people who have contributed to the fact that this thesis has been written, I firstly want to acknowledge my parents: Thank you for making me do my homework when I was a kid and for encouraging me to move to Göteborg. Most of all, thank you for your support.

This work was carried out at the Division of Thermo and Fluid Dynamics at Chalmers University of Technology in Göteborg. Of all the colleagues at "Termo", the contributions of some people deserve special note.

I would like to thank my supervisors Professor Lars Davidson for all discussions and advise and Professor Lars-Erik Eriksson for sharing some of his profound knowledge in compressible flow with me. The moral support and encouraging talks have also been very much appreciated.

Special thanks also to Niklas Andersson, Jonas Ask and Johan Larsson for all discussions about things neither of us understood at first, but learned together. I know it would have been much tougher if we would not have shared our setbacks and successes.

Associate Professor Gunnar Johansson deserves a special mentioning for the many interesting discussions. The administrative support by Monika Orrbacke, Sandra Arvidsson and Ulla Lindberg-Thieme is also gratefully acknowledged. Finally, I would like to thank all my friends and colleagues at the Division of Thermo and Fluid Dynamics for creating an inspiring working atmosphere.

Financial support from the NFFP (National Flight Research Program) as well as the EU 5th Framework Project JEAN (Jet Exhaust Aerodynamics & Noise), contract number G4RD-CT2000-000313 is gratefully acknowledged.

# Contents

# Nomenclature

*Roman letters*

| | |
|---|---|
| $\mathbf{a}$ | normalized Reynolds stress tensor |
| $a_i$ | coefficients of the symmetric convective scheme |
| $b_i$ | coefficients of the upwinded convective scheme |
| $c_0$ | ambient speed of sound |
| $D$ | diameter |
| $d_i$ | coefficients of upwinding |
| $E(k)$ | turbulence energy spectrum function |
| $e_0$ | total energy |
| $\mathbf{E}$ | rotation matrix |
| $f$ | frequency |
| $f_0$ | fundamental frequency of forcing |
| $f_A$ | amplitude factor |
| $f_L$ | length scale factor |
| $f(r)$ | longitudinal correlation function |
| $f_{12}(r)$ | cross correlation function |
| $f_{13}(r)$ | cross correlation function |
| $f_{23}(r)$ | cross correlation function |
| $f_\tau$ | time scale factor |
| $g(r)$ | transversal correlation function |
| $h_0$ | total enthalpy |
| $h(r)$ | transversal correlation function |
| $k$ | length of $\mathbf{k}$ |
| $k_1$ | lowest modeled wave number |
| $\mathbf{k}$ | wave number |
| $k_e$ | wave number of energy containing eddies |
| $k_\eta$ | Kolmogorov wave number |
| $\overline{k}$ | turbulence kinetic energy |
| $k_N$ | highest modeled wave number |
| $L$ | longitudinal length scale |
| $L_t$ | turbulence length scale |

| | |
|---|---|
| $M$ | Mach number |
| $\mathbf{n}$ | normal vector |
| $p$ | pressure |
| $Q$ | solution vector, $(\rho, \rho u, \rho v, \rho w, \rho e_0)$ |
| $\mathbf{R}$ | rotation matrix |
| $\mathbf{r}$ | separation, $\mathbf{x} - \mathbf{y}$ |
| $R_{ij}$ | $(\mathbf{r})$ velocity correlation tensor (homogeneous turbulence) |
| $R_{1,1}$ | $(\mathbf{x}, r_1, \tau)$ Space-time correlation of $u$ velocity component |
| $R_{ij}$ | $(\mathbf{y}, \mathbf{r})$ velocity correlation tensor |
| $St$ | Strouhal number, $fD_j/U_j$ |
| $t$ | time |
| $T_{ij}$ | Lighthill stress tensor |
| $T_p$ | pairing time |
| $U$ | mean axial velocity |
| $\mathbf{u}$ | velocity vector |
| $\mathbf{u}_t$ | synthesized velocity field (random) |
| $\mathbf{u}_c$ | convection velocity |
| $\hat{u}$ | Fourier mode amplitude |
| $\mathbf{v}_t$ | synthesized velocity field (filtered and convected) |
| $W$ | characteristic variables |
| $x_0$ | start of buffer layer |
| $x_{max}$ | end of buffer layer |
| $\mathbf{x}$ | spatial coordinate |
| $\mathbf{y}$ | spatial coordinate |

*Greek letters*

| | |
|---|---|
| $\Delta$ | cell size |
| $\delta_{ij}$ | Kronecker delta |
| $\delta_\omega(0)$ | initial vorticity thickness |
| $\Delta t$ | time step size |
| $\varepsilon$ | turbulence dissipation rate |
| $\epsilon$ | dissipation parameter |
| $\gamma$ | specific heat ratio |
| $\lambda$ | eigenvalue |
| $\nu$ | molecular viscosity |
| $\omega$ | angular frequency |
| $\psi$ | phase |
| $\rho$ | density |
| $\boldsymbol{\sigma}$ | Fourier mode direction |
| $\sigma$ | $(x)_{max}$ strength of the buffer layer |
| $\tau$ | time separation |

| | |
|---|---|
| $\tau_{ij}$ | viscous stress tensor |
| $\boldsymbol{\tau}$ | Reynolds stress tensor |
| $\tau_t$ | turbulence time scale |
| $\theta$ | space angle |

*Subscripts*

| | |
|---|---|
| $amb$ | ambient |
| $j$ | jet exit condition |
| $m$ | time step |
| $n$ | mode number |

*Superscripts*

| | |
|---|---|
| $*$ | principal axes of Reynolds stress tensor |
| $a$ | anisotropic |
| $iso$ | isotropic |
| $m$ | time step number in time filter |
| $T$ | transpose |
| $\bar{\cdot}$ | time-average |
| $\prime$ | fluctuation related to time-average |
| $\tilde{\cdot}$ | Favre time-average or rotated coordinate system |
| $\prime\prime$ | fluctuation related to Favre time-average |

# Chapter 1

# Introduction

The research area of aeroacoustics started in the era of the first jet engine propelled aircraft. It was realized that with the new types of engines, the jet engines, there was a potential noise hazard. The first turbojet engines were produced for military airplanes and in that application the noise was not really of such a large concern. The main goal was to deliver thrust and the jet engines did that better than any other engine. When jet engines were to be used for civil aircraft however the noise issue became an important factor. With improved technology giving larger and more powerful power plants for commercial aircraft the noise levels increased rapidly. The noise emitted at takeoff from a commercial aircraft in the 60's was more than the combined shouting power of the earth's population.

The research in the area of jet noise began in the late forties and it was in 1952 that the real breakthrough came, when Sir James Lighthill published the first of his two-part paper on aerodynamically generated sound. The second paper followed in 1954.[1,2] The approach of Lighthill was to try to find the sources of sound in turbulent flow. This was achieved in terms of an acoustic analogy where the basic idea was to rewrite the compressible equations for fluid motion in such a way that the left-hand side consisted of the second-order linear wave equation governing sound propagation in a homogeneous medium at rest. All other terms were moved to the right-hand side and considered as sources. The resulting wave equation with source term is

$$\frac{\partial^2 \rho}{\partial t^2} + c_0^2 \frac{\partial^2 \rho}{\partial x_j \partial x_j} = \frac{\partial^2 T_{ij}}{\partial x_i \partial x_j} \tag{1.1}$$

where $\rho$ is the density, $c_0$ is the ambient speed of sound and $T_{ij} = \rho v_i v_j + (p - \rho c_0^2)\delta_{ij} - \tau_{ij}$ is the Lighthill stress tensor containing all non-

linearities, and $v_i$, $p$, $\tau_{ij}$ and $\delta_{ij}$ are the velocity, pressure, viscous stress tensor and Kronecker delta respectively. The right-hand side in equation 1.1 involves second spatial derivatives of products of velocities resulting in the famous quadrupole source distribution of turbulence.[1,3]

Lighthill managed to find a formal integral solution to the wave equation 1.1 by using a Green's function. One of the major assumptions in the solution to the acoustic analogy is that acoustic propagation is assumed to take place in a homogeneous medium at rest. This means that there can be no solid bodies present and that refraction of sound due to shear is not taken into account unless these effects are inherent in the source field. This means that any effect of inhomogeneity in the flow must be represented by the source field which is used to evaluate the source terms since this is not part of the wave operator in equation 1.1. Extensions of Lighthill's acoustic analogy to incorporate the effect of solid surfaces in the flow was published by Curle[4] in 1955 and later also by Ffowcs Williams and Hawkins[5] among others.[6–8] The interaction of the turbulence with the surfaces introduces sources which were found to have a dipole[1,3] character which is illustrated by a numerical example by Pérot *et al.*[9]

Lighthill[1] also included the effect of convected turbulence on the directivity of the radiated sound. The theory predicts that there is an amplification of the emitted sound in the direction of the convection and a reduction in the opposite direction. In the case of a subsonic jet at high Mach number or a supersonic jet this effect is an important factor of the sound field directivity. This convective amplification is singular though at sonic speeds, and Ffowcs Williams[10] refined the theory such that the singularity was removed.

The power of Lighthill's analogy based methods is the possibility to use statistical models of the sound generation and emission. This is quite remarkable since sound generation and propagation is inherently time dependent. The noise generation is modeled based on correlations and estimations of the scales in the turbulent region and the propagation is solved as an integral equation. For applications of these methods, see Refs. [3, 9, 11–16]. The work done on statistical methods in this project is limited to an anisotropic model for the two-point velocity correlation tensor. The two-point velocity correlation tensor is central in statistical Lighthill's analogy based methods since it represents the spatial structure of the turbulence. A model of the anisotropy concept in terms of length scale is also presented.

Another important effect in inhomogeneous flows is the refraction of the generated sound. When the sound is propagating out of the jet to

the far-field the local speed of a wave-front will be a function of both the thermodynamic speed of sound and the local convection velocity. In the down-stream direction, the wave-front will tend to bend out from the jet since the local speed of the wave at location $B$ is higher than that in $A$, see figure 1.1. This makes the sound refract out from the jet and cause a cone of silence in the axial direction, especially for high frequencies which are more affected by spatial variations in the mean flow. This effect will be amplified if the jet is heated compared to the surrounding. In 1974 Lilley[17] developed an analogy in which the refractional effects were included in the wave operator. Some effects of inhomogeneity of the flow were included in the wave operator and were not required to be specified in the source terms. This had a price though, the simplicity of the analogy was lost and the general solution could not be found by an integral method.

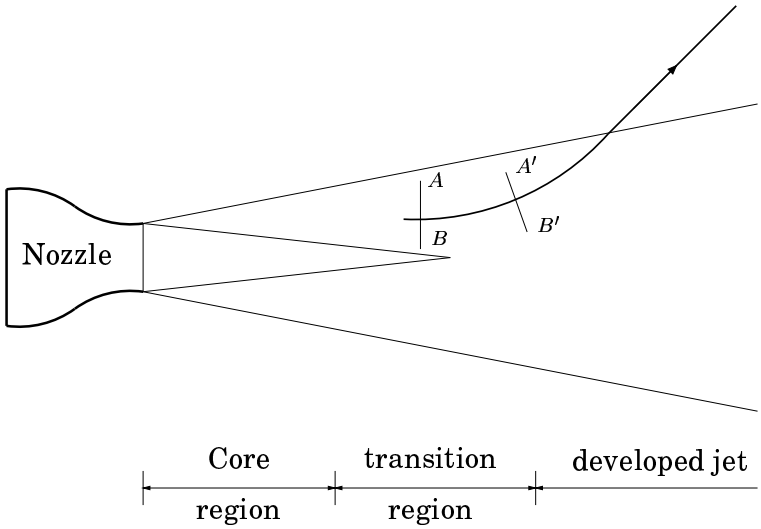


Figure 1.1: Refraction of sound wave.

The general understanding at the time was that turbulence consisted of small eddies which were more or less randomly distributed. The source of noise in turbulence was of course believed to be the same eddies. At the beginning of the seventies the discovery of large turbulence structures in jets and free shear flows changed the focus in the aeroacoustic community. The large turbulence structures were found to dominate the overall dynamics and mixing of free shear flows and it was also shown that they are a strong source of sound in supersonic jets.[18] However, these large structures are not as important for the sound generation in subsonic jets. For further reading on the impor-

tance of large turbulence structures in jet noise, see Tam.[19] If a supersonic jet is imperfectly expanded, shock cells will form close to the jet exit. There are two additional sources of sound in jets that can be identified in the presence of shock cells. These are screech tones and broadband shock associated noise, see Ref. [20] for references. Since these sources are associated with supersonic jets they are not within the scope of this work.

Until the nineties, all estimations of jet noise were restricted to analogies with solutions based on dimensional arguments and statistical information. Rapid increase in the available computer power opened for the possibility to directly solve the compressible Navier-Stokes equations using Direct Numerical Simulations (DNS) or Large Eddy Simulations (LES). Solving the compressible Navier-Stokes equations (or simplifications thereof) with the aim of predicting sound generation and propagation is called Computational Aeroacoustics (CAA). Well-performed DNS and LES simulations are very valuable tools for the understanding of noise generated by turbulence and inhomogeneous propagation of the generated noise. They capture flow-acoustic interaction, refraction, diffraction, presence of solid objects, convectional and other effects that may affect the flow and sound field. It is not feasible yet though, to use these methods in industrial applications, even if LES might be used in a near future given that the computer development continues as it has in recent years.

But until then it is worth while to continue to develop methods for jet noise estimations which are less computationally intensive. A method called SNGR or Stochastic Noise Generation and Radiation method has been developed by Bechara *et al.*,[21] Bailly *et al.*[22] and Bailly and Juvé.[23] In stead of being based on statistical estimations of the turbulence to be used for an integral solution of an acoustic analogy it is based on unsteady source modeling. These sources are used to evaluate source terms to an appropriate equation governing acoustic wave propagation which is solved on a computational grid for the final sound prediction. By solving the wave operator on a computational grid to extend the acoustic solution from the near-field to the far-field instead of relying on an integral solution, the use of a simple wave operator such as the linear homogeneous wave equation (which does not include effects of inhomogeneities such as refraction) is obsolete. The most general approach is to use the linearized versions of the first principles governing fluid flow as a wave operator. The inhomogeneous linearized Euler equations are therefore used as wave operator in the original SNGR formulations,[21–23] where the terminology inhomo-

geneous linearized Euler equations refers to that the equations have source terms. The SNGR method of Bailly and Juvé[23] has been further developed in the present work. The changes concern the methods of introducing time dependence and convection to the synthesized turbulence. The method has also been changed such that the synthesized turbulence can have anisotropy in both velocity and length scales. The proposed method has been applied to both generic test cases and high Mach number subsonic jet flows and the results have when possible been validated to measurements and other prediction methods.

Common for all methods to perform an aeroacoustic noise prediction based on solving the discretized flow equations is that there are very high requirements for the numerical methods. The requirements in a CAA computation as compared to a CFD (Computational Fluid Dynamics) computation are stricter in every aspect. The main reason for this is related to the scale disparity between the turbulence scales and the acoustic scales. The smallest turbulent scales must be resolved with high accuracy at the same time as the largest acoustic scales must have room to propagate out from the source region to the surrounding ambient region in the computational domain. On the same domain the smallest acoustic scales must be accurately propagated without numerical dispersion or dissipation errors. The numerical scheme must in order to meet these requirements have a very high fidelity and the grid resolution is still high in the whole computational domain with a very large degree-of-freedom in the problem as a result. The requirements of the free-field boundary conditions are also much higher in CAA compared to CFD. The free-field boundary conditions must have very high level of absorption of out going waves in order to simulate the non-existence of the computational boundary. As a consequence, a large portion of the work related to CAA (and in this work) is on ensuring that the numerics are at the state of the art and that the number of unknown numerical factors are kept to a minimum.

# Chapter 2

# Goals and Motivation

The goals of the present work have evolved during the work process and the level of ambition has been adjusted to the level of progress. The main original goals were however:

- To investigate the possibility to develop a noise prediction method for turbulent jets which is considerably less computationally costly than LES and DNS and more flexible and general than existing statistical methods.
- To increase the understanding of the important aspects of performing a noise prediction when using CAA methods both in terms of numerical requirements and in the sound generation process.

The motivation of the project is the renewed focus on aeroacoustics in the aircraft and jet engine industry. This interest is driven by stricter legislative standards and harder competition for the best concepts both in terms of efficiency and overall noise levels from commercial jet airliners. Jet exhaust related noise is a major noise source from a modern jet aircraft at take-off, and any progress in prediction methods which can be applied to industrial size jets would be a valuable tool in the development of future more quiet jet engines.

# Chapter 3

# The SNGR Method

This chapter is focused on describing the proposed Stochastic Noise Generation and Radiation (SNGR) method. A short overview of the method will first be given followed by a more detailed presentation of the individual steps in the following sections. Some technical derivations and definitions are left out and referred to in the Appendix or in the papers, mainly Papers II-IV.[24–26]

## 3.1 Stochastic Noise Generation and Radiation – Overview

The SNGR model applied to a jet is performed in three steps. These are:

**step 1.** A Reynolds-Averaged Navier-Stokes solution of a compressible turbulent jet is calculated using, for example, a $k-\varepsilon$ turbulence model.

**step 2.** An unsteady turbulent velocity field with the same local turbulence kinetic energy, time scale and length scale as the RANS solution is generated using random Fourier modes.

**step 3.** The inhomogeneous linearized Euler equations (ILEE) are solved using the mean flow field computed in step (1) as mean flow solution. Source terms derived in a similar way as for Lighthill's wave equation are evaluated using the turbulence field generated in step (2). The linearized Euler equations then govern the propagation of sound from the turbulent field to the surrounding farfield.

The three steps in the SNGR method will be described in the following sections.

## 3.2 Reynolds Averaged Navier-Stokes Solution

The Reynolds Averaged Navier-Stokes solution of the flow has two purposes. One is to serve as the reference solution in the linearized Euler equations in step (3) of the SNGR method. As such the RANS solution is important for the proper development of the solution to the linearized Euler equations. Effects of convection and refraction in the mean shear of the RANS can strongly affect the propagation of the acoustic waves. The other purpose is that the source field generated in step (2) of the SNGR method will be generated based on the solution of the RANS equations. The spatial and temporal distribution of energy in the generated turbulence in step (2) will be based on the turbulence kinetic energy and dissipation rate. The generated velocity field will also be convected by the velocity field from the RANS solution.

The standard $k-\varepsilon$ RANS model has been used in the jet noise simulations. The simulations have been performed by Eriksson[27] in axisymmetric variables. The reason for using an axisymmetric mesh for the RANS computations is that the computational domain could be extended to several hundred jet diameters from the nozzle exit. This is required if the proper development of the jet is to be achieved in the RANS simulations. The RANS solutions of the jets are in good agreement with measurements and show typical standard $k-\varepsilon$ RANS model behavior for a round jet.

The axisymmetric solution was then transferred to the 3D computational mesh used in the linearized Euler computations. Each of the computational cells in the 3D mesh was split into $10 \times 10 \times 10$ subvolumes. The location of the center of each sub-volume $(\overline{x}, \overline{y}, \overline{z})$ was expressed in axisymmetric coordinates $(\overline{x}, \overline{r})$ and the solution in this sub-volume was interpolated from the axisymmetric RANS solution.

The interpolation of the solution in the axisymmetric mesh was based on a cell-to-node transformation of the solution where the volume averaged solution was transfered to the grid nodes. The solution in the subvolume was then interpolated within a cell by using the node-based solution in the axisymmetric mesh. The contribution to the solution from each sub-volume to the average solution in the whole 3D cell solution

was accumulated using volume-weighted accumulation. This ensured a minimum of error in the conservation of mass, momentum and energy in the transformation of the solution from the axisymmetric mesh to the full 3D mesh.

The RANS solution is also used in combination with Boussinesq assumption to predict the Reynolds stress anisotropy which is used as input for the anisotropic method to generate synthesized turbulence.

## 3.3 Generation of Synthesized Turbulence

This section concerns the generation of an unsteady turbulent velocity field, i.e. step (2) in the SNGR method. A time-space turbulent velocity field can be simulated using random Fourier modes. This was proposed by Kraichnan[28] and Karweit *et al.*[29] Later Bechara *et al.*,[21] Bailly *et al.*[22] and Bailly and Juvé[23] used this to generate synthesized turbulence in the framework of the SNGR method.

The synthesis of velocity fields in this work is based on the same approach as in the above mentioned references. The present method does however differ in the way time dependence and convection effects are introduced. This will be shown later in this section. First the generation of a space distribution of the synthesized turbulence is presented. A random velocity field can be constructed as a sum of Fourier modes

$$\mathbf{u}_t(\mathbf{x}) = 2\sum_{n=1}^{N} \hat{u}_n \cos(\mathbf{k}_n \cdot \mathbf{x} + \psi_n)\boldsymbol{\sigma}_n \tag{3.1}$$

where $\hat{u}_n$, $\psi_n$ and $\boldsymbol{\sigma}_n$ are amplitude, phase and direction of the $n^{th}$ Fourier mode. The direction $\boldsymbol{\sigma}_n$ has length $|\boldsymbol{\sigma}_n| = 1$. Figure 3.1 shows the geometry of the $n^{th}$ mode in wave space.

The orientation of vector $\mathbf{k}_n$ is chosen randomly on a sphere with radius $k_n$. This to ensure isotropy of the generated velocity field. By the assumption of incompressibility the continuity equation gives the following relation

$$\mathbf{k}_n \cdot \boldsymbol{\sigma}_n \equiv 0 \qquad \text{for all} \qquad n \tag{3.2}$$

The wave number vector $\mathbf{k}_n$ and the spatial direction $\boldsymbol{\sigma}_n$ of the $n^{th}$ mode are thus perpendicular.

The space angles $\varphi_n$, $\alpha_n$, $\theta_n$ and the phase $\psi_n$ are chosen randomly with probability functions given in table 3.1. The probability function

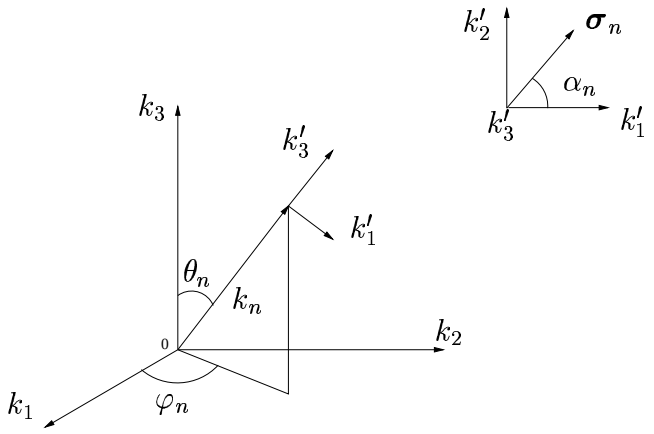


Figure 3.1: Geometry in wave-space for the $n^{th}$ mode.

| | |
|---|---|
| $p(\varphi_n) = 1/(2\pi)$ | $0 \leq \varphi_n \leq 2\pi$ |
| $p(\psi_n) = 1/(2\pi)$ | $0 \leq \psi_n \leq 2\pi$ |
| $p(\theta_n) = (1/2)\sin(\theta)$ | $0 \leq \theta_n \leq \pi$ |
| $p(\alpha_n) = 1/(2\pi)$ | $0 \leq \alpha_n \leq 2\pi$ |

Table 3.1: Probability distributions of random variables.

of $\theta$, $p(\theta_n) = 1/2\sin(\theta)$ is chosen such that the distribution of the direction of $\mathbf{k}_n$ is uniform on the surface of a sphere, see figure 3.2, i.e. the probability of a randomly selected direction is the same for all surface elements $\mathrm{dA}$.

The amplitude $\hat{u}_n$ of each mode in equation 3.1 is computed from the turbulence energy spectrum function $E(k_n)$ corresponding to the energy spectrum for isotropic turbulence. This gives

$$\hat{u}_n = \sqrt{E(k_n)\Delta k_n} \tag{3.3}$$

where $\Delta k_n$ is a small interval in the spectrum located at $k_n$, see figure 3.3. A model spectrum is used to simulate the shape of the energy spectrum for isotropic turbulence. In this way the sum of the squares of $\hat{u}_n$ over all $n$ is equal to the total turbulence kinetic energy

$$\overline{k} = \sum_{n=1}^{N} \hat{u}_n^2 \tag{3.4}$$

The spectrum $E(k_n)$ is subdivided with a linear distribution as

$$k_n = k_1 + dk_l^{n-1} \quad \text{for} \quad n = 1, 2, \ldots, N \tag{3.5}$$

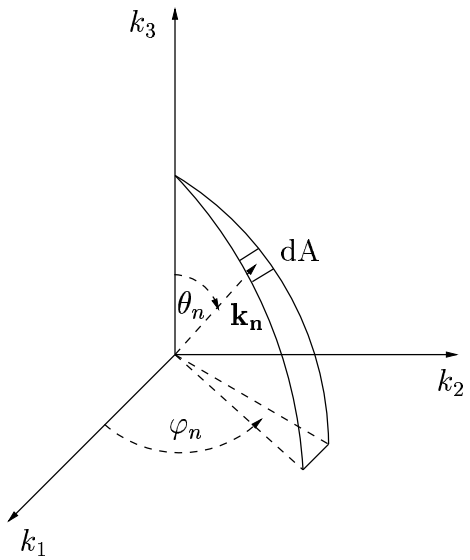


Figure 3.2: The probability of a randomly selected direction of a wave in wave-space is the same for all $\mathrm{dA}$ on the shell of a sphere.

where

$$dk_l = \frac{(k_N - k_1)}{N - 1} \tag{3.6}$$

The energy spectrum for isotropic turbulence is simulated by a modified von Kármán-Pao spectrum

$$E(k) = \alpha \frac{u'^2}{k_e} \frac{(k/k_e)^4}{[1 + (k/k_e)^2]^{17/6}} e^{[-2(k/k_\eta)^2]} \tag{3.7}$$

where $k$ is the wave number, $k_\eta = \varepsilon^{1/4}\nu^{-3/4}$ is the Kolmogorov wave number, $\nu$ is the molecular viscosity and $\varepsilon$ is the turbulence dissipation rate. $u'^2$ is the r.m.s. value of the velocity fluctuations corresponding to the turbulent kinetic energy, $u'^2 = 2\overline{k}/3$. There are two free parameters in equation 3.7. The numerical constant $\alpha$ which determines the kinetic energy of the spectrum and the wave number $k_e$ corresponding to the most energy containing eddies at the peak in the spectrum. The available information from the RANS solution is the turbulence kinetic energy $\overline{k}$, and the dissipation rate $\varepsilon$. These are used to determine $\alpha$ and $k_e$ and thereby the shape of the spectrum and the distribution of energy over different wave numbers. The numerical constant $\alpha$ can be determined by the requirement that the integral of the energy spectrum, equation 3.7, over all wave numbers should be equal to the total turbulent kinetic energy

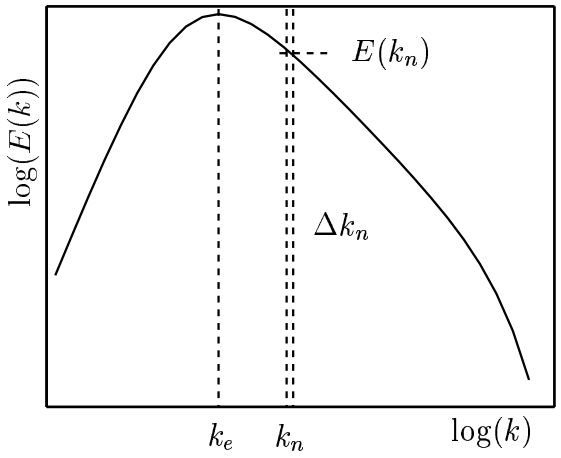


Figure 3.3: Model energy spectrum

$$\overline{k} = \int_0^\infty E(k)dk \tag{3.8}$$

Since equation 3.7 is derived for infinite Reynolds number $\alpha$ can be found independently of $k_e$ by integrating equation 3.8 to get

$$\alpha = \frac{4}{\sqrt{\pi}} \frac{\Gamma(17/6)}{\Gamma(1/3)} \simeq 1.45276 \tag{3.9}$$

The turbulence length scale from the RANS solution is defined as

$$L_t = f_L \frac{\overline{k}^{3/2}}{\varepsilon} \tag{3.10}$$

where $f_L$ is the length scale factor used to calibrate the length scale of the synthesized turbulence. Assuming that the length scale from the RANS solution is the same as the integral length scale for isotropic turbulence gives the following relation

$$L_t = \frac{\pi}{2u'^2} \int_0^\infty \frac{E(k)}{k} dk \tag{3.11}$$

which is used to determine the wave number $k_e$ corresponding to the most energetic length scales. The relation of $k_e$ to $L_t$ and $\alpha$ is then

$$k_e = \frac{9\pi}{55} \frac{\alpha}{L_t} \tag{3.12}$$

where $\alpha$ is given in equation 3.9 and $L_t$ is obtained from the RANS solution.

### 3.3.1 Time Dependence

Using equation 3.1 together with the other relations in the previous section a single realization of a turbulent velocity field is synthesized. A prescribed time evolution of the turbulence is introduced through a time filter. This is done in the following way. First generate a realization of the turbulent velocity field $\mathbf{u}_t^m(\mathbf{x})$ (using equation 3.1) where superscript $(\cdot)^m$ denotes time step. Each generated field $\mathbf{u}_t^m(\mathbf{x})$ for all $1 < m < N$ is independent of the others and they have a zero statistical mean in time. In other words the generated velocity field is locally white noise in time. A new turbulent velocity field can then be computed via the filter equation (Paper III and IV[25,26])

$$\mathbf{v}_t^m(\mathbf{x}) = a\mathbf{v}_t^{m-1}(\mathbf{x}) + b(\mathbf{u}_t^m(\mathbf{x}) + \mathbf{u}_t^{m-1}(\mathbf{x})) \tag{3.13}$$

where $a = \exp(-\Delta t/\tau_t)$ and $b = f_A\sqrt{(1-a)/2}$. $\tau_t$ is referred to as the time scale and defines the time separation for which the autocorrelation function is reduced to $\exp(-1)$. The factor $f_A$ is an amplitude factor used to modify the level of the filtered turbulent field $\mathbf{v}_t^m(\mathbf{x})$. When $f_A$ is equal to one the expression for $b$ ensures that the root mean square of $\mathbf{v}_t^m(\mathbf{x})$ is the same as for $\mathbf{u}_t^m(\mathbf{x})$. Typically $a$ is a number close to one and $b$ close to zero. The time scale of the filter in equation 3.13 is computed from the RANS solution as

$$\tau_t = f_\tau \frac{\overline{k}}{\varepsilon} \tag{3.14}$$

where the time scale factor $f_\tau$ is introduced for the possibility to modify the time scale.

Figure 3.4 shows a $1/3$ octave power spectral density of $u$-velocity component computed from synthesized turbulence filtered using the equation 3.13. The time scale in the spectrum is $\tau_t = 0.001$ s. Also shown is the analytical discrete Fourier transform of the autocorrelation of the filter equation 3.13. Both curves show a near constant level for low frequencies with a quadratic slope for higher frequencies. At the resolution limit the energy goes to zero, i.e. there are no odd-even fluctuations in the filtered velocities. Shown is also the $\omega^{-5/3}$ line for high frequencies predicted by isotropic turbulence theory.[30]

### 3.3.2 Convection Operator

To account for convection of the generated turbulent field $\mathbf{v}_t^m(\mathbf{x})$ a simple convection equation is solved for $\mathbf{v}_t^{m-1}(\mathbf{x})$

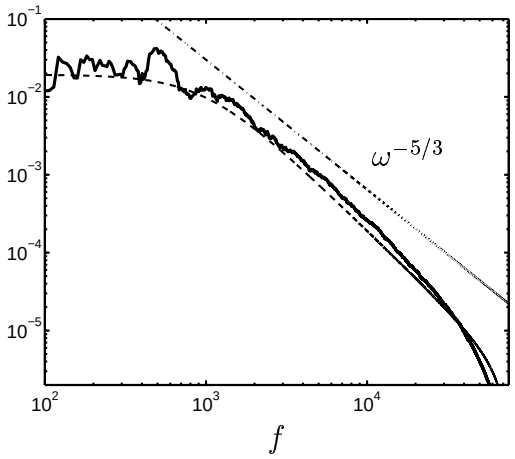


Figure 3.4: $1/3$ octave power spectral density of $u$. Solid line: synthesized velocity; dashed line: analytical expression for equation 3.13; dash-dotted line: $\omega^{-5/3}$ line

$$\frac{\partial(\overline{\rho}\mathbf{v}_t^{m-1})}{\partial t} + \frac{\partial(\overline{\rho u_j}\mathbf{v}_t^{m-1})}{\partial x_j} = 0 \tag{3.15}$$

before it is used in equation 3.13. The convected and time filtered velocity field $\mathbf{v}_t^m(\mathbf{x})$ is then used when evaluating the source terms in step (3) in the SNGR method.

The convective operator and the time filter (equations 3.15 and 3.13) were introduced to avoid a problem of spatial de-correlation in the previous formulations of the generation of synthesized turbulence.[22,23,28,31] In these studies the synthesized turbulent velocity was given by

$$\mathbf{u}_t(\mathbf{x},t) = 2\sum_{n=1}^{N} \hat{u}_n \cos(\mathbf{k}_n \cdot (\mathbf{x} - t\mathbf{u}_c) + \psi_n + \omega_n t)\boldsymbol{\sigma}_n \tag{3.16}$$

i.e. time dependence and convection were introduced directly in the Fourier modes. In this expression $\mathbf{u}_c$ is the local convection velocity computed in the RANS solution, and $\omega_n$ is the angular frequency of the $n^{th}$ generated mode. Batten *et al.*[31] reported that the convective argument $(\mathbf{x} - t\mathbf{u}_c)$ causes spatial de-correlation of the synthesized velocity field in shear flows. The reason for this is that the local convection velocity $\mathbf{u}_c$ will vary cross the shear layer so that $\mathbf{x} - t\mathbf{u}_c$ becomes very different for points close to each other as time $t$ in the simulation becomes large. This de-correlation does not occur in the present method since the convected velocity field $\mathbf{v}_t^{m-1}(\mathbf{x})$ in equation 3.15 is continuously filtered in the time filter operator (equation 3.13). The random

velocity fields $\mathbf{u}_t^m(\mathbf{x})$ used as input in equation 3.13 are well correlated in space for all times since they do not include the de-correlating convection term $(\mathbf{x} - t\mathbf{u}_c)$. The total effect of the convection operator and the time filter is a well correlated synthesized velocity field even in shear flows, which is shown for high Mach number jets in Papers II and IV.[24,26]

### 3.3.3 Anisotropy

The method to introduce anisotropy in the generation of synthesized turbulence is fully described in Paper III,[25] and only the final expressions are presented here.

The goal is to generate a velocity field with an anisotropy specified by a model Reynolds stress tensor $\boldsymbol{\tau}$. The idea is to introduce anisotropy to the synthesized velocity field in the principal axes of the model stress tensor since in these axes, the cross-correlation components in the tensor are all zero and the anisotropy of the flow is determined by the normal components. The generated anisotropic velocity field is then rotated from the principal axes of the model stress tensor back into the normal coordinate system.

Let superscript $(\cdot)^*$ denote a variable that is expressed in a coordinate system aligned with the principal axes of a model Reynolds stress tensor $\boldsymbol{\tau}$. An anisotropic velocity field $\mathbf{u}^{a*}(\mathbf{x}^*)$ is then generated (cf. equation 3.1) by the equation

$$\mathbf{u}^{a*}(\mathbf{x}^*) = 2\sum_{n=1}^{N} \hat{u}_n \cos(\mathbf{k}_n^{a*} \cdot \mathbf{x}^* + \psi_n)\boldsymbol{\sigma}_n^{a*} \tag{3.17}$$

where the direction of the anisotropic velocity component $\hat{u}_n$ is

$$\boldsymbol{\sigma}_n^{a*} = \mathbf{a}^{*1/2}\boldsymbol{\sigma}_n^* \quad , \quad |\boldsymbol{\sigma}_n^{a*}| \neq 1 \tag{3.18}$$

The tensor

$$\mathbf{a}^* = -\frac{3}{2}\frac{\boldsymbol{\tau}}{\overline{\overline{\rho k}}} \tag{3.19}$$

is the normalized Reynolds stress tensor in the principal coordinate system. The wave number $\mathbf{k}_n^{a*}$ in equation 3.17 is defined by

$$\mathbf{k}_n^{a*} = \mathbf{a}^{*-1/2}\mathbf{k}_n^* \tag{3.20}$$

This modified wave number is introduced to make sure that the resulting velocity field will have zero divergence for a homogeneous anisotropic field, i.e. $\mathbf{k}_n^{a*} \cdot \boldsymbol{\sigma}_n^{a*} = 0$.

The final expression for the anisotropic velocity field expressed in the normal coordinate system is then computed by

$$\mathbf{u}^a(\mathbf{x}) = \mathbf{R}\mathbf{u}^{a*}(\mathbf{x}^*) \tag{3.21}$$

where $\mathbf{R}$ is the rotation matrix that diagonalizes the stress tensor $\boldsymbol{\tau}$. The resulting stress tensor associated with velocity field $\mathbf{u}^a(\mathbf{x})$ is the same as the model Reynolds stress tensor $\boldsymbol{\tau}$. The rotation matrix $\mathbf{R}$ consists of the eigenvectors of the model stress tensor $\boldsymbol{\tau}$ and the normalized stress tensor expressed in the principal axes $\mathbf{a}^*$ is a diagonal tensor with the normalized eigenvalues of $\boldsymbol{\tau}$ in the diagonal. Time dependence and convection of the anisotropic turbulence velocity field in equation 3.17 is introduced in the same way as in the isotropic case.

The proposed method to generate anisotropic turbulence has been used in a test case which is described in section 5.4.2 and in Paper III[25] as well as for turbulent high Mach number subsonic jets in Paper IV[26] which are presented in section 5.5.

## 3.4 Inhomogeneous Linearized Euler Equations, ILEE

The third step in the SNGR method is to compute the sound field associated with the synthesized turbulence generated in step (2). An appropriate system of equations must be chosen which governs acoustic wave propagation and has source terms representing turbulence. One could for example use the Lighthill equation,[1] which is derived from the Navier-Stokes equations without assumptions. Properly computed source terms would give an accurate prediction of the sound field associated with the source field. Since Lighthill's equation is the linear wave equation for a homogeneous medium at rest all effects of inhomogeneity such as the presence of solid boundaries or shear as well as non-linear effects must be specified by the source terms.

Following the original presentation by Bechara et al.,[21] the inhomogeneous linearized Euler equations are used as wave operator for the acoustic prediction in the present work. The formulations used in [21–23] were based on primitive formulations of the ILEE whereas the conservative formulation is used in the present work. The advantage

of the ILEE compared to the Lighthill equation is that effects of inhomogeneities are retained in the wave operator and the source terms do not need to describe all such effects.

### 3.4.1 Conservative Formulation

The inhomogeneous linearized Euler equations used in the present SNGR method are based on conservative formulation using $(\rho', (\rho u)', (\rho v)', (\rho w)', (\rho e_0)')$ as solution variables. The derivation of these equations is presented in Paper I[32] and only the final expression is given here. The linearized continuity equation, inhomogeneous momentum equations and inhomogeneous energy equation can in conservative formulation be written as

$$\begin{aligned}
&\frac{\partial \rho'}{\partial t} + \frac{\partial (\rho u_j)'}{\partial x_j} = 0 \\
&\frac{\partial (\rho u_i)'}{\partial t} + \frac{\partial}{\partial x_j}(\widetilde{u}_j(\rho u_i)' + \widetilde{u}_i(\rho u_j)' - \rho'\widetilde{u}_i\widetilde{u}_j + p'\delta_{ij}) = \\
&-\frac{\partial}{\partial x_j}(\rho u_i'' u_j'' - \overline{\rho u_i'' u_j''}) \\
&\frac{\partial (\rho e_0)'}{\partial t} + \frac{\partial}{\partial x_j}(\widetilde{h}_0(\rho u_j)' + \widetilde{u}_j(\rho h_0)' - \rho'\widetilde{h}_0\widetilde{u}_j) = \\
&-\frac{\partial}{\partial x_j}(\rho h_0'' u_j'' - \overline{\rho h_0'' u_j''})
\end{aligned} \tag{3.22}$$

where over-line $(\bar{\cdot})$ and prime $(\cdot')$ denote time-average and associated fluctuation respectively. Tilde $(\widetilde{\cdot})$ denotes Favre time-average and the double prime $(\cdot'')$ is the associated fluctuation. The total enthalpy and pressure in equation 3.22 are introduced to enable a short notation and the decompositions of total enthalpy and the pressure into averages and fluctuations are consistent with the decompositions of the primary solution variables.[32]

The inhomogeneous linearized Euler equations above, equations 3.22, have been derived from the Euler equations without approximations or assumptions of the nature of the flow. The equations above are in fact still the non-linear Euler equations. But if one argue that the terms on the right hand side of equations 3.22 are in some way known and considered as source terms, then the equations on the left hand side are the linearized Euler equations. The right hand side could for example

be given by a Large Eddy Simulation or a Direct Numerical Simulation which also would provide the reference solution $(\overline{\rho}, \overline{\rho}\widetilde{u}, \overline{\rho}\widetilde{v}, \overline{\rho}\widetilde{w}, \overline{\rho}\widetilde{e_0})$ for the linearized Euler equations. The equations 3.22 would then be an analogy for acoustic generation and radiation. In the SNGR method the reference solution $(\overline{\rho}, \overline{\rho}\widetilde{u}, \overline{\rho}\widetilde{v}, \overline{\rho}\widetilde{w}, \overline{\rho}\widetilde{e_0})$ is given from the solution of the RANS equations (step (1)), and the source terms (right hand side in equation 3.22) are evaluated from the synthesized turbulence in step (2).

### 3.4.2 Stability in Shear Flows

Free shear flows can be categorized based on in which way they show a tendency for instability, see Huerre and Monkewitz[33] . One of these categories of unstable flows is the convectively unstable flow. A disturbance in a convectively unstable flow grows in time but is convected downstream and thus leaving the starting point undisturbed. If the flow is homogeneous in the stream-wise direction this instability exists for all downstream positions. In developing flows there may be a region of local convective instability with surrounding stable regions. This can be called a local convective instability region. Unheated turbulent jets with uniform density are examples of flows which in the initial shear layers experience local convective instabilities.

For the non-linear flow-equations the instabilities reach a finite limit through non-linearity and undergo transition to turbulence. For linearized flow equations there is no non-linearity which limits the amplitude through transition. It is only the convection and locality of the instability that keeps the amplitude of the disturbance finite. The disturbances can reach quite large values before they are convected out from the local convectively unstable region. By convection these disturbances are transported through the computational domain until they reach the outflow boundary. Once there they pose a considerable challenge for the outflow boundary condition, see sections 4.4.3 and 5.1.

For a noise prediction simulation the instabilities are of concern due to coupling between vorticity waves and acoustic waves in shear flows. The instabilities are mostly of vortical structure and the disturbances are convected downstream by the mean flow. But if there is a coupling of the vorticity waves with acoustic waves the disturbances will be able to propagate out from the region of the original disturbances as acoustic waves. If the amplitudes of these acoustic waves are large they can dominate the numerical solution and make evaluation of the flow difficult.

In jet simulations it has been found that the most unstable modes are at relatively low frequencies. Numerical simulations indicate that instabilities are at frequencies lower than that of the dominating sound generation. The most unstable modes in the simulations in the present work have been found to have Strouhal numbers $St = fD_j/U_j$ lower than $0.1$ whereas the dominating frequencies of the emitted sound of high Mach number subsonic jets are above $St = 0.1$. This opens for the possibility to filter the solution of the emitted sound below a specified frequency. This is possible since the system of equations is linear and there is thus no spectral transfer of energy between different frequencies. The far-field jet noise predictions presented in the present work have been filtered in this manner to avoid the effect of these low frequency instabilities. This has been done as a last resort to be able to evaluate the far-field acoustic data.

There has however been some progress in efforts to make the LEE stable in shear flows. The approaches have been focused on decoupling vorticity and acoustic waves. For example Bogey *et al.*[34] did this in a formulation of the linearized Euler equations using primitive variables by discarding spatial derivatives of the reference solution. This decouples the acoustic and vorticity waves and has a stabilizing effect on the solution, see Bogey *et al.*[34] A less aggressive modification of the governing equations has been proposed by Zhang *et al.*[35] For axisymmetric simulations in ducted flows in the $x$-direction they discarded the derivative of the axial mean velocity component in the radial direction, $\partial\overline{u}/\partial y$. This also had a stabilizing effect on the disturbances. Both types of modifications of the governing equations in [34] and [35] do however introduce non-conservativeness of mass, momentum and energy. And even if both [34] and [35] have reported good results for the investigated flows by using these modified equations, it is unclear which effect these modifications have on the solution to the equations in other flows than those presented.

Ewert and Schröder[36] have performed a more elaborate change of the linearized Euler equations. By splitting the solution variables in the equations into an incompressible vortical part and a compressible rotation-free part the vorticity and acoustic modes have been decoupled. The resulting equations have been shown[36,37] to be stable even for globally unstable flows.

An brief investigation of the effects of modifying the linearized Euler equations has been performed in the present work. The test case and the results are fully presented in section 5.3. It is just mentioned here that the results indicate that modifying the equations may introduce

errors in the refraction of acoustic waves in inhomogeneous flows.

# Chapter 4

# Numerical Method

## 4.1 Linearized Euler Equations Solver

The solver for the linearized Euler equations is based on the G3D[38] series of codes developed by Lars-Erik Eriksson at Volvo Aero Corporation. These codes solve compressible flow equations on conservative form on a general structured boundary-fitted, curve-linear non-orthogonal multi-block mesh.

The solver in the present work is an extended version of a code for solving the linearized Euler equations in CFD applications. The developments consist of increased numerical accuracy required for Computational Aeroacoustics (CAA). In the present state the code uses an explicit four-stage fourth order Runge-Kutta time marching technique. The convective fluxes are evaluated using a six-point finite volume stencil. Upwinding of the convective fluxes based on characteristic variables is used to ensure numerical stability. The code has been parallelized using MPI (Message Passing Interface) to make parallel computations possible. The Finite Volume Method (FVM) used in this work is briefly described below. For more details on the numerical methods see Eriksson.[39]

The Kirchhoff-Helmholtz[40] method is used in the test cases to extend the prediction of the acoustic solution to the far-field, and the details related to this method are discussed in section 4.3. This is followed in section 4.4 by a description of the absorbing boundary conditions used in the computations using the linearized Euler equations. The finite volume method solver used for solving the flow equations is first presented in the following sections.

### 4.1.1 Finite Volume Method

The linearized Euler equations can be written on a compact conservative form as

$$\frac{\partial Q'}{\partial t} + \frac{\partial F_j}{\partial x_j} = 0 \tag{4.1}$$

where

$$Q' = \begin{pmatrix} \rho' \\ (\rho u_i)' \\ (\rho e_0)' \end{pmatrix} \qquad F_j = \begin{pmatrix} (\rho u_j)' \\ \widetilde{u}_j(\rho u_i)' + \widetilde{u}_i(\rho u_j)' - \rho'\widetilde{u}_i\widetilde{u}_j + p'\delta_{ij} \\ \widetilde{h}_0(\rho u_j)' + \widetilde{u}_j(\rho h_0)' - \rho'\widetilde{h}_0\widetilde{u}_j \end{pmatrix} \tag{4.2}$$

The Finite Volume Method used is based on a discretization of the equations on a structured, non-orthogonal curve-linear multi-block mesh. This is done by integrating 4.1 over a control volume $\Omega$

$$\int_\Omega \frac{\partial Q'}{\partial t}\mathrm{dV} + \int_\Omega \frac{\partial F_j}{\partial x_j}\mathrm{dV} = 0 \tag{4.3}$$

Introducing a volume average $\mathbf{Q}'$ of $Q'$ over $\Omega$ and using Gauss theorem on the second term we can write

$$V\frac{\partial \mathbf{Q}'}{\partial t} + \int_{\partial\Omega} F_j \cdot \mathrm{dS_j} = 0 \tag{4.4}$$

where $dS_j = n_j dS$ is a surface normal element on $\partial\Omega$. In words equation 4.4 says that the rate of change of the volume average of the state vector $Q'$ is equal to the integral of the flux through the boundary of volume $\Omega$. If $\Omega$ is the volume defining a cell in a computational mesh the flux term can be rewritten as the sum of the fluxes through the cell faces of control volume $\Omega$

$$\int_{\partial\Omega} F_j \cdot \mathrm{dS_j} = \sum_{all\,faces} \int_{face} F_j \cdot \mathrm{dS_j} \tag{4.5}$$

Assuming that $F_j$ is constant over each face, equation 4.5 can be written as

$$\int_{\partial\Omega} F_j \cdot \mathrm{dS_j} = \sum_{all\,faces} F_j^{face} \cdot S_j^{face} \tag{4.6}$$

where $S_j^{face}$ is the surface normal vector times the surface area of the face. The governing equations discretized on a structured mesh can now be written as

$$V\frac{\partial \mathbf{Q}'}{\partial t} + \sum_{all\,faces} F_j^{face} \cdot S_j^{face} = 0 \tag{4.7}$$

Solving equation 4.7 is done by estimating the values of $F_j$ on the faces and then use a time marching technique to advance the solution in time. The procedure is then repeated using the new solution from the last time step.

### 4.1.2 Convective Fluxes and Artificial Dissipation

The convective fluxes are computed using an approach based on a transformation of the solution on the cell face into characteristic variables, see Appendix 7.4. The reason for this is to be able to add a small amount of artificial numerical dissipation through an upwinding of the convective scheme. The methodology is as follows.

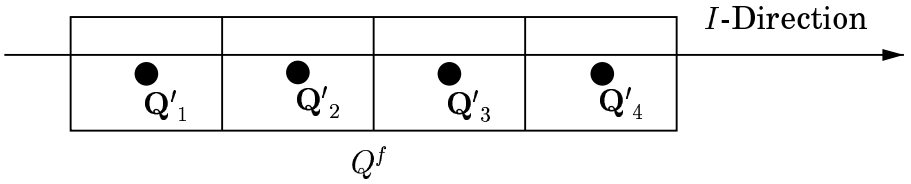


Figure 4.1: Estimation of face value $Q^f$ is based on cell averages $\mathbf{Q}'_1$ to $\mathbf{Q}'_4$.

The solution vector $Q^f$ is computed on the face in a right-hand side upwinded version and a left-hand side upwinded version. The upwinding is based on adding a dissipative term to the system of equations. This term is multiplied by a small number $\epsilon$ to add a small amount of dissipation, see Appendix 7.2. This is illustrated here using a four-point stencil

$$\begin{aligned} Q_L^f &= b_1\mathbf{Q}'_1 + b_2\mathbf{Q}'_2 + b_3\mathbf{Q}'_3 + b_4\mathbf{Q}'_4 \\ Q_R^f &= b_4\mathbf{Q}'_1 + b_3\mathbf{Q}'_2 + b_2\mathbf{Q}'_3 + b_1\mathbf{Q}'_4 \end{aligned} \tag{4.8}$$

where $Q_L^f$ is the left-hand side upwinded and $Q_R^f$ is the right-hand side upwinded estimates on the face and the upwinded coefficients $b_i$ are given by

$$
\begin{aligned}
\mathrm{b}_1 &= a_1 \pm \epsilon\ d_1 \\
\mathrm{b}_2 &= a_2 \pm \epsilon\ d_2 \\
\mathrm{b}_3 &= a_3 \pm \epsilon\ d_3 \\
\mathrm{b}_4 &= a_4 \pm \epsilon\ d_4 \\
\mathrm{b}_5 &= a_5 \pm \epsilon\ d_5 \\
\mathrm{b}_6 &= a_6 \pm \epsilon\ d_6
\end{aligned}
\tag{4.9}
$$

The coefficients $a_i$ are the coefficients of the symmetric convective scheme and $d_i$ are chosen to approximate an odd order derivative which is scaled with the small parameter $\epsilon$, see Appendix 7.2.

The left and right-hand side upwinded solution vectors $Q_f^L$ and $Q_f^R$ are transformed in the $I$-direction into vectors for the characteristic variables, $W_L^{(n)}$ and $W_R^{(n)}$ representing one-dimensional waves through the cell face, see Appendix 7.4. Using the reference solution in the linearized Euler equations an average of the two neighboring cells is computed as

$$Q_a = 0.5(\overline{\mathbf{Q}}_2 + \overline{\mathbf{Q}}_3) \tag{4.10}$$

which is used to compute the eigenvalue $\lambda^{(n)}$ associated to each characteristic variable, see Appendix 7.4. In three dimensions there are five characteristic variables corresponding to one entropy, two vorticity and two acoustic waves with the eigenvalue associated to each characteristic variable representing the velocity of that wave.

The solution is transformed back from characteristic variables to physical variables using information about the eigenvalues. If the eigenvalue $\lambda^{(n)}$ associated to the characteristic variable $W^{(n)}$ is positive, the left-hand side upwinded version is used in the transformation back to physical variables and if the eigenvalue $\lambda^{(n)}$ is negative, the right-hand side upwinded version is used. This corresponds to an upwinding of each characteristic variable depending on the direction in which the wave is traveling through the face. Finally the flux through the face, equation 4.7, is computed using the solution estimated on the face.

The numerical scheme used in the present work is the six-cell finite volume version of the fourth-order Dispersion Relation Preserving (DRP) scheme proposed by Tam,[41] and a sixth-order derivative of the solution vector is used in the upwinding of the numerical scheme. The coefficients of the numerical scheme are given in Appendix 7.5 and the resulting dispersion relation and dissipation relation are shown in Appendix 7.2.

### 4.1.3 Time Marching

When the spatial fluxes are computed as in the section above, equation 4.7 can be written on the form

$$\frac{\partial \mathbf{Q}'}{\partial t} = \mathcal{F} \tag{4.11}$$

where $\mathcal{F}$ is the sum of the spatial fluxes per unit volume. The time integration is performed using a four-stage 4:th order low storage Runge-Kutta time marching technique

$$\begin{aligned}
\mathbf{Q}'_{*} &= \mathbf{Q}'_{m} + \frac{1}{4}\Delta t \mathcal{F}(\mathbf{Q}'_{m}) \\
\mathbf{Q}'_{**} &= \mathbf{Q}'_{m} + \frac{1}{3}\Delta t \mathcal{F}(\mathbf{Q}'_{*}) \\
\mathbf{Q}'_{***} &= \mathbf{Q}'_{m} + \frac{1}{2}\Delta t \mathcal{F}(\mathbf{Q}'_{**}) \\
\mathbf{Q}'_{m+1} &= \mathbf{Q}'_{m} + \Delta t \mathcal{F}(\mathbf{Q}'_{***})
\end{aligned} \tag{4.12}$$

where $\mathbf{Q}'_{m}$ is the solution at time step $m$ and $\mathbf{Q}'_{m+1}$ is the computed solution at time step $m+1$.

The time step $\Delta t$ is chosen such that the highest $\mathrm{CFL}$-number in the computational domain is below a specified value. The time step is given by $\Delta t = \mathrm{CFL}/\mathrm{SR}$ where $\mathrm{SR}$ is the convective spectral radius.[42] The numerical scheme is stable up to $\mathrm{CFL}$ about unity. The maximum $\mathrm{CFL}$-number is however chosen to $0.5$ in most computations. Above this $\mathrm{CFL}$-number the amplitude error caused by the artificial numerical dissipation starts to become important for low wave numbers. See Appendix 7.2 for a stability analysis of the fully discretized equations using the above specified scheme.

## 4.2 Solver for the Convective Operator

The numerical methods for solving the convective operator (equation 3.15) in the proposed SNGR method are the same as for the linearized Euler equations except for the order of accuracy. An upwinded third order numerical scheme is used for the convective fluxes and a second-order three stage Runge-Kutta method is used for time stepping. The numerical coefficients for the convective scheme are given in Appendix 7.5. The boundary conditions for the convective operator are based on characteristical variables and are presented in section 4.4.

An important detail in the proposed SNGR method is that all scales which are synthesized must be resolved by the numerical schemes in all steps of the computations. The synthesized velocity field must be resolved on the mesh so that the convective operator (equation 3.15) can propagate it without too much dispersion of amplitude errors (see Appendix 7.2). Through the evaluation of the source terms in equation 3.22 there is a doubling of the wave numbers and frequencies so that the requirements on the solution of the ILEE is even higher than that of the convective operator. This doubling comes from the non-linearity of the source terms, see equation 3.22. The resolutions for the highest modes in the near-field of the jet simulations are $7$ and $3.5$ cells per wavelength respectively for the numerical schemes for the convective operator and the solver for the ILEE.

## 4.3 Kirchhoff-Helmholtz Method

Kirchhoff-Helmholtz integration[40] is a method to predict a state variable governed by the linear homogeneous wave equation at a point, based on information of the same state variable from a closed surface enclosing all non-linear sound generating structures. In aeroacoustics, this is used to predict the pressure disturbances outside of the computational domain for the flow field. Given here is a short presentation of the Kirchhoff-Helmholtz method. For a more detailed analysis, see.[40,43,44]

The Kirchhoff-Helmholtz surface is assumed to enclose all non-linear effects and sound sources. Outside this surface the field is linear and is governed by the wave equation. The Kirchhoff formulation for a quantity $\Phi$ satisfying the wave equation outside a stationary control surface, can be written as (Pierce[44])

$$\Phi(\mathbf{x},t) = \frac{1}{4\pi}\int_S \left[\frac{\Phi}{r^2}\frac{\partial r}{\partial n} - \frac{1}{r}\frac{\partial \Phi}{\partial n} + \frac{1}{c_0 r}\frac{\partial r}{\partial n}\frac{\partial \Phi}{\partial t}\right]_{\tau'} \mathrm{d}S \tag{4.13}$$

In the above equation $[]_{\tau'}$ stands for evaluation at the emission time. The normal derivative of the distance between the surface and the observer, $\partial r/\partial n$, is actually $\cos(\theta)$, where $\theta$ is the angle between the vector $\mathbf{r} = \mathbf{x} - \mathbf{y}$ and the outward pointing normal vector $\mathbf{n}$. Equation 4.13 gives $\Phi$ at an arbitrary point $\mathbf{x}$ at time $t$ outside of the control surface $S$ as a function of the information given at $\mathbf{y}$ on the surface $S$ at time $\tau'$.

The Kirchhoff-Helmholtz integration method relies formally on the use of a closed integration surface enclosing all sound sources. In a real

jet case however, it is not feasible to extend the computational domain in the axial direction to ensure that all sound generating structures are inside a closed surface, see figure 4.2. There is always a portion of the downstream boundary through which a considerable amount of vorticity is convected. To minimize the error in the Kirchhoff-Helmholtz integration, the integration surface is left open on this boundary. This is a violation of the conditions under which the theory holds. However, Freund *et al.*[43] have shown that the major contribution to the solution at an observation point comes from a point on the surface that intersects a line between the observer and the source point, see figure 4.2. The errors involved using the open surface are smaller than what would have been the case if the surface would have crossed the outflow region.

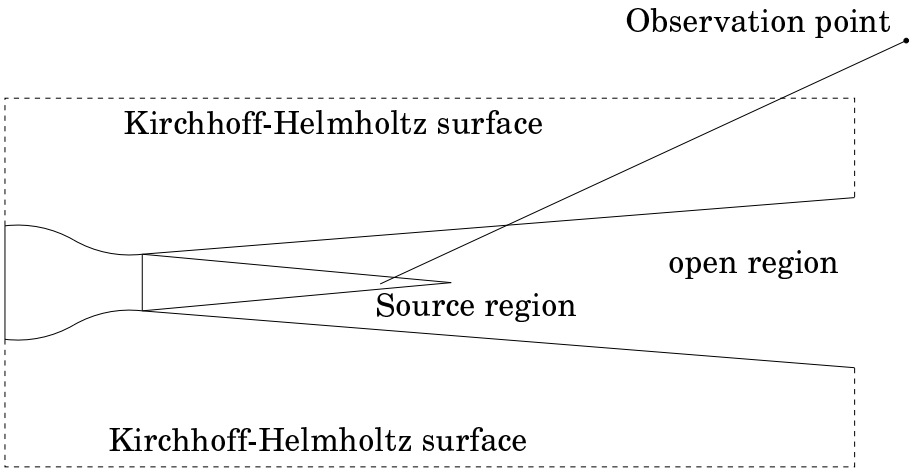


Figure 4.2: Kirchhoff-Helmholtz surface for jet case. - - - : Kirchhoff-Helmholtz surface.

The implementation of the Kirchhoff method used in this work is based on a forward time formulation which enables direct integration of equation 4.13 during the simulation of the linearized Euler equations without having to save the surface pressure for post-processing. The Kirchhoff-Helmholtz integral method implementation used in this work has been validated using a test case consisting of a monopole in a box, see Billson.[45] The results were in excellent agreement with the analytical solution.

## 4.4 Boundary Conditions

### 4.4.1 Characteristic Variable Based Absorbing Boundary Conditions (Cvba)

The boundary conditions presented here are similar to the ones presented by Thompson[46,47] but the details are not the same. The formulation of the boundary conditions presented here is derived by Eriksson.[39] The boundary conditions are based on a characteristic variable based representation of the governing equations in the direction of the outward facing normal vector $\mathbf{n}$. This transformation is presented in Appendix 7.4 and only the outline is given here.

The governing equations can be transformed into a set of decoupled equations in one direction. The transformed equations govern propagation of planar waves in the direction of the analysis. The degrees of freedom are the five characteristic variables, $W^{(i)}$, each governed by the equation

$$\frac{\partial W^{(i)}}{\partial t} + \lambda^{(i)} \frac{\partial W^{(i)}}{\partial \xi} = 0 \tag{4.14}$$

where $\lambda^{(i)}$ is the characteristic speed associated with the characteristic variable and $\xi$ is the spatial variable in the $\mathbf{n}$-direction.

The sign of the characteristic speeds $\lambda^i$ at the boundary gives information about the direction in which the characteristic variable $W^{(i)}$ is traveling. This information is used to set up the boundary conditions. The boundary condition is set up as

$$\begin{array}{lll} \text{Specify } W^{(i)} \text{ at boundary} & \text{if} & \lambda^{(i)} \leq 0 \\ \text{Extrapolate } W^{(i)} \text{ from interior domain} & \text{if} & \lambda^{(i)} \geq 0 \end{array} \tag{4.15}$$

The expressions above state that if information of $W^{(i)}$ is transported into the domain, the value of $W^{(i)}$ has to be given as a boundary condition. If the information of $W^{(i)}$ is transported from the inside of the domain, toward the boundary, the value of $W^{(i)}$ does not need to be specified and $W^{(i)}$ is extrapolated from the solution. When the appropriate action has been made on each characteristic variable, the solution is transformed back into the state variables again. This boundary condition gives complete absorption of planar waves propagating normally toward the boundary. For waves with oblique incidence to the boundary there will only be a partial absorption, see figure 4.3.

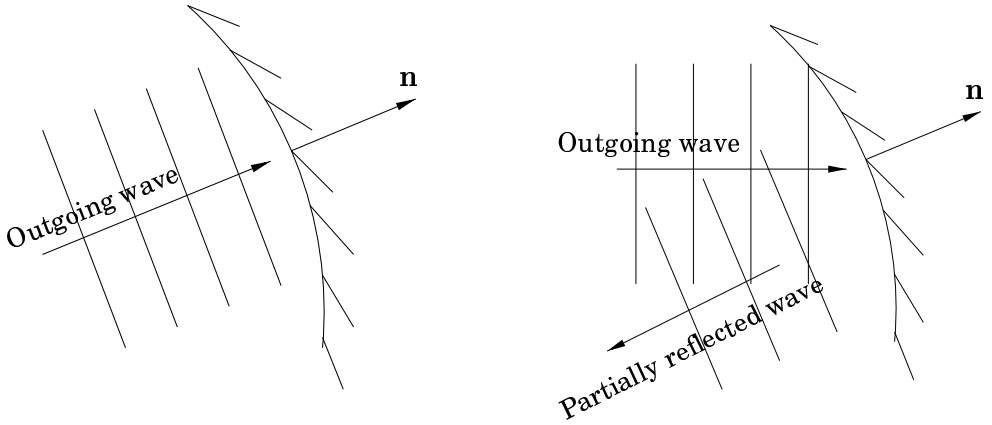


Figure 4.3: Absorbed wave v.s. partially reflected wave.

### 4.4.2 Modified Characteristic Variable Based Absorbing Boundary Conditions (Cvba)

The modified boundary conditions based on characteristic variables are equal to the original boundary conditions based on characteristic variables except for one detail. The original boundary conditions are completely absorbing for waves traveling with normal incidence to the boundary. This is a result of choosing the boundary normal vector $\mathbf{n}$ as direction for the local analysis describes above. The idea with the modified version of the original boundary conditions is that if the direction of the waves propagating toward the boundary is known, the local analysis of the governing equations is made in that direction. This leads to complete absorption in this direction, see figure 4.4.2. The problem is then to choose the direction in which performing the analysis. In many problems the direction to the main source region is approximately known and the direction of the analysis of the boundary conditions can be chosen accordingly. Tests of these modified boundary conditions are presented in section 5.1.

### 4.4.3 Buffer Layer

At the far-field and inflow boundary the only disturbances reaching the boundary are acoustic waves. The energy content in sound waves is usually very small and even if there is a small fraction of the disturbance which is reflected back into the computational domain the energy of the reflected wave will be very small.

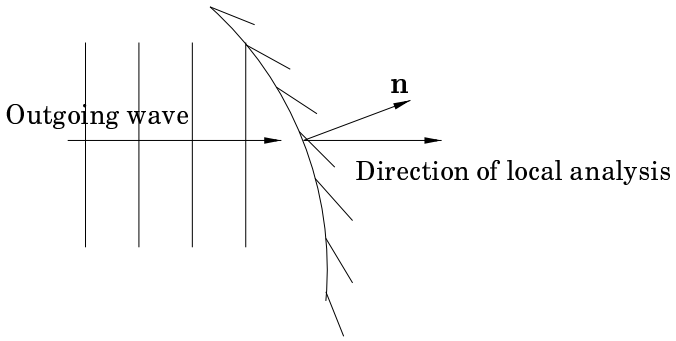


At the outflow however there are vorticity and entropy disturbances convected with the flow reaching the boundary as well as acoustic disturbances. The energy content in vorticity and entropy waves is very large at the outflow compared to acoustic waves. So if the boundary condition at the outflow does not completely absorb all energy from the vorticity and entropy disturbances very large acoustic disturbances will reflect back into the computational domain. These waves will be an artifact of poor boundary conditions and not part of the correct solution. This contamination of the solution must be avoided. To ensure that there are no reflections from the outflow region a buffer layer is often applied. The buffer layer is an extension of the computational domain in the downstream direction in which extra terms are added to the equations. The way this is done was first proposed by Colonius *et al.*[48] Assuming that the buffer layer is added in the computational domain in the $x$-direction, the terms added to the governing equations are

$$\frac{\partial Q'}{\partial t} = \cdots - \frac{c_0 \sigma(x)}{(x_{max} - x_0)} (Q') \tag{4.16}$$

where

$$\sigma(x) = \sigma_{max} \left( \frac{x - x_0}{x_{max} - x_0} \right)^2 \tag{4.17}$$

where $c_0$ is the local reference speed of sound. The strength of the buffer layer, $\sigma_{max}$, is chosen to achieve a certain amount of damping and $x_0$ and $x_{max}$ define the beginning and end of the buffer layer (assuming that the flow is mainly in the $x$-direction). The parabolic shape of $\sigma(x)$ reduces the risk that the damping term will cause reflections into the computational domain.

# Chapter 5

# Test Cases

This chapter is a summary of the most important numerical tests which have been performed in the project. Some of the cases have been published in one of the Papers I-IV[24–26,32] or are documented in an internal report, Paper V.[49] These documents are found in the back of this thesis and only a short presentation of the results is given here. Other tests have not been published elsewhere and are fully described here.

## 5.1 Absorbing Boundary Conditions

Bogey and Bailly[50] have proposed two boundary condition test cases for boundary conditions formulated in three dimensions. The first case consists of a Gaussian acoustic pulse in a uniform mean flow and the second is an axisymmetric vortex in a uniform mean flow. The boundary conditions tested in [50] were reformulated versions in spherical coordinates of the boundary conditions proposed by Tam and Dong.[51] The test showed that the boundary conditions performed well as non-reflective boundary conditions for an acoustic pulse. In the vortex test case there was some reflection into the computational domain. The two test cases suggested in [50] are in the present work performed using the boundary conditions based on characteristic variables (Cvba) as well as a set of modified boundary conditions based on characteristic variables (MCvba), see section 4.4. The computational setup and the results are presented and discussed below.

The computational mesh consists of a $N^3$ mesh with $N = 100$ cells. The spatial extent of the mesh is $-50 \leq x, y, z \leq 50$ with a constant cell size $\Delta = 1$. The test case has been normalized by the variables in table 5.1. In the test cases below the $L_2$-norm of the pressure distur-

bance is computed for each time step. This is used as a measure of the performance of the boundary conditions. The norm is defined by

$$L_2(t) = \left[ \frac{1}{N^3} \sum_{i,j,k}^{N^3} p'^2_{i,j,k}(t) \right]^{1/2} \tag{5.1}$$

| | | | |
|---|---|---|---|
| length scale | : | $\Delta$ | cell size |
| velocity scale | : | $c_0$ | ambient speed of sound |
| time scale | : | $\Delta/c_0$ | |
| density scale | : | $\rho_0$ | ambient density |
| pressure scale | : | $\rho_0 c_0^2$ | |

Table 5.1: Normalization variables

### 5.1.1 Gaussian Acoustic Pulse

The first test case consists of an initial Gaussian acoustic pulse in a mean flow in the $x$-direction with Mach number $M = 0.5$, mean density $\overline{\rho} = 1$ and mean pressure $\overline{p} = 1/\gamma$. The initial condition is

$$\begin{aligned} \rho' &= \epsilon \exp[-\alpha r^2] \\ u'_1 &= 0 \\ u'_2 &= 0 \\ u'_3 &= 0 \\ p' &= \epsilon \exp[-\alpha r^2] \end{aligned} \tag{5.2}$$

where $\alpha = (\ln 2)/b^2$, $b = 3$, $\epsilon = 10^{-3}$ and $r$ is the radius from the center of the pulse located in origo. More details on the test case can be found in [50].

The pressure disturbances $|p'|/\epsilon$ in the $xy$ plane are shown in figure 5.1. The left column represents the Cvba boundary conditions at times $t = 40$, $80$ and $120$. The center column represents the MCvba boundary conditions at the same times. In the test by Bogey and Bailly there were no visible reflections back into the computational domain using the same scale for the iso-contours as in figure 5.1, whereas the results using the Cvba and MCvba show reflections. The outgoing wave reaches the boundary with a level of $|p'|/\epsilon \approx 0.02$. The reflected waves from the boundaries have an amplitude of $|p'|/\epsilon \approx 0.001$ or about $5\%$ of the original wave amplitude. In the test by Bogey and Bailly the reflection was below $2\%$ and below the scale of the iso-contours.

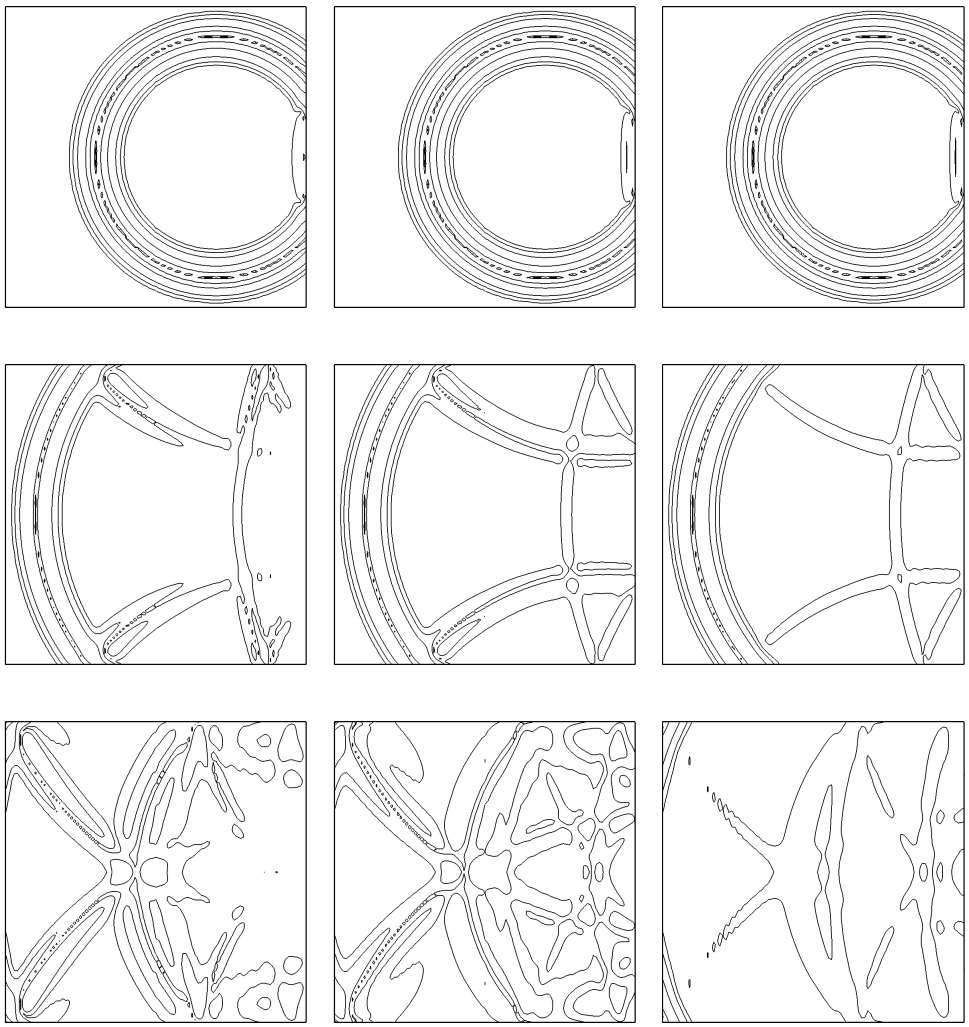

Figure 5.1: Scaled pressure disturbance $|p|/\varepsilon$. **Left column**: Characteristic variable based boundary conditions, Cvba. **Center column**: Modified Cvba. **Right column**: Modified Cvba with moving source correction. At times $t = 40$ (top), $80$ (middle) and $120$ (bottom). Isocontours from $2.5 \times 10^{-4}$ to $1.6 \times 10^{-2}$ using $4$ levels with a geometrical ratio of $4$.

The time history of the $L_2$ norm for the acoustic pulse is shown in figure 5.2(a). The norm is normalized by the initial value of the norm at time $t = 0$. The norm decreases in steps as the pulse reaches the outflow, side and inflow boundaries. The non-zero value of $L_2 \approx 3 \times 10^{-2}$ at times $t > 150$ represents the amount of reflected waves. This correspond to about one order of magnitude lower compared to the initial value. The corresponding result of Bogey and Bailly is about two order of magnitude decrease of the $L_2$ norm at time $t = 150$.

The results from the modified and the original Cvba boundary conditions are similar with just slightly less reflection from the modified boundary conditions. One would expect the modified boundary conditions to perform better than the original boundary conditions. But it should be noted that the direction of the one-dimensional analysis was specified as if the source was located in the center of the computational domain, $(x_0, y_0, z_0) = (0, 0, 0)$. The center of the source is however moving with the local convection speed so the estimate is actually not such a good approximation by the time the acoustic pulse reaches the boundary.

To illustrate the point the same computation was performed using the modified Cvba in which the origin of the moving source was specified as $(x_0, y_0, z_0) = (\overline{u}t, 0, 0)$. The resulting pressure iso-contours are shown in the right column of figure 5.1 and the $L_2$ norm is the dash-dotted line in figure 5.2(a). The result is much improved up to $t = 140$. The increase in the norm after $t = 140$ is related to that the source by then is outside the computational domain and thus inverting the direction of the one-dimensional analysis for the outflow boundary. The result is encouraging since the source location is often approximately known and the modified boundary conditions would in that case be efficient as absorbing boundary conditions for acoustic disturbances.

### 5.1.2 Convected Axisymmetric Vortex

The second test case proposed in [50] is that of a convected axisymmetric vortex. The mean flow is defined by $\overline{\rho} = 1$, $\overline{\mathbf{u}} = (M, 0, 0)$, $M = 0.5$, $\overline{p} = 1/\gamma$. The initial velocity disturbance is defined by

$$\begin{aligned} u_x &= \epsilon \frac{r_0}{r}(r - r_0)\exp\left[-\alpha\left(x^2 + (r - r_0)^2\right)\right] \\ u_r &= -\epsilon \frac{r_0}{r} x \exp\left[-\alpha\left(x^2 + (r - r_0)^2\right)\right] \end{aligned} \tag{5.3}$$

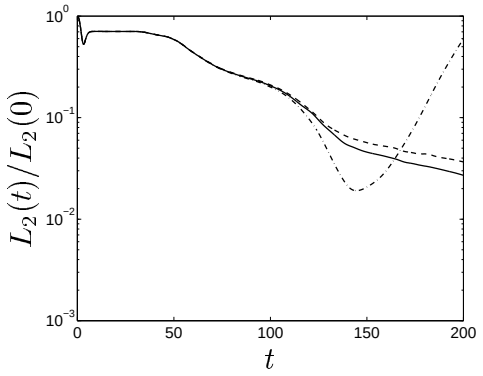


(a) Gaussian acoustic pulse in uniform mean flow. $L_2/L_2(0)$ as a function of time.

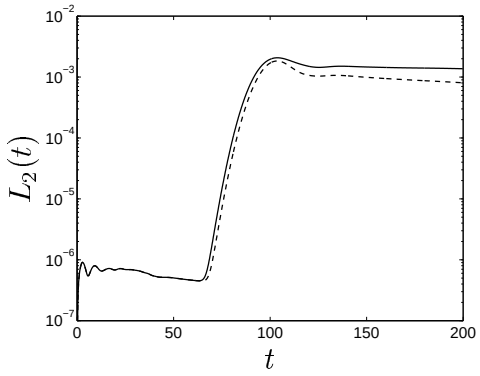


(b) Axisymmetric vortex in uniform mean flow. $L_2$ as a function of time.

Figure 5.2: Evaluation of boundary conditions. (a) Gaussian acoustic pulse in uniform mean flow, (b) axisymmetric vortex in uniform mean flow. Solid lines: modified Cvba boundary conditions; dashed lines: Cvba boundary conditions.; dash-dotted line in (a): modified Cvba boundary conditions with moving source specified

where

$$r = (y^2 + z^2)^{1/2}, \quad \theta = \arctan(z/y) \tag{5.4}$$

The vortex radius is $r_0 = 20$, $\alpha = (\ln 2)/b^2$, $b = 5$ and $\epsilon = 0.03$. The initial density and pressure disturbances are set to zero.

The vorticity magnitude $|\omega_3| = |\partial u_2'/\partial x - \partial u_1'/\partial y|$ in the $xy$ plane is shown in the left column of figure 5.3 and the pressure disturbance in the right column. The times are $t = 50$, $100$ and $150$. The figures show the vortex as it is convected out of the computational domain. The pressure iso-contours are chosen so that the initial pressure disturbance in the vortex is smaller than the lowest iso-contour. When the vortex is convected through the boundary, it generates acoustic waves which propagate into the domain and contaminate the computational domain.

The time history of the $L_2$ norm of the pressure disturbance is shown in figure 5.2(b). An initial disturbance is generated from the sudden start of the vortex. The hydrodynamic pressure disturbance associated with the vortex is settled after $t \approx 20$ with a norm $L_2 = 6 \times 10^{-7}$. When the vortex reaches the boundary at about $t = 70$, reflection of acoustic waves cause a drastic increase in the $L_2$ norm with a peak of

$L_2 = 2 \times 10^{-3}$ when the vortex center reaches the boundary at $t = 103$. This represents an increase in the $L_2$ norm of about $3.5$ orders of magnitude. The corresponding result from the test by Bogey and Bailly[50] is an increase in the $L_2$ norm of about $2$ orders of magnitude. Clearly the boundary conditions based on asymptotic analysis of the Euler equations (Ref. [50]) are more efficient as absorbing boundary conditions for vorticity than the characteristical variable based boundary conditions.

From the two tests above it can be concluded that the Mcvba is a good alternative for radiation boundary conditions where only acoustic waves reach the boundary. In the outflow region where vorticity and entropy waves reach the boundary both the boundary conditions presented in [50] and the present boundary conditions are insufficient and a buffer layer boundary condition is required. In combination with a buffer layer the Mcvba and the Cvba are used in the simulations in the present work.

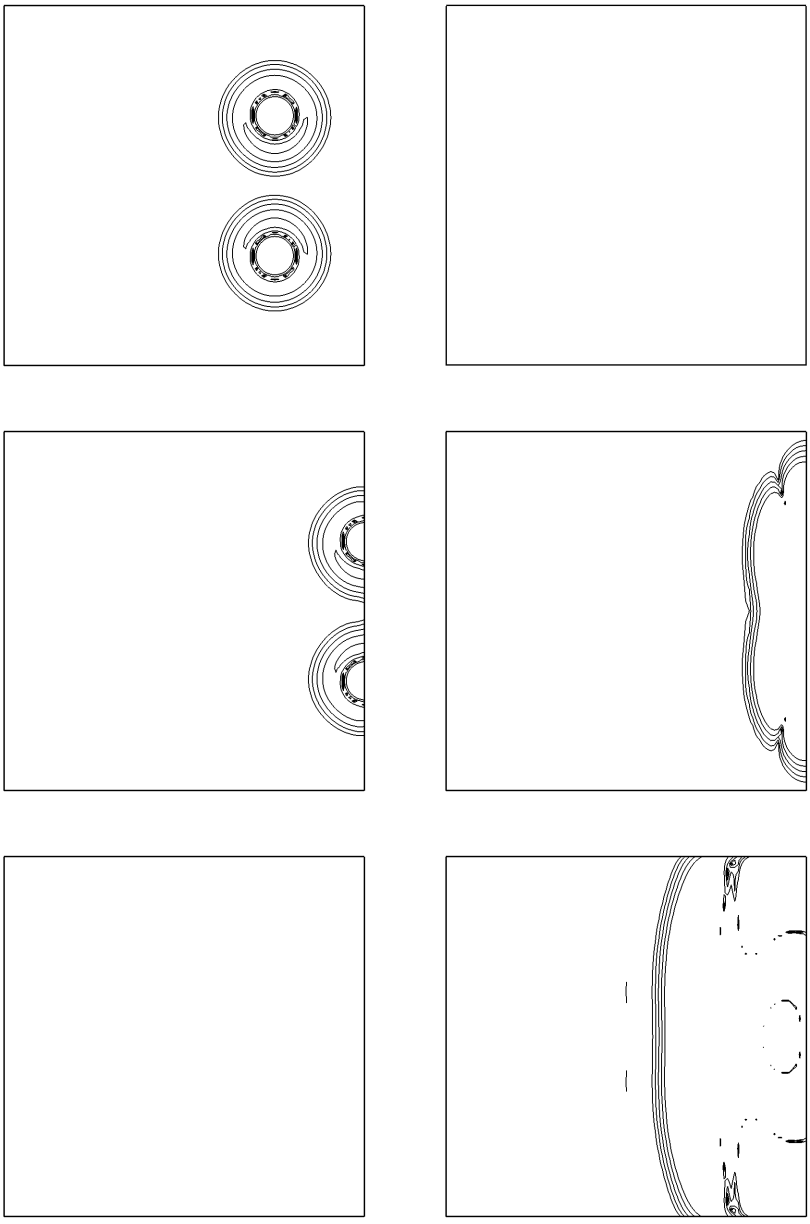

Figure 5.3: Mcvba results. Vorticity magnitude $|\omega_3| = |\partial u_2'/\partial x - \partial u_1'/\partial y|$ (left) and pressure amplitude $|p'|$ (right) for times $t = 50$ (top), $100$ (middle) and $150$ (bottom). Iso-contours: vorticity from $5 \times 10^{-4}$ to $80 \times 10^{-4}$ and pressure from $5 \times 10^{-6}$ to $80 \times 10^{-6}$ using $5$ levels with a geometrical ratio of $2$.

## 5.2 2D Mixing Layer

The forced 2D mixing layer test case was presented in Paper I.[32] The purpose of the test case was to validate that the derived ILEE in conservative form did give the acoustic solution associated with a specified source field. Simplified source terms with only fluctuating velocities to be used in the SNGR method were also evaluated.

The use of a forced 2D mixing layer as a test case for different acoustic analogies was first presented by Colonius *et al.*,[52] who performed a Direct Numerical Simulation (DNS) of a forced mixing layer and compared the results with Lilley's acoustic analogy.[17] Bogey *et al*[34,53] made a sound prediction with Large Eddy Simulation (LES) and Lighthill's analogy as well as LES and the linearized Euler equations (as derived in [22]) on a forced mixing layer. The results of the direct simulations and the analogies in [52] and [34, 53] were in good agreement.

In Paper I, a direct simulation of a forced 2D mixing layer was carried out. The direct simulation also provided the mean flow and source field for the inhomogeneous linearized Euler equations, equation 3.22. Simulations were performed using the full source terms in equation 3.22 as well as using simplified source terms suited for the SNGR method. See Paper I[32] for more details on the different source term formulations. The solutions to the inhomogeneous linearized Euler equations were compared to the solution of the direct simulation and showed a good agreement.

The mixing layer consists of an upper stream with a Mach number of $M_1 = 0.5$ and a lower stream with Mach number $M_2 = 0.25$. At the interface between the two streams a hyperbolic-tangent profile is used as inflow boundary profile. The mean inlet stream-wise profile is

$$\widetilde{u}_{in} = \frac{U_1 + U_2}{2} + \frac{U_1 - U_2}{2} \tanh\left(\frac{2y}{\delta_\omega(0)}\right) \tag{5.5}$$

where $U_1$ and $U_2$ are the upper and lower velocities respectively. The initial vorticity thickness $\delta_\omega(0) = 0.02$ [m] defines the thickness of the incoming velocity profile, see figure 5.4. The velocity at the inflection point is defined by $U_0 = (U_1 + U_2)/2$. The span-wise velocity $\widetilde{v}_{in}$ is set to zero at the inlet. The pressure and density are constant over the inlet and are set to normal atmospheric conditions. The Reynolds number for this flow based on the initial vorticity thickness $\delta_\omega(0)$ is $Re_\omega = \delta_\omega(0)U_0/\nu = 1.58 \times 10^5$.

A two-dimensional laminar shear layer is unstable by nature and will start to break up if the computational domain is long enough. This

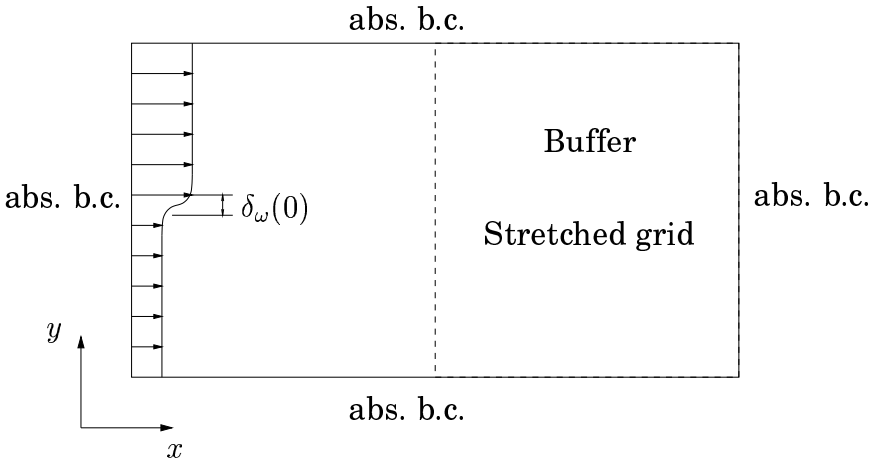


Figure 5.4: Computational domain. Absorbing boundary conditions (abs. b.c.) are used at all boundaries

process might take some time though and the laminar part of the shear layer can be quite long in the stream-wise direction. The acoustic field produced in this process will also be more or less stochastic with peaks in the spectra for the frequencies corresponding to the natural instability frequencies of the shear layer. To get better control of the shear layer and to make it break up faster, forcing is applied at the inflow boundary. This forcing is done using the inflow absorbing boundary conditions. The incoming vorticity characteristic variable is modulated at the fundamental frequency of the incoming profile. The resulting forcing enters the span-wise inflow velocity component as

$$v_{in} = \widetilde{v}_{in} + A\sin(\omega_0 t) \tag{5.6}$$

where $A$ is the amplitude of the forcing. The forcing is only applied in the region of the hyperbolic-tangent profile. Since the forcing is included as a part of the absorbing boundary conditions, the forcing does not interfere with the absorbing property of the boundary condition and the amount of spurious waves created by the forcing is kept to a minimum. An important detail is that the forcing added in the direct simulation is also added in the linearized Euler simulation. The reasoning behind this is that unless this is done, the boundary condition for the linearized Euler simulation is not consistent with the sources evaluated from the direct simulation and disturbances not present in the direct simulation appear in the solution to the linearized Euler equations.

Bogey *et al.*[53] computed the fundamental frequency based on the

instability theory of Michalke[54] as

$$f_0 = 0.132 \left[ \frac{U_0}{\delta_\omega(0)} \right] \tag{5.7}$$

The shear layer is forced at two frequencies. The fundamental frequency $f_0$ and half the fundamental frequency $f_0/2$. In this way the forcing at the fundamental frequency will induce the creation of vortices at a frequency of $f_0$ which are convected downstream by the convection velocity. The second forcing at half the fundamental frequency will in turn induce a process where two successive vortices start to roll up around each other. This pair of vortices will after a short period of time start to merge and form a larger vortex. The frequency of this pairing will be denoted $f_p = f_0/2$ and the pairing time $T_p = 2T_0$. In this work, $A = 0.2$ for the forcing at the fundamental frequency $f_0$ and $A = 0.1$ for $f_0/2$. A more detailed description of the test case is given in Paper I.[32]

Figure 5.5 shows a snapshot of the vorticity in the near-field and the dilatation in the far-field for the direct simulation and the linearized Euler simulation with full source terms (equation 3.22). The solutions are very similar and the phase and amplitude seem to agree well. Some wiggles that are visible in the direct simulation are absent in the linear solution. The reason for this is probably non-linearities in the direct simulation. The solutions from the linearized Euler simulations using the simplified source terms (see Paper I[32]) are not shown due to the fact that it is hard see any difference in the solutions compared to the full source term simulation.

Figure 5.6 shows the instant pressure fluctuation at a line at $x = 2.0\,[\mathrm{m}]$ and $0.5 \leq y \leq 3.0[\mathrm{m}]$ for the direct simulation and the different linearized Euler solutions. The average pressure has been corrected for the direct simulation to avoid a problem with a low frequency drift in the pressure. The phase and amplitude of the linearized Euler solutions are in good agreement with the direct simulation except very near the mixing layer. The deviation in this near-field region is a result of an error in the time-average of the pressure. The solutions for the different source terms are clearly very similar.

The main conclusions from the 2D mixing layer test case is that the inhomogeneous linearized Euler equations on conservative form accurately predict the sound field related to a specified hydrodynamic source, and that the simplifications of the source terms do not noticeably affect the results.

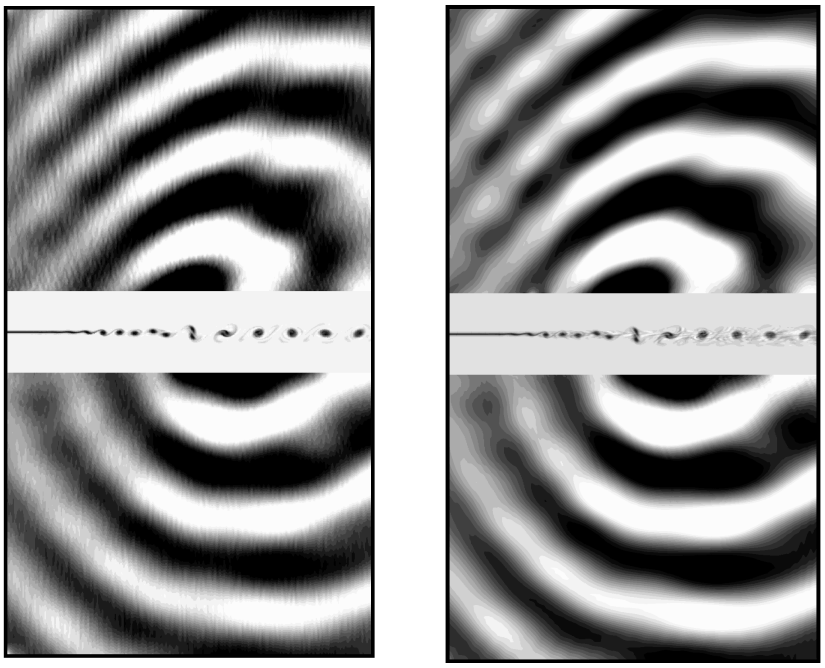

(a) Direct simulation

(b) Linearized Euler simulation

Figure 5.5: Vorticity and dilatation for direct simulation and linearized Euler equations using the full source terms, equation 3.22.

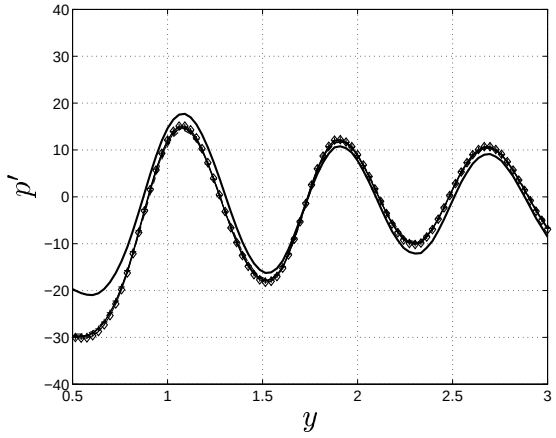


Figure 5.6: Pressure disturbance at $x = 2.0[\mathrm{m}]$, $0.5 \leq y \leq 3[\mathrm{m}]$. Solid line: direct simulation; others: different source terms

## 5.3 Modified Linearized Euler Equations

In an attempt to avoid the stability problems of the linearized Euler equations in shear flows (see section 3.4.2), the equations were modified using the same approach as Bogey *et al.*[34] The aim is to make the resulting equations stable in free shear flows. The method used here is simply to discard the spatial derivatives of the reference solution in the linearized Euler equations. The resulting equations in compact form are (see Appendix 7.1)

$$\frac{\partial Q'}{\partial t} + A_0 \frac{\partial Q'}{\partial x} + B_0 \frac{\partial Q'}{\partial y} + C_0 \frac{\partial Q'}{\partial z} = 0 \tag{5.8}$$

where the following terms have been neglected

$$\left[ \frac{\partial A_0}{\partial x} + \frac{\partial B_0}{\partial y} + \frac{\partial C_0}{\partial z} \right] Q' \tag{5.9}$$

The neglected terms in the modified equations contain the spatial derivatives of the reference solution. The resulting equations are equal to the full linearized Euler equations only for a homogeneous reference solution in which the derivatives of the reference solution are zero and the characteristic variables are analytically decoupled. The modified equations have a much weaker coupling between different characteristic variables and are therefore more stable in shear flows than the original equations.

This is shown in figure 5.7 where planar acoustic waves with Strouhal number $St = f\, D_j/U_j = 0.36$ are generated inside the nozzle of a Mach $0.90$ low Reynolds number jet.[55] The resulting sound field is represented by the axial acoustic intensity $p'u''$. The full linearized Euler equations (Eq. 3.22) are used for the result in figure 5.7(a) and the modified (Eq. 5.8) in figure 5.7(b). In both cases the sound waves exit the nozzle and are refracted out of the core region due to the mean flow. If there were no interactions between different types of characteristical variables, these would be the only disturbances in the solutions. In figure 5.7(a) however, the sound waves excite strong vorticity waves which are convected downstream. These are seen as the disturbances in the centerline region. The strong excitation of vorticity waves in figure 5.7(a) are not present in figure 5.7(b). There are some disturbances in the centerline region which are clearly not acoustical but the level is much lower than in figure 5.7(a).

The modified equations are clearly more stable than the full linearized Euler equations, as vorticity is not as strongly excited in the

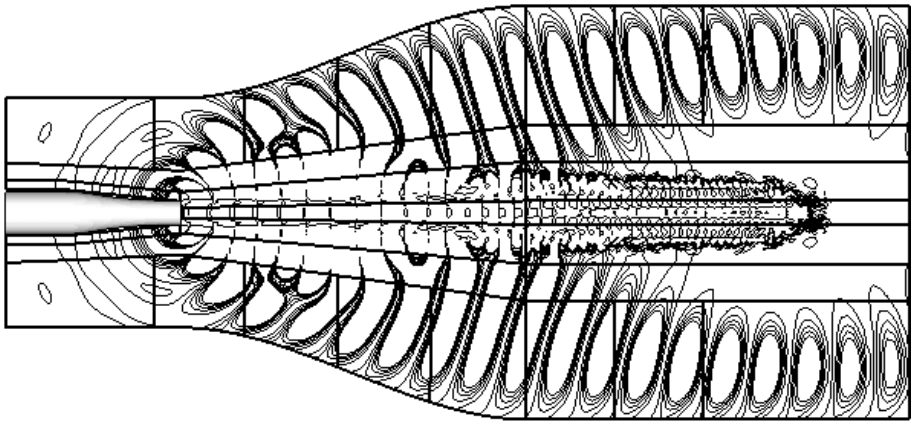

(a) Full linearized Euler equations

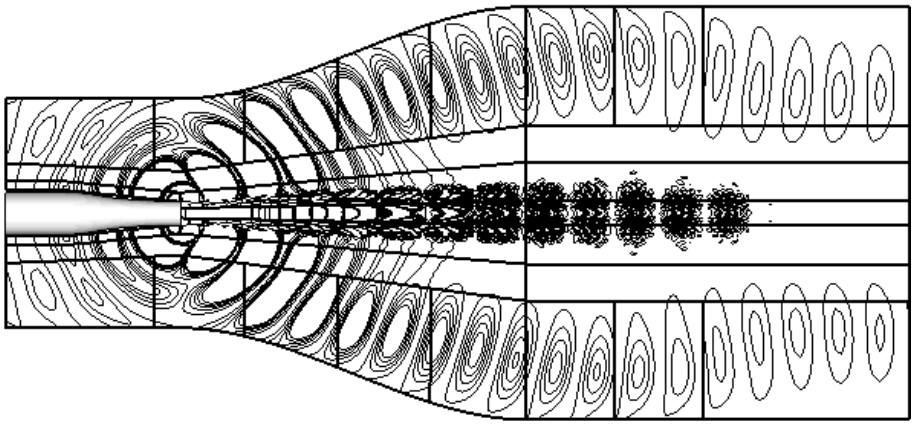

(b) Modified linearized Euler equations

Figure 5.7: Axial acoustic intensity $p'u''$ from plane acoustic waves generated in the nozzle.

presence of mean shear. There are however other differences in the solutions from the different sets of equations. The refraction of the acoustic waves is not the same in figures 5.7(b) and 5.7(a). There is a much larger intensity in the waves upstream of the nozzle using the modified equations than the full equations indicating that the modified equations do not give the correct refraction at the nozzle exit.

Figure 5.8 shows the pressure disturbances caused by a monopole located in the shear layer of the same Mach $0.90$ jet as before. The full linearized Euler equations are used for the result in figure 5.8(a) and

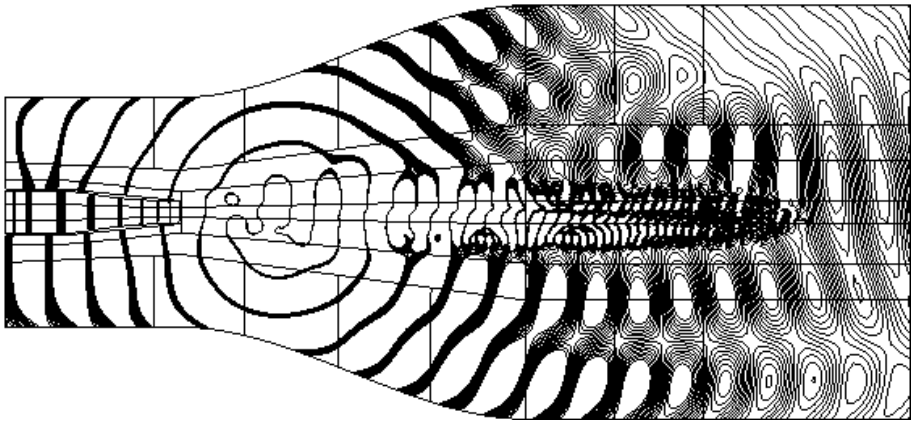

(a) Full linearized Euler equations

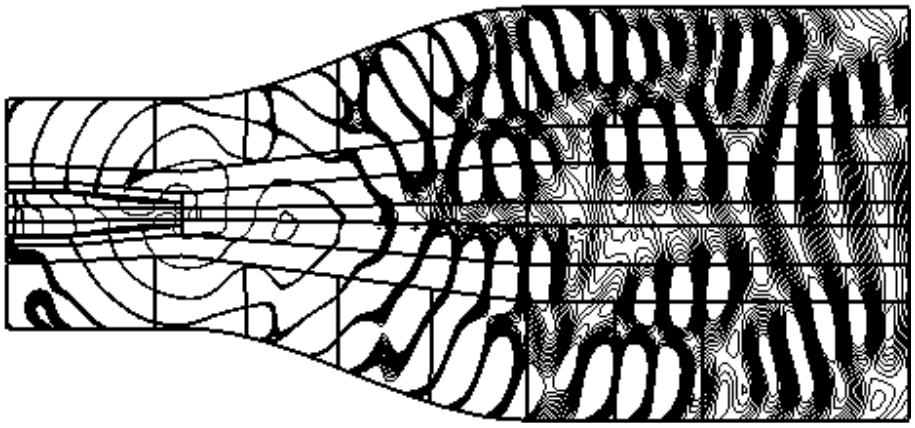

(b) Modified linearized Euler equations

Figure 5.8: Pressure disturbances in $xz$ plane from monopole located at $(x_0, y_0, z_0) = (4D_j, 0, 3/4D_j)$

the modified in figure 5.8(b). From the solutions in figures 5.8 there is a clear difference in the directivity of the sound field. This shows that the refraction of the sound generated from a monopole is not the same for the two sets of equations. The conclusion must be that the neglect of the mean shear terms as described above affect the sound propagation in a non-physical way. The modified equations are more stable which is positive but they lack some directional effects due to the absence of the terms in equation 5.9

The conclusions from the results are valid for the present formulation where $(\rho', (\rho u)', (\rho v)', (\rho w)', (\rho e_0)')$ are used as solution variables. In [34] for example where $(\rho', \overline{\rho}u', \overline{\rho}v', \overline{\rho}w', p')$ are used as solution variables (see section 3.4.2), the results of the same tests may be different since it is not exactly the same terms which are neglected when the modification is made to the equations.

## 5.4 Turbulence In a Box

The motivation for the box-turbulence test case which is presented in Paper III[25] was to have a simple generic test case in which turbulence could be generated and compared to theory. Homogeneous isotropic and anisotropic turbulence generated by the proposed SNGR method is presented and near-field and far-field statistics are compared to theory.

The test case consists of a box measuring $1 \times 1 \times 1$ [m] resolved by $128$ equally spaced cells in each direction. A source region is defined as the cube with $64$ cells in each direction in the center of the box. Turbulence is synthesized in the source region and the source terms to the ILEE are evaluated from this source field. Care is taken to avoid end-effects in the evaluation of the source terms by only evaluating the source terms in the interior of the source region. The ILEE are solved in the whole box and the acoustic solution is propagated out from the source region toward the boundaries. The modified boundary conditions based on characteristical variables (see section 4.4) are used as absorbing boundary conditions and the amount of reflections are minimal. The Kirchhoff method is used to extend the solution to the far-field in $108$ observer points placed on three circles, one in each coordinate plane (see figure 5.9). Each circle has a radius of $100$ box sizes.

The reference state in the box is a stagnant fluid with a density of $\overline{\rho} = 1.2$ kg/m$^3$ and pressure $\overline{p} = 100\,000$ Pa. The input turbulence kinetic energy and dissipation rate for the anisotropic synthesized turbulence are $\overline{k} = 763$ m$^2$/s$^2$ and $\varepsilon = 763 \times 10^3$ m$^2$/s$^3$ respectively. The length scale, time scale and amplitude factors are set to $f_L = 1$, $f_\tau = 3$ and $f_A = 1$. This gives a turbulence with time and length scales[24] of the synthesized turbulence equal to $(\tau_t, L_t) = (0.003, 0.028)$ [s, m]. For more details see Paper III.[25]

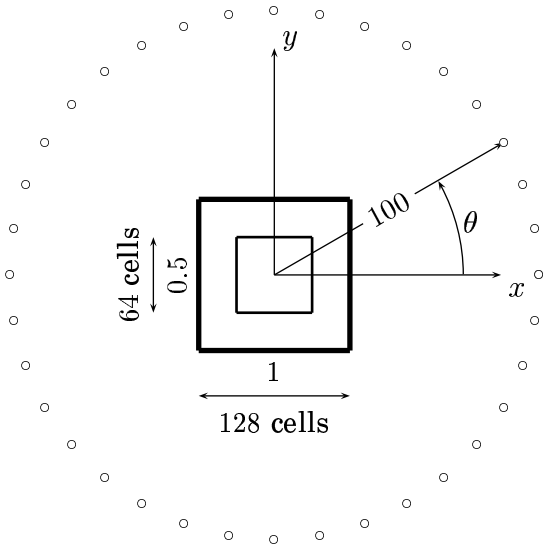


Figure 5.9: $xy$-plane through computational domain with 36 observer points. Small box: SNGR source region; Large box: LEE domain

### 5.4.1 Isotropic Turbulence

First some results will be presented from an isotropic case and the characteristics of the sound generated from the synthesized turbulence will be discussed. One can argue that both length and time scales of the turbulence must match a generated sound wave in order to get a strong noise generation. The turbulence spectral energy distribution in this isotropic case has a peak at wave number $k_p = 21$ corresponding to a length scale of $L_p = (2\pi)/k_p = 0.3\,[\mathrm{m}]$. Since the source terms in the inhomogeneous linearized Euler equations involve quadratic terms, $u_i'' u_j''$, the sound generating structure will be of length $L_s \approx L_p/2$. For a speed of sound of $342$ m/s this corresponds to a frequency of $f = 2280$ Hz for a sound wave which matches the length scale of the peak energy mode. This matches the region of peak energy of the far-field sound which can be seen in figure 5.10 showing the $1/3$ octave power spectral density of pressure at observer position $1$.

The noise generated by isotropic turbulence theoretically scales with frequency as $\omega^{-7/2}$ for high frequencies.[56] This scaling of the far-field noise is shown as the dashed line in Figure 5.10. The simulated and the theoretical data are in good agreement for high frequencies for up

to about $8000$ [Hz] with a drop-off for the simulated results above this frequency. This is directly related to the mesh resolution and the numerical scheme in the linearized Euler computation.

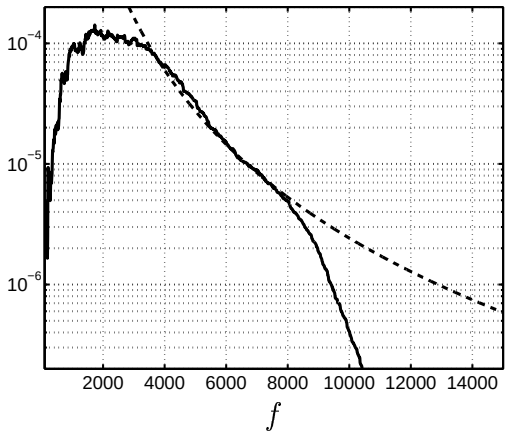


Figure 5.10: $1/3$ octave power spectral density of far-field pressure. Solid line: sampled data; dashed line: theory of isotropic turbulence

### 5.4.2 Anisotropic Turbulence

The test case for the anisotropic synthesized turbulence was conducted in the same way as for the isotropic case above. The only difference was that a specified anisotropic Reynolds stress tensor was prescribed in the generation of the synthesized turbulence. See section 3.3.3, or Paper III[25] for more details.

The near-field statistics of the synthesized turbulence was first investigated, including anisotropy of the turbulence in term of velocity and length scales. The normalized model stress tensor used in the first anisotropic case (case 1) is shown in table 5.2. The model stress tensor is diagonal and the anisotropy is evident from the differences in the diagonal components. The diagonal components of the normalized stress tensor determine the scaling of the individual velocity components in the generation of synthesized turbulence (equation 3.18). Also shown is the stress tensor computed from the statistics of the synthesized velocities.

Table 5.3 shows the normalized model and sampled stress tensors for a case (case 2) where the anisotropy is the same as in case 1. The only difference is that the model tensor has been rotated by $45$ degrees. The diagonal components are equal in this case and the anisotropy of the

| | | | | | |
|---|---|---|---|---|---|
| 1.5 | 0 | 0 | 1.499 | 0.002 | −0.003 |
| 0 | 0.5 | 0 | 0.002 | 0.495 | 0.002 |
| 0 | 0 | 1 | −0.003 | 0.002 | 1.005 |

Table 5.2: Normalized Reynolds stress tensor elements. case 1. Left: model tensor; Right: sampled from SNGR method.

| | | | | | |
|---|---|---|---|---|---|
| 1 | 0.5 | 0 | 0.998 | 0.494 | −0.005 |
| 0.5 | 1 | 0 | 0.494 | 0.996 | 0.003 |
| 0 | 0 | 1 | −0.005 | 0.003 | 1.006 |

Table 5.3: Normalized Reynolds stress tensor elements. case 2. Left: model tensor; Right: sampled from SNGR method.

tensor is only seen as a $\overline{u'v'}$ cross correlation. The results validate that a velocity field having an anisotropic stress tensor can be simulated using the proposed technique.

It is also shown in Paper III[25] that the length scales of the synthesized turbulence experience an effect of anisotropy. This is illustrated in figure 5.11(a) where the longitudinal and transversal two-point correlations in the direction of the largest normal stress component in the principal axes are plotted. Figure 5.11(b) shows the corresponding correlations in the direction of the smallest normal stress component. Shown are also the respective correlations for the isotropic case. Both the longitudinal and transversal correlations in figure 5.11(a) are increased by the anisotropy illustrating that the correlations increase in the direction of the largest stress component. The opposite effect with a reduction of the correlations in the direction of the smallest stress component is evident in figure 5.11(b).

The OASPL (Overall Sound Pressure Level) of the emitted sound from the anisotropic turbulence in case 1 and 2 are shown in figure 5.12. The directivity of the OASPL indicates that the direction of maximum sound emission can be deduced from the Reynolds stress tensor when rotated into the principal axes. The sound emission is strongest in the direction of the largest normal stress component and weakest in the direction of the smallest one.

Also shown is the OASPL directivity as predicted by a statistical model based on Lighthill's acoustic analogy.[1] The statistical model is a modified version of the expressions presented by Ribner.[3]

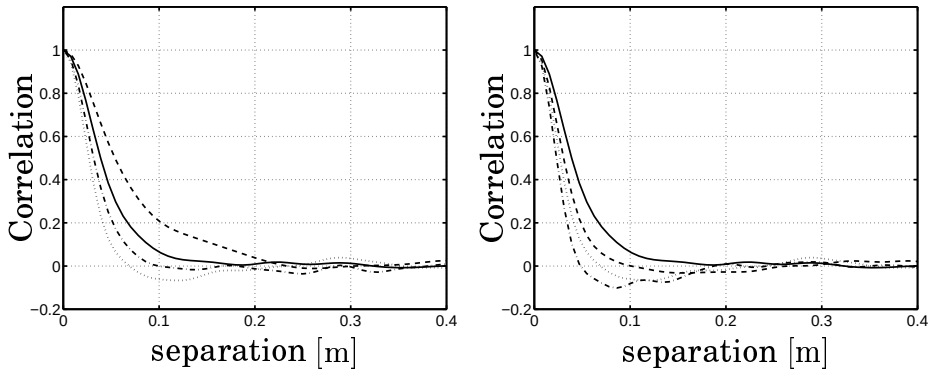


(a) $x^*$-direction (b) $y^*$-direction

Figure 5.11: Two point correlations. Dashed line: longitudinal anisotropic; solid line: longitudinal isotropic; dash-dotted line: transversal anisotropic; dotted line: transversal isotropic

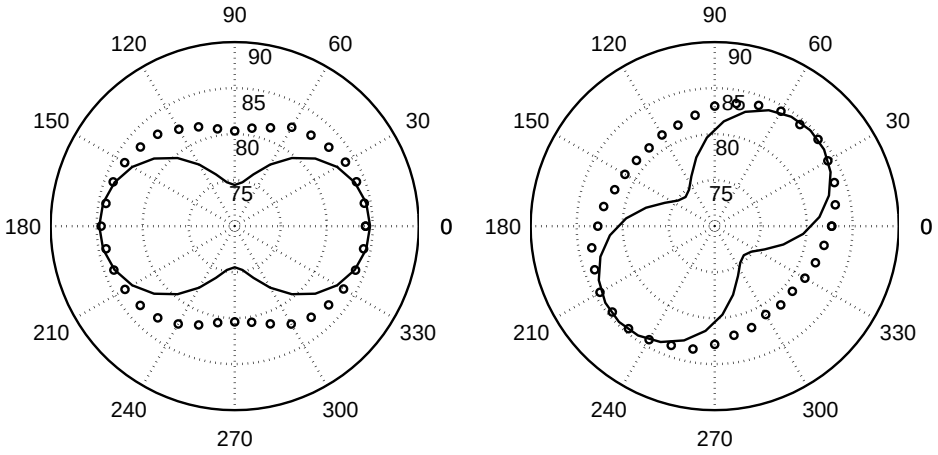

(a) Case 1 (b) Case 2

Figure 5.12: OASPL in $xy$-plane at radius $R = 100$ for angles $\theta = 0 : 10 : 360$ degrees. Circles: SNGR method; solid line: statistical model.

One can see that the direction of the sound directivity is the same for the numerical results and the statistical model. The degree of directivity in terms of OASPL is however twice as large for the statistical model compared to the numerical results.

The reason for the difference in the sound emission directivity lev-

els between the numerical results and the statistical model is unclear. The expression of the velocity correlation tensor used in the statistical model is a simple modification of the isotropic correlation tensor by Batchelor[57] and might be a too crude model (see Paper III). The true degree of sound directivity from anisotropic homogeneous turbulence can not be deduced from the present results. A more accurate model (see Paper V) for the velocity correlation tensor is needed for evaluation of the results from the synthesized turbulence.

The $1/3$ octave power spectral density of the far-field pressure for case $1$ is shown in figure 5.13. Spectra are shown for observer locations $1$ and $10$ (see figure 5.9) equivalent to $0$ and $90$ degrees from the $x^*$-axis respectively. The spectral behaviour of the far-field sound also

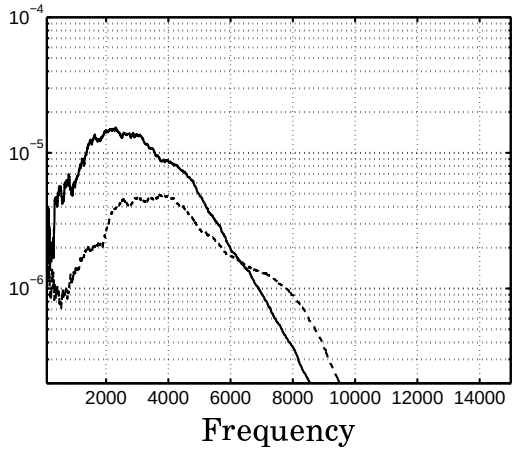


Figure 5.13: $1/3$ octave power spectral density of the far-field pressure. Case $1$. Solid line: observer point $1$ ($x^*$ direction); dashed line: observer point $10$ ($y^*$ direction)

reflects the anisotropy of the generated turbulence. The spectral content is shifted toward lower frequencies in the direction of the larger Reynolds stress in the principal axes and toward higher frequencies in the direction of the smaller Reynolds stress. There is also a large difference in the peak levels in the two spectra which is due to the difference in compactness of the turbulence in the two directions.

## 5.5 High Mach Number Subsonic Jets

One goal of the present work was to develop a modeling method for jet noise predictions which could be used as an industrial tool for acoustic design of jet engine exhaust nozzles. The hybrid method SNGR was found to be an interesting approach and showed promising results by Beachara *et al.*[21] and Bailly *et al.*[22,23] The method was in a developing stage and was believed to have the potential to be a good compromise between LES and statistical methods.

Three jets simulated using the SNGR method will be presented. These are high Reynolds number jets with jet exit Mach numbers of $0.75$ and $0.90$ respectively. The Mach $0.75$ jet was simulated both as cold and hot where the ratio of the temperature at the jet exit and the ambient fluid were $T_j/T_{amb} = 1$ and $T_j/T_{amb} = 2$ respectively. The flow conditions for the three jets are shown in table 5.4.

| Case | $M075c$ | $M075h$ | $M090c$ | |
|---|---|---|---|---|
| $M_j$ | 0.75 | 0.75 | 0.90 | |
| $T_j/T_{amb}$ | 1.0 | 2.0 | 1.0 | |
| $h_{0j}$ | 321841 | 611137 | 336162 | J/kg |
| $p_{0j}$ | 147116 | 122685 | 171329 | Pa/m$^2$ |
| $\rho_{amb}$ | 1.2256 | 1.2256 | 1.2256 | kg/m$^3$ |
| $T_{amb}$ | 288 | 288 | 288 | K |
| $D_j$ | 0.05 | 0.05 | 0.05 | m |

Table 5.4: Flow parameters for the simulated jet cases. subscripts $(\cdot)_j$ and $(\cdot)_{amb}$ denote jet exit and ambient conditions respectively.

The cold Mach $0.75$ jet has been used when evaluating the developments of the proposed SNGR method. As a test of the generality of the proposed SNGR method the hot Mach $0.75$ jet and the Mach $0.90$ jet were simulated. Data from LES[58] and measurements[15] of the same jets are used to evaluate the results from the proposed SNGR method. Some results from the simulations will be given below. For more details see Papers II and IV.[24,26]

### 5.5.1 Near-field Calibrated Results

The first approach in Paper II[24] to calibrate the model parameters was to compare the near-field statistics of the synthesized turbulence to that of LES solutions of the same flow. The main parameters were

the length scale factor $f_L$ and the time scale factor $f_\tau$ which determine the length and time scales of the synthesized turbulence based on the RANS solution (see equations 3.10 and 3.14).

This calibration was done using two-point space-time correlations in the shear layer of the jet. Correlations computed from LES by Andersson *et al.*[58] were compared to those from the synthesized turbulence in the proposed SNGR method. These two-point space-time correlations in the axial directions in the shear layer computed from the LES and the synthesized turbulence are shown in figure 5.14. The length and time scale factors were calibrated to $f_L = 1/6$ and $f_\tau = 1.0$ respectively in these near-field calibrated results. From the space-time correlations the spatial two-point correlation and the convected reference field autocorrelation were computed. These are shown in figure 5.15 and show that the LES and synthesized turbulence are in good agreement both in length and time scales.

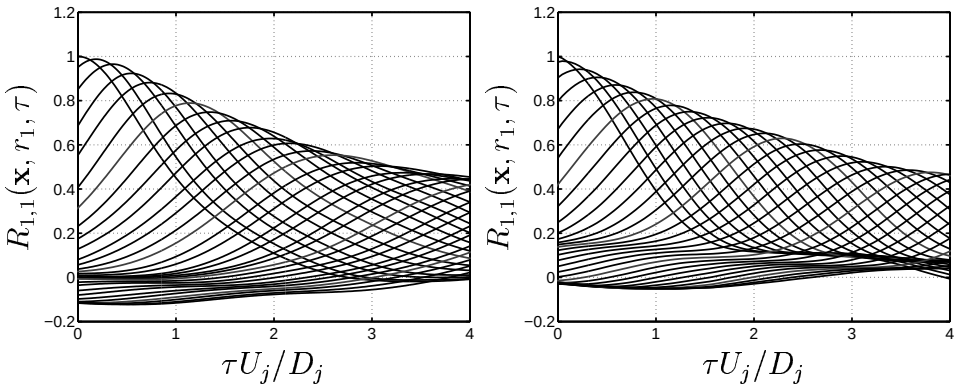


(a) LES by Andersson (b) Synthesized velocity field

Figure 5.14: Two-point space-time correlation[24] in the axial direction at $(x/D_j, r/D_j) = (10, 0.5)$. Different lines represent separations $r_1/D_j = [0 : 0.1 : 3]$

The far-field sound prediction was however not in the same good agreement with the measurements of the same jet when these factors were used. The OASPL directivity for the cold Mach $0.75$ jet at $r/D_j = 30$ and $r/D_j = 50$ are shown in figure 5.16 and the $1/3$-octave power spectral density of the far-field pressure at $(r/D_j, \theta) = (30, 30)$ is shown in figure 5.17(a). Shown are also the same quantities computed from the measurements by Jordan and Gervais.[15] As can be seen, the sound pressure level is overpredicted by about $10$ dB and the spectral peak is

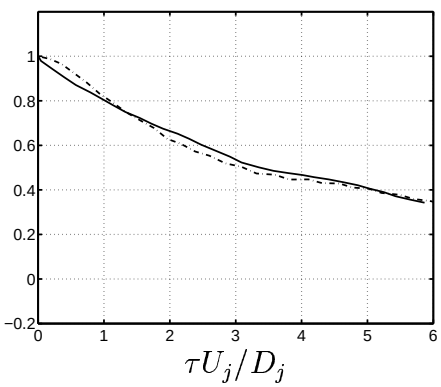


(a) Convected reference field auto-correlation

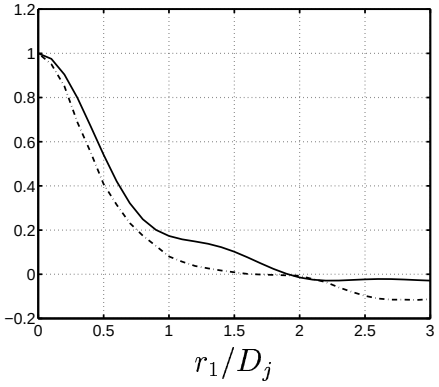


(b) Two-point correlation

Figure 5.15: Correlations at $(x/D_j, r/D_j) = (10, 0.5)$. Solid line: synthesized velocity field, dash-dotted line: LES by Andersson

at a too high frequency compared to the measurements.

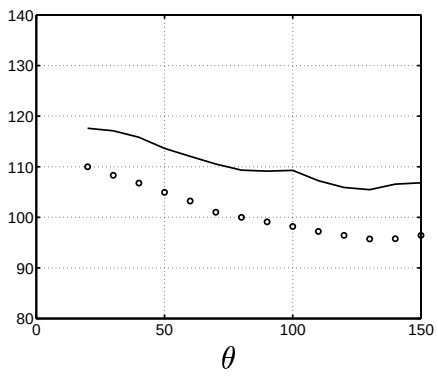


(a) $r/D_j = 30$

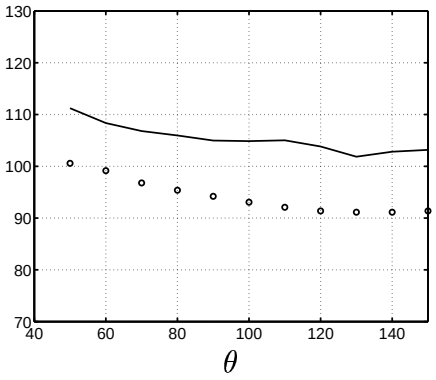


(b) $r/D_j = 50$

Figure 5.16: OASPL (dB) at $r/D_j = 30$ and $r/D_j = 50$ for different angles $\theta$ from jet axis direction. Solid line: present method; circles: measurements

The errors in the far-field results could either be related to the use of the inhomogeneous linearized Euler equations as an acoustic analogy in combination with the Kirchhoff method or related to some property of the synthesized turbulence.

To validate the ILEE as an analogy in Paper II,[24] the far-field acous-

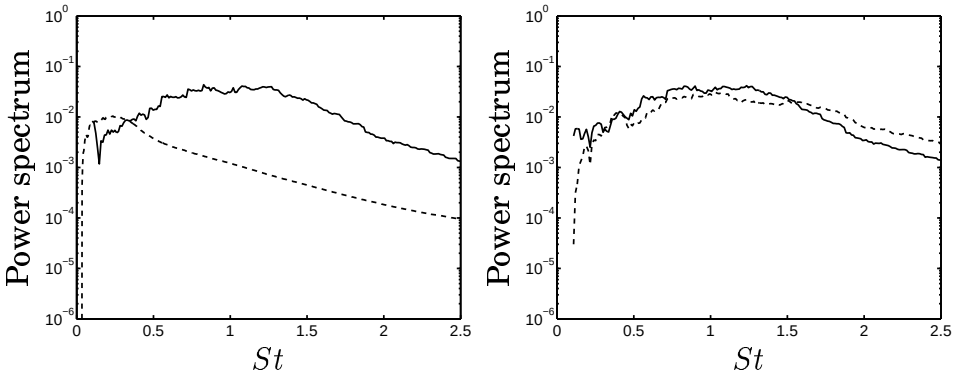


(a) Solid line: present method; dashed line: measurements

(b) Solid line: Kirchhoff method; dashed line: Lighthill's analogy

Figure 5.17: $1/3$-octave power spectral density of pressure in an observation point at $(r/D_j, \theta) = (30, 30)$. Near-field calibrated results.

tic solution was computed in two different ways. The proposed SNGR method including the Kirchhoff integral method was used (as presented above) as well as the double time derivative formulation of the Lighthill acoustic analogy, see Crighton.[59] The Lighthill analogy solution was computed directly from the synthesized velocity field, see figure 5.18 whereas the Kirchhoff solution was based on the solution to the linearized Euler equations and thus included all steps in the present method.

Figure 5.17(b) shows the $1/3$-octave power spectral density of the far-field pressure computed using the Lighthill analogy and the Kirchhoff method. The far-field spectra are almost identical except for very low frequencies where there is presence of disturbances in the Kirchhoff method solution originating from hydrodynamic instabilities in the solution of the linearized Euler equations. The spectral peaks are located at the same place and the levels are the same in the two curves. The conclusion is that the linearized Euler equations with source terms presented here indeed produce the correct sound field associated with a specified turbulence source field. This confirms the results from the 2D mixing layer in section 5.2. The cause of the poor agreement with measurements in the far-field noise prediction is thus not related to the inhomogeneous linearized Euler equations but must be related to some property of the synthesized turbulence.

The reason for the shift in the spectral peak in figure 5.17(a) was

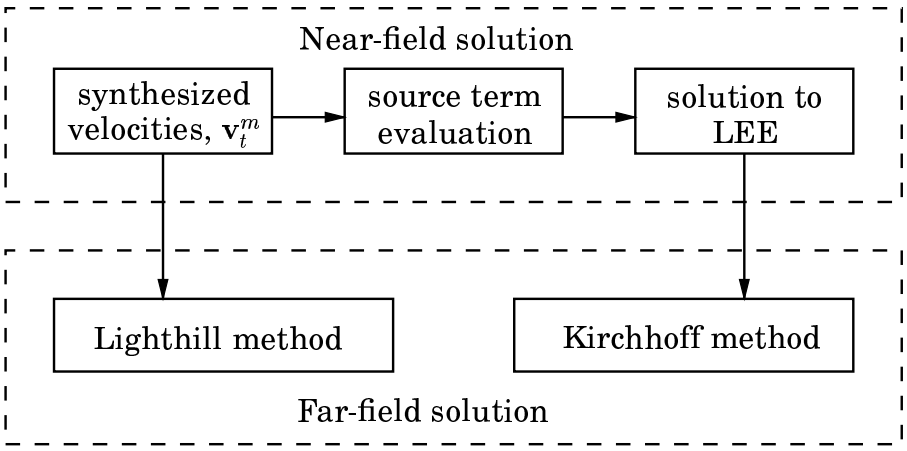


Figure 5.18: Near-field to far-field solutions using Lighthill and Kirchhoff methods.

found to be related to incorrect length scales in the generated turbulence. Even if the two-point correlations in figure 5.15(b) are in good agreement with the LES, the synthesized turbulence does not contain the correct length scales. This is due to poor resolution in the generation of synthesized turbulence, see Paper II.[24] The conclusion in Paper II was that the generated turbulence should have a larger length scale factor $f_L$ and thus a larger two-point correlation than the LES since the spectrum used as model for the distribution of kinetic energy in the turbulence has been truncated in the higher wave numbers.

The reason for the overprediction of the sound pressure level was further investigated in Paper II.[24] The effects of divergence of the source field, the convection operator and the time scales in the synthesized turbulence were evaluated. The time scales in the synthesized source field were found to affect the level of the emitted sound by changing the compactness of the turbulence, but both the convection operator and the existence of divergence in the turbulence had minor effects on the level of the emitted sound. It has furthermore been suspected that the reason could be due to non-compact sources associated with modes with low wave numbers and high frequencies in the synthesized turbulence, see Ref. [60]. This low wave number – high frequency property of the synthesized turbulence is present in the generation of the synthesized turbulence due to the time filter which is used to develop the turbulence in time (equation 3.13). The overprediction of the emitted sound in the present SNGR method is though not related to this effect as can be seen in Fig. 5.19. The figure shows the $1/3$ octave

power spectral density of the far-field pressure from synthesized homogeneous isotropic turbulence generated in a box. The computational setup was the same as for the box-turbulence in the previous section except that in the present test all modes in the synthesized turbulence had the same wave length. Two cases were computed with wave numbers of length $k = 27$ rad/m and $k = 54$ rad/m respectively.

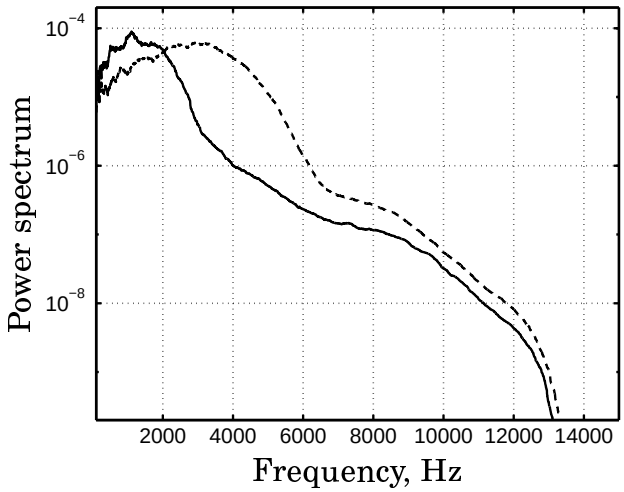


Figure 5.19: $1/3$ octave power spectral density of the far-field pressure. Solid line: $k = 27$; dashed line: $k = 54$

The spectra show a peak at frequencies corresponding to the wavelengths of the turbulence in each case. There is also noise generated at frequencies lower than the peak frequency which is attributed to aliasing effects and non-linearity of the source terms to the linearized Euler equations. There is no increase in the noise from the low wave number case at high frequencies though, which would be the case if there was a non-compact source associated with low wave numbers with high frequencies in the generation of the synthesized turbulence.

The test does however show that there is a direct relation between the frequencies in the generated sound and the wave lengths of the synthesized turbulence. This relation is due to that the time filter (Eq. 3.13) which filters the velocity field only has one time scale which acts on all wave numbers. The filter also allows fluctuations at all resolvable frequencies, with most energy at low frequencies and a quadratic decrease in energy at high frequencies, see figure 3.4. Relevant for the sound generation is that there is always a matching frequency for every wave number such that the noise generation is very efficient. This strong relation is probably not the case in real turbulence which

is much less efficient as a noise generator.

The correct values of the length scale factor and time scale factor were due to the truncation of the model spectrum in the generation of synthesized turbulence difficult to determine based on the near-field correlations. As an alternative approach, the factors were instead calibrated based on the far-field noise predictions. A third parameter called the amplitude factor $f_A$ (see equation 3.13) was also added to calibrate the amplitude of the far-field noise level by modifying the amplitude of the generated turbulence.

The effect of the far-field calibrated values of $f_L$, $f_\tau$ and $f_A$ on the near-field of the synthesized turbulence is that spatial correlations no longer are in agreement with the LES data due to increased length scale factor and that the kinetic energy of the generated turbulence is lowered by the amplitude factor (see Papers II and IV[24,26]).

### 5.5.2 Far-field Calibrated Results

In Papers II and IV[24,26] results are presented from the proposed SNGR method where the parameters in the model are calibrated based on the agreement with measurements in the far-field noise predictions. In the results below the model parameters have been calibrated to measurements by Jordan and Gervais[15] for the cold Mach $0.75$ jet. The results from the heated Mach $0.75$ and the Mach $0.90$ jets are used to evaluate the generality of the method. The length and time factors were set to $f_L = 1$, $f_\tau = 1$ respectively for the far-field calibrated results.

#### Anisotropy

A method to generate anisotropic synthesized turbulence was developed in Paper III[25] and the method was applied to the same cold Mach $0.75$ jet as above in Paper IV.[26] The main questions related to the near-field of the new anisotropic method were if the two equation $k-\varepsilon$ RANS model would be able to predict an anisotropic Reynolds stress field which agreed with the LES data of the same jet and if the synthesized turbulence could simulate this inhomogeneous anisotropic turbulence field.

The normalized normal Reynolds stress tensor components in the shear layer of the jet from the LES and the RANS are shown in figure 5.20. The results from the LES show a larger difference between the different components, indicating that the RANS model can not predict

the anisotropy of a strong shear flow. What is then not taken into account however is the role of the cross stresses in the Reynolds stress tensor. Figure 5.21 shows the same normalized Reynolds stress terms but expressed in a coordinate system aligned with the principal axes of each stress tensor. In this principal coordinate system, the cross stresses are zero and all effects of anisotropy in the tensor are manifested by the normal stresses, see Papers III and IV[25,26] for details. One can now see that the degree of anisotropy in the RANS and the LES are really of the same order.

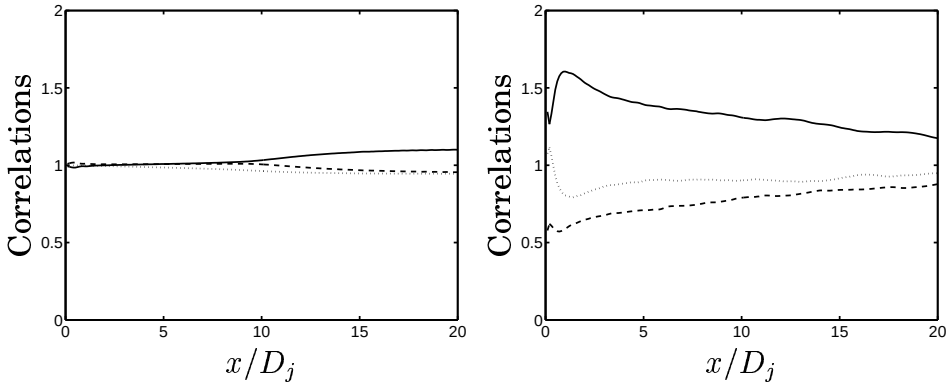


(a) RANS (b) LES

Figure 5.20: Normalized normal Reynolds stress tensor components in shear layer, $(y, z)/D_j = (0.5, 0)$. In $xy$-coordinates. Solid line: $\mathbf{a}_{11}$; dashed line: $\mathbf{a}_{22}$; dotted line: $\mathbf{a}_{33}$.

The synthesized anisotropic turbulence has been shown to be able to simulate a specified anisotropic Reynolds stress tensor in a homogeneous case, see Paper III.[25] A validation that the anisotropy of a shear flow can be simulated is shown in figure 5.22 where the $\overline{u'v'}$ correlation from the RANS and the synthesized turbulence in the shear layer of the cold Mach $0.75$ jet are plotted. The cross-correlation from the synthesized turbulence is in good agreement with that of the RANS solution. More details on the near-field turbulence of the Mach $0.75$ jet in terms of length scale anisotropy is presented in Paper IV.[26] It is shown that the length scale anisotropy of the synthesized turbulence is in agreement with the model theory.

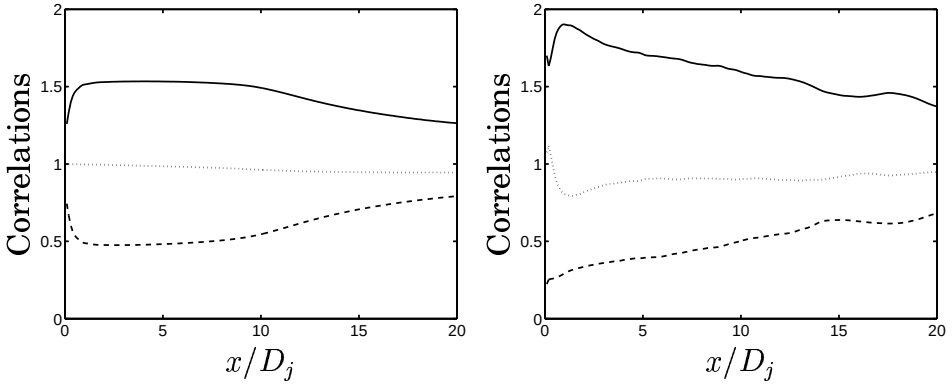


(a) RANS (b) LES

Figure 5.21: Normalized normal Reynolds stress tensor components in shear layer, $(y, z)/D_j = (0.5, 0)$. In $xy^*$-coordinates. Solid line: $\mathbf{a}^*_{11}$; dashed line: $\mathbf{a}^*_{22}$; dotted line: $\mathbf{a}^*_{33}$.

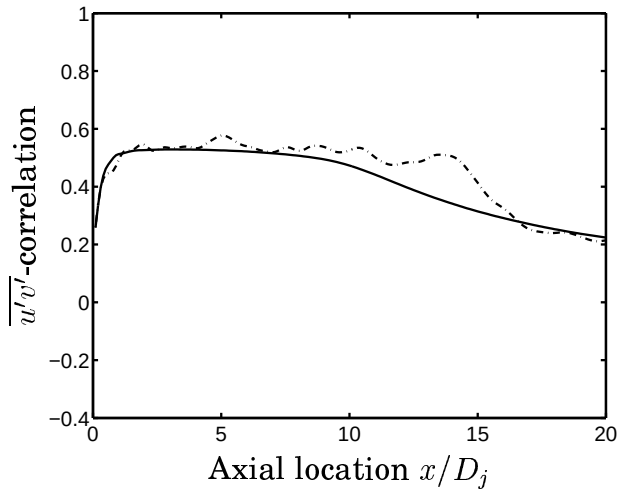


Figure 5.22: Normalized $\overline{u'v'}$-correlation in the shear layer, $(y, z)/D_j = (0.5, 0)$. Solid line: RANS; dash-dotted line: anisotropic SNGR sampling

## Far-field Results

The OASPL directivity from the cold Mach $0.75$ jet for the locally isotropic and the anisotropic SNGR methods are shown in figure 5.23. The amplitude factor was in both cases set to $f_A = 0.316$. The results show that the directivity of the predictions are about the same even if the generated sound is increased in the results from the anisotropic

model. The anisotropy in the model does evidently increase the emitted sound. A new calibration of the amplitude factor was performed in Paper IV to correct the emitted noise levels and all results below from the anisotropic model were produced using $f_A = 0.265$.

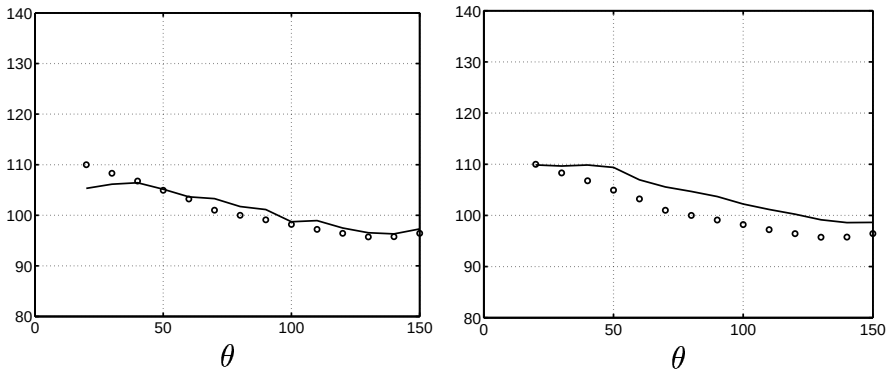


(a) Isotropic (b) Anisotropic

Figure 5.23: OASPL (dB) at $r/D_j = 30$ for different angles $\theta$ from jet axis direction. Cold Mach $0.75$, $f_A = 0.316$ Solid line: present method; circles: measurements

The OASPL directivity for the cold and heated Mach $0.75$ jets and the Mach $0.90$ jet using the anisotropic method are shown in figure 5.24. The OASPL directivities are generally in good agreement with the measurements except for angles below $\theta = 40$ degrees. The drop below this angle can be attributed to the open Kirchhoff surface in the downstream direction (see section 4.3). The trend from the cold Mach $0.75$ jet to the cold Mach $0.90$ jet in Figs. 5.24(a) and 5.24(b) is quite well captured and the agreement with the measurements are relatively good. This is however not the case for the change from the cold to hot Mach $0.75$ jets in Fig. 5.24(a). The reason for this might be twofold. The first reason can be related to that the synthesized source field in the SNGR method only contains velocity fluctuations and that sources of sound related to high temperatures are thus not taken into account. The second reason can be related to that the simulation of the hot Mach $0.75$ case is considerably shorter than for the other cases, and the statistics are thus based on fewer samples ($10\,000$ for the hot jet and $30\,000$ for the cold). The reason for this were disturbances which grew rapidly in the hot jet simulation. The cold jets are convectively unstable,[33] meaning that there are unstable regions in the jets but that the

disturbances are convected downstream and thus leaving the region of the original instability. The hot jet however, seems to be absolutely unstable.[33] The disturbances from the unstable regions are not convected away fast enough and the disturbances can grow without bound due to the linearity of the linearized Euler equations. The results from the hot Mach $0.75$ jet are therefore not statistically reliable. If the hot jet is to be simulated using the present approach, a modified set of equations would be desirable. Such equations could for example be the acoustic perturbation equations (APE)[36,37] which are reported to be stable for arbitrary inhomogeneous mean flows.

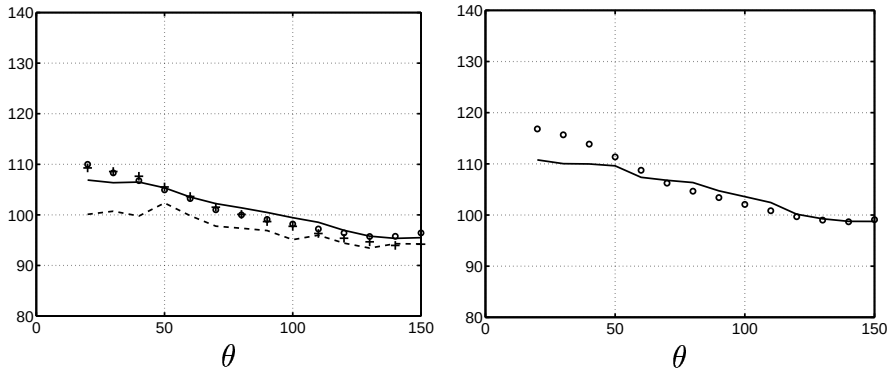


(a) Anisotropic Mach $0.75$ cold and hot

(b) Anisotropic Mach $0.90$

Figure 5.24: OASPL (dB) at $r/D_j = 30$ for different angles $\theta$ from jet axis direction. $f_A = 0.265$ Solid line: present method cold; Dashed line: present method hot ; circles: measurements cold; plus signs: measurements hot

Figures 5.25 and 5.26 show the $1/3$ octave power spectral density of the far-field pressure from the isotropic and anisotropic simulations of the cold Mach $0.75$ jet. The observer positions in figures 5.25 and 5.26 are $(r/D_j, \theta) = (30, 30)$ and $(r/D_j, \theta) = (30, 90)$ respectively.

The spectral results at $30$ degrees from the jet axis in figure 5.25 are improved compared to the near-field calibrated results in figure 5.17(a) with a shift in the spectral energy content toward lower frequencies in the far-field calibrated simulation. The two spectra in figure 5.25 indicate that the far-field noise spectrum for the anisotropic simulation is in somewhat better agreement with the measurements than the isotropic simulation even though both the isotropic and anisotropic results still show a lack of energy at low frequencies. The results at $90$

degrees from the jet axis in figure 5.26 are in good agreement with the measurements. The difference in the shape of the spectra between the isotropic and anisotropic cases is small.

The anisotropy which is evident in the near-field statistics above is not as pronounced in the far-field results. A reason for this might be that most of the directivity of a jet is a result of the convective amplification[1] in the sound generation and the refraction of the generated sound. The convective amplification increases the sound emission in the flow direction and lowers the emission in the up-stream direction. The refraction has the effect (mainly for high frequencies) of directing the sound emitted down-stream out from the axial direction toward the radial direction. These effects are the same for the anisotropic and isotropic simulations and if the directivity in the sound emission due to anisotropy is not strong enough, the resulting sound field directivity is masked by the convective amplification and the refraction.

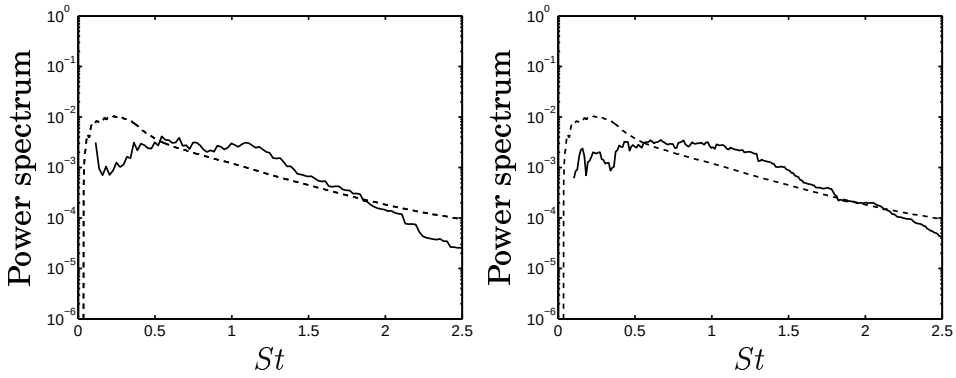


(a) Isotropic $f_A = 0.316$ (b) Anisotropic $f_A = 0.265$

Figure 5.25: $1/3$-octave power spectral density of pressure in an observation point at $(r/D_j, \theta) = (30, 30)$. Cold Mach $0.75$ Solid line: present method; dashed line: measurements

The results from these jet noise computations using the proposed SNGR method show that the method has the capability to predict varying flow conditions in terms of jet exit Mach number, but the absolute level of the generated sound does need calibration.

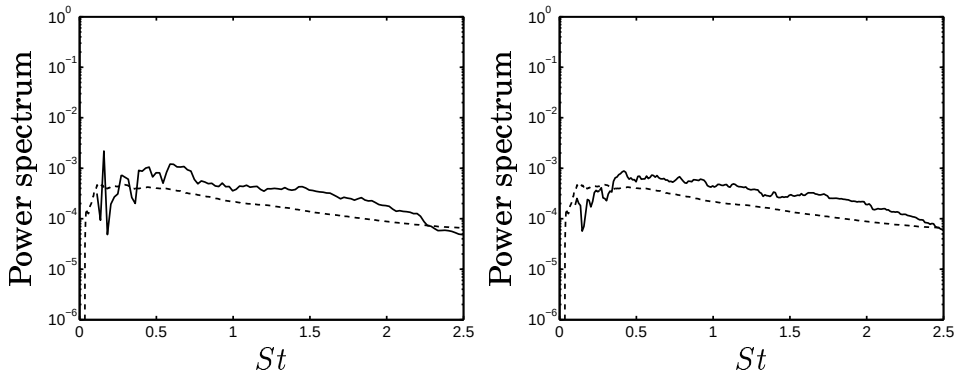


(a) Isotropic $f_A = 0.316$ (b) Anisotropic $f_A = 0.265$

Figure 5.26: $1/3$-octave power spectral density of pressure in an observation point at $(r/D_j, \theta) = (30, 90)$. Cold Mach $0.75$ Solid line: present method; dashed line: measurements

## 5.6 Classical Theory

Statistical models for turbulence-generated noise have been developed ever since 1952 when Sir James Lighthill presented the first of two papers on aerodynamically generated sound.[1,2] In these models, the two-point velocity correlation tensor is the basis of the statistical representation of the turbulence structure and is strongly related to the sound emission directivity.

In 1969 Ribner[3] used isotropic turbulence theory by Batchelor[57] to model the velocity correlation tensor in the framework of Lighthill's analogy in order to estimate the noise generated by a jet. In this presentation the one local length scale and turbulence intensity required to be specified in the isotropic theory were taken as the axial longitudinal length scale and the intensity of the axial velocity component respectively. The anisotropy of the turbulence in a real jet was thus not properly taken into account. This model has also been evaluated by others, e.g. Bailly *et al.*[14]

In 1973 Goldstein and Rosenbaum[11] introduced anisotropy in the model of the velocity correlation tensor by considering axisymmetric turbulence developed by Chandrasekhar.[61] Other models based on the same axisymmetric theory have been presented by Khavaran,[12] Bechara *et al.*,[13] Bailly *et al.*,[14] Devenport *et al.*[16] and Jordan and Gervais.[15] Even though proper anisotropy can not be taken into account, this is an improvement over the isotropic model. The choice of local axis of symmetry is though arbitrary since the turbulence is not really axisymmetric in any direction (except on the jet centerline if the jet is geometrically axisymmetric). The same arbitrariness holds for the degree of anisotropy in the axisymmetric model.

An attempt to construct a more general model of the velocity correlation tensor $R_{ij}(\mathbf{y}, \mathbf{r})$ based on the homogeneous turbulence assumption but including anisotropy in turbulence intensities and length scales was developed by Billson *et al.*[49] (Paper V). The same derivation is also given in this section and the results from Paper V are presented.

A functional form of $R_{ij}(\mathbf{y}, \mathbf{r})$ in terms of six one-dimensional correlation functions will be derived. A closure model where these correlation functions are related to single point statistics will also be presented. This closure is however preliminary and is not to be taken as a ready-to-use model.

### 5.6.1 Anisotropic Model of the Two-point Velocity Correlation Tensor

The strategy is to express the second-order two-point velocity correlation tensor $R_{ij}(\mathbf{r})$ in terms of a correlation $\widetilde{R}_{ij}(\widetilde{r}_1)$ where $\widetilde{r}_1$ denotes a separation in a coordinate system $\widetilde{\mathbf{x}}$ which has $\widetilde{x}_1$ parallel to $\mathbf{r}$. Define two coordinate systems $\mathbf{x} = (x_1, x_2, x_3)$ and $\widetilde{\mathbf{x}} = (\widetilde{x}_1, \widetilde{x}_2, \widetilde{x}_3)$ with the same origin, see figure 5.27. Let $\widetilde{\mathbf{x}}$ be rotated compared to $\mathbf{x}$ such that $\widetilde{x}_1$ is parallel to a separation $\mathbf{r} = (r_1, r_2, r_3)$ expressed in the $\mathbf{x}$ coordinate system. One possible orthonormal set of rotation vectors relating $\mathbf{x}$ to $\widetilde{\mathbf{x}}$ is then

$$\begin{aligned} \mathbf{e_1} &= \left(\frac{r_1}{r}, \frac{r_2}{r}, \frac{r_3}{r}\right)^T \\ \mathbf{e_2} &= \left(\frac{-r_2}{r_h}, \frac{r_1}{r_h}, 0\right)^T \\ \mathbf{e_3} &= \left(\frac{r_1 r_3}{r r_h}, \frac{r_2 r_3}{r r_h}, -\frac{r_h^2}{r r_h}\right)^T \end{aligned} \tag{5.10}$$

where $r = (r_1^2 + r_2^2 + r_3^2)^{(1/2)}$ and $r_h = (r_1^2 + r_2^2)^{(1/2)}$ respectively. A rotation matrix $\mathbf{E} = (\mathbf{e_1}, \mathbf{e_2}, \mathbf{e_3})$ will relate $\mathbf{x}$ to $\widetilde{\mathbf{x}}$ and vise versa as

$$\begin{aligned} \mathbf{x} &= \mathbf{E}\,\widetilde{\mathbf{x}} \\ \widetilde{\mathbf{x}} &= \mathbf{E}^T\,\mathbf{x} \end{aligned} \tag{5.11}$$

and the spatial separation $\widetilde{\mathbf{r}} = (\widetilde{r}_1, \widetilde{r}_2, \widetilde{r}_3)$ will be related to $\mathbf{r}$ as

$$\widetilde{\mathbf{r}} = \mathbf{E}^T\,\mathbf{r} = (\mathbf{e_1}, \mathbf{e_2}, \mathbf{e_3})^T \mathbf{r} = (r, 0, 0)^T \tag{5.12}$$

i.e. any separation $\mathbf{r}$ results in a separation in the first component $\widetilde{r}_1$ in the coordinate system $\widetilde{\mathbf{x}}$. For simplicity the notation will here after be changed to tensor notation. The rotation matrix will be denoted by $E_{ij} = \mathbf{E}$.

With the assumption of homogeneous turbulence a velocity correlation tensor can be defined in the $\mathbf{x}$ coordinate system as

$$R_{ij}(\mathbf{r}) = \overline{u_i(\mathbf{x}) u_j(\mathbf{x} + \mathbf{r})} \tag{5.13}$$

where the overline $\overline{(\cdot)}$ denotes an appropriate average and $u_i$, $u_j$ are velocity components. For homogeneous turbulence there is no dependence of $\mathbf{x}$ for $R_{ij}(\mathbf{r})$. By using the rotation matrix $E_{ij}$, the correlation tensor $R_{ij}(\mathbf{r})$ can then be expressed as

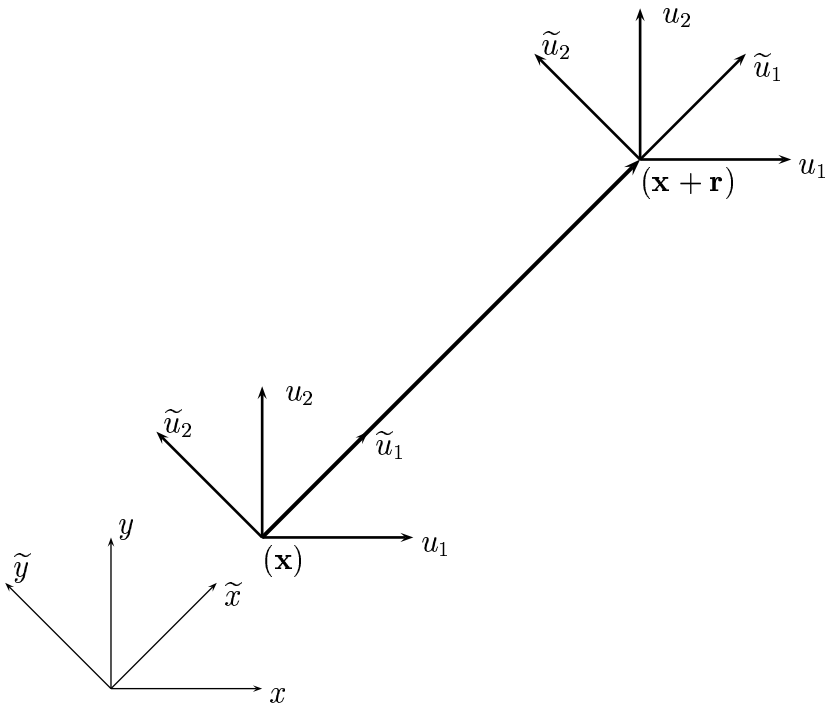


Figure 5.27: Original and rotated coordinate systems $\mathbf{xy}$ and $\widetilde{\mathbf{x}}\widetilde{\mathbf{y}}$ (in two dimensions). Velocity components $u_i$ and $\widetilde{u}_j$ in respective coordinate system.

$$R_{ij}(\mathbf{r}) = E_{ik}\, E_{jl}\, \widetilde{R}_{kl}(\widetilde{\mathbf{r}}) = E_{ik}\, E_{jk}\, \widetilde{R}_{kl}(r,0,0) \tag{5.14}$$

where $\widetilde{R}_{ij}(r,0,0)$ are correlations of pairs of velocity components $\widetilde{u}$, $\widetilde{v}$ and $\widetilde{w}$ with separation in the $\widetilde{r}_1$-direction. These can be expressed individually as

$$
\begin{aligned}
\widetilde{R}_{11}(r,0,0) &= -\widetilde{\boldsymbol{\tau}}_{11}\widetilde{f}(r) \\
\widetilde{R}_{22}(r,0,0) &= -\widetilde{\boldsymbol{\tau}}_{22}\widetilde{g}(r) \\
\widetilde{R}_{33}(r,0,0) &= -\widetilde{\boldsymbol{\tau}}_{33}\widetilde{h}(r) \\
\widetilde{R}_{12}(r,0,0) &= -\widetilde{\boldsymbol{\tau}}_{12}\widetilde{f}_{12}(r) \\
\widetilde{R}_{13}(r,0,0) &= -\widetilde{\boldsymbol{\tau}}_{13}\widetilde{f}_{13}(r) \\
\widetilde{R}_{23}(r,0,0) &= -\widetilde{\boldsymbol{\tau}}_{23}\widetilde{f}_{23}(r)
\end{aligned}
\tag{5.15}
$$

where $\widetilde{f}(r)$ is the longitudinal velocity correlation function and $\widetilde{g}(r)$ and $\widetilde{h}(r)$ are the transversal correlation functions related to $\widetilde{v}$ and $\widetilde{w}$ respectively. $\widetilde{f}_{12}(r)$, $\widetilde{f}_{13}(r)$ and $\widetilde{f}_{23}(r)$ are the corresponding cross correlation functions. The assumption of homogeneous turbulence also ensures that $\widetilde{R}_{ij}(r,0,0) = \widetilde{R}_{ji}(r,0,0)$. The normalization is done by the correlation tensor at zero separation (i.e., the Reynolds stress tensor $\widetilde{\boldsymbol{\tau}}_{ij}$), which is computed from the stress tensor in the original coordinate system $\mathbf{x}$ as

$$
\widetilde{\boldsymbol{\tau}}_{ij} = E_{ki}\, E_{lj}\, \boldsymbol{\tau}_{kl} \tag{5.16}
$$

Equations 5.14 to 5.16 show that the two-point velocity correlation tensor $R_{ij}(\mathbf{r})$ can be expressed in terms of six scalar correlation functions and the Reynolds stress tensor. How well equations 5.14 and 5.15 represent a true homogeneous anisotropic turbulence field lies in the accuracy of the modeling of the scalar functions.

The true functional forms of the scalar functions for a homogeneous anisotropic velocity field is not known. A simple model of the correlation functions which is based on the isotropic model will nevertheless be presented. The longitudinal correlation function can for example be modeled as

$$
\widetilde{f}(r) = e^{-\pi r^2/4L^2} \tag{5.17}
$$

where $L$ is the longitudinal length scale in the direction of the spatial separation $\widetilde{r}_1$. Following the expressions for isotropic turbulence[57] and using equation 5.17 the transversal correlation functions can be related to the longitudinal as

$$
g(r) = h(r) = f(r) + \frac{r}{2}\frac{df(r)}{dr} = \frac{L^2 - r^2}{L^2} e^{-r^2/L^2} \tag{5.18}
$$

For simplicity, the cross correlation functions are modeled in the same way as the longitudinal correlation function, i.e.

$$\widetilde{f}_{12}(r) = \widetilde{f}_{13}(r) = \widetilde{f}_{23}(r) = e^{-r^2/L^2} \tag{5.19}$$

The functional form of the correlation functions and especially their relative shapes (equations 5.18 and 5.19) are not validated to any anisotropic turbulence. Further work is needed to develop models for these functions for a general homogeneous anisotropic turbulence.

### Length scale anisotropy

Recent results from the SNGR (Paper III)[25] method where anisotropy has been included in the synthesis of artificial turbulence suggest that the length scale of the turbulence in different directions can be deduced from the individual components of the Reynolds stress tensor. The results indicate that the length scale in a certain direction is related to the corresponding relative magnitude of the normalized normal stress tensor component. The following relation can for example be used as a model of the length scale anisotropy for the length scale in the $\widetilde{r}_1$-direction.

$$L = L^{iso} \left( \frac{3\widetilde{\boldsymbol{\tau}}_{11}}{\widetilde{\boldsymbol{\tau}}_{11} + \widetilde{\boldsymbol{\tau}}_{22} + \widetilde{\boldsymbol{\tau}}_{33}} \right)^{1/2} \tag{5.20}$$

where $L^{iso}$ is the longitudinal length scale in limit of isotropic turbulence.

Equations 5.14 to 5.20 together with the rotation matrix $\mathbf{E} = E_{ij}$ defined by the vectors in equation 5.10 can be used to model a general anisotropic two-point correlation tensor $R_{ij}(\mathbf{r})$ for homogeneous turbulence. The full expressions for the different components of the correlation tensor are quite large and are thus not given here. For the isotropic case the cross correlation functions $\widetilde{f}_{12}(r)$, $\widetilde{f}_{13}(r)$ and $\widetilde{f}_{23}(r)$ as well as the off-diagonal components of the Reynolds stress tensor will be analytically zero and equations 5.14 and 5.15 reduce to the isotropic model of $R_{ij}(\mathbf{r})$ given by Batchelor.[57]

$$R_{ij}(\mathbf{r}) \rightarrow R_{ij}^{iso}(\mathbf{r}) = \overline{u^2} \left( \frac{f(r) - g(r)}{r^2} r_i r_j + g(r)\delta_{ij} \right) \tag{5.21}$$

The accuracy of the model lies in the correctness of the expressions for the correlation functions in equations 5.17 to 5.19 and the length scale anisotropy in equation 5.20. One flaw of the model is that when

the expressions in equations 5.17 to 5.20 are used to model the correlation functions, the resulting two-point correlation tensor $R_{ij}(\mathbf{r})$ will not fulfill the continuity condition

$$\frac{\partial R_{ij}(\mathbf{r})}{\partial r_i} = \frac{\partial R_{ij}(\mathbf{r})}{\partial r_j} = 0 \tag{5.22}$$

These relations can be used to constrain the models of the correlation functions in order to construct a more accurate model of the two-point velocity correlation tensor.

### 5.6.2 Preliminary Results

As $R_{ij}(\mathbf{r})$ is a function of the three-dimensional separation vector $\mathbf{r}$ it is difficult to illustrate. For special cases though the general features can be viewed in suitably chosen planes. Figures 5.28 to 5.32 show correlation fields from the proposed anisotropic $R_{ij}(\mathbf{r})$ in the $xy$-plane for $z = 0$. The interesting correlations in this slice are $R_{11}$, $R_{22}$, $R_{12}$ where the dependence of $\mathbf{r}$ is omitted in the notation below.

The different cases are described in tables 5.5 and 5.6. They correspond to one isotropic turbulence case (case 1) and four anisotropic turbulence cases (case 2-4). The degree of anisotropy in cases 2-4 is the same but the principal axes of $\boldsymbol{\tau}_{ij}$ in cases 4 and 5 are rotated in the $xy$ plane by 45 degrees compared to cases 2 and 3. The modeled length scale anisotropy (with $L^{iso} = 0.1$) is used in cases 3 and 5 but a constant length scale ($L = 0.1$) is used in cases 2 and 4. The Reynolds stress tensors used for the different cases are given in table 5.6.

| Case | Description |
|---|---|
| 1 | Isotropic |
| 2 | Anisotropic, Principal axes of $\boldsymbol{\tau}_{ij}$ 0 degrees, $L$ isotropic |
| 3 | Anisotropic, Principal axes of $\boldsymbol{\tau}_{ij}$ 0 degrees, $L$ anisotropic |
| 4 | Anisotropic, Principal axes of $\boldsymbol{\tau}_{ij}$ 45 degrees, $L$ isotropic |
| 5 | Anisotropic, Principal axes of $\boldsymbol{\tau}_{ij}$ 45 degrees, $L$ anisotropic |

Table 5.5: Case descriptions. Isotropic length scale denotes that equation 5.20 has not been used.

The isotropic reference case is plotted in figure 5.28, where $R_{11}$ and $R_{22}$ are identical but rotated by 90 degrees. They are positive with a Gaussian shape in the longitudinal direction but have a dip with a negative region in the transversal directions as prescribed by the

| Case | Reynolds stress tensor |
|---|---|
| 1 | $\boldsymbol{\tau}_{ij} = -[(400, 0, 0), (0, 400, 0), (0, 0, 400)]$ |
| 2, 3 | $\boldsymbol{\tau}_{ij} = -[(600, 0, 0), (0, 200, 0), (0, 0, 400)]$ |
| 4, 5 | $\boldsymbol{\tau}_{ij} = -[(400, 200, 0), (200, 400, 0), (0, 0, 400)]$ |

Table 5.6: Reynolds stress tensors $\boldsymbol{\tau}_{ij}$ expressed in $\mathbf{x}$ coordinate system

isotropic model. $R_{12}$ has two positive and two negative lobes and is zero on the coordinate axes.

With an anisotropy in case 2 where $\boldsymbol{\tau}_{11} > \boldsymbol{\tau}_{22}$ the corresponding two-point correlations experience the same relations as seen in figure 5.29. The general shapes of $R_{11}$, $R_{22}$ and $R_{12}$ are otherwise the same as for the isotropic case. With a length scale anisotropy (see equation 5.20) in case 3 the contours of $R_{11}$, $R_{22}$ and $R_{12}$ are separated in $x$-direction and compressed in $y$-direction.

In case 4, with the same degree of anisotropy as in case 2 and 3 but with the principal axes of $\boldsymbol{\tau}_{ij}$ rotated by 45 degrees about the $z$-axis; the $R_{11}$, $R_{22}$ and $R_{12}$ slices become as in figure 5.31. The $R_{11}$ and $R_{22}$ fields are slightly modified by the rotation of the stress tensor. The big difference is however the $R_{12}$ field in which the positive lobe is increased and the negative lobe is decreased both in magnitude and in size. Finally with length scale anisotropy included in case 5, the correlations are increased in the 45 degree direction and reduced at $-45$ degrees.

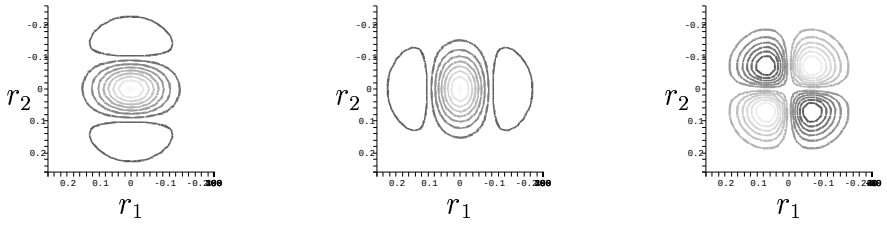


(a) $R_{11}$ (b) $R_{22}$ (c) $R_{12}$

Figure 5.28: Case 1. Isotropic. Iso-contours. Light contours: high levels, dark contours: low (or negative) levels. Levels: a) and b) [-10:50:540]; c) [-60:10:-10 and 10:10:60]

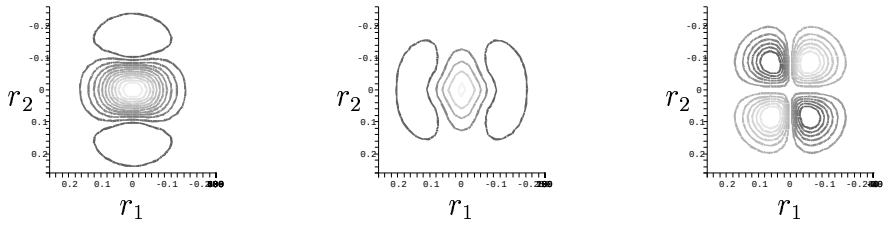


(a) $R_{11}$ (b) $R_{22}$ (c) $R_{12}$

Figure 5.29: Case 2. Anisotropic. Principal axes 0 degrees. Isotropic length scale. Same scaling as case 1.

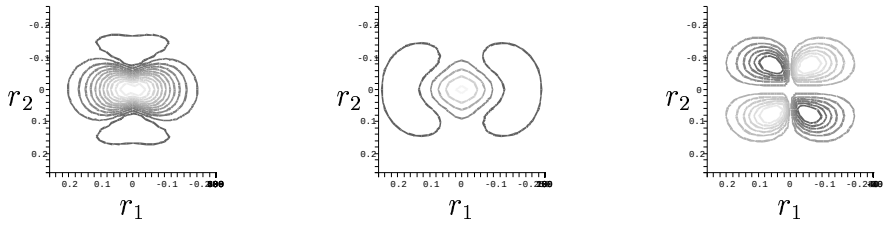


(a) $R_{11}$ (b) $R_{22}$ (c) $R_{12}$

Figure 5.30: Case 3. Anisotropic. Principal axes 0 degrees. Anisotropic length scale. Same scaling as case 1.

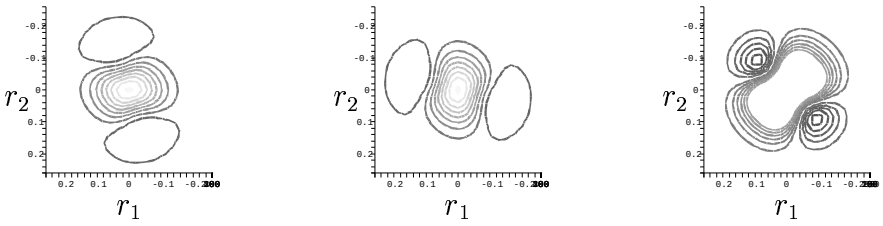


(a) $R_{11}$ (b) $R_{22}$ (c) $R_{12}$

Figure 5.31: Case 4. Anisotropic. Principal axes 45 degrees. Isotropic length scale. Same scaling as case 1.

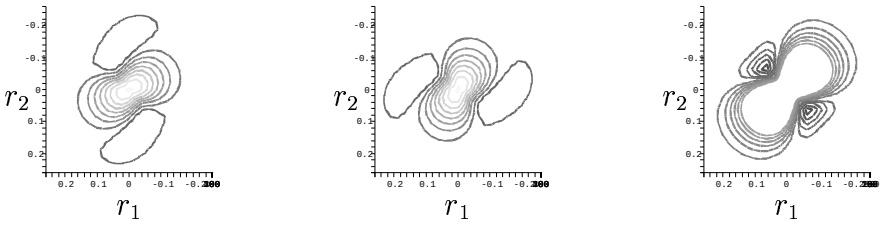


(a) $R_{11}$ (b) $R_{22}$ (c) $R_{12}$

Figure 5.32: Case 5. Anisotropic. Principal axes 45 degrees. Anisotropic length scale. Same scaling as case 1.

# Chapter 6

# Concluding Remarks

The main goal of the project was to investigate the possibility to develop a noise prediction method for turbulent jets which is considerably less computationally costly than LES and DNS and more flexible and general than existing statistical methods. The work in the project has been related to two approaches for jet noise predictions. The main work has been devoted to improving the prediction capability of the SNGR method and a minor part has been on anisotropic modeling of turbulence related to statistical noise prediction theory. A general ready-to-use SNGR method capable to predict the far-field noise in terms of sound pressure level directivity and spectral energy content has not been accomplished, but the proposed method has the capability to predict trends in the flow Mach numbers and can be used to evaluate different flow configurations.

The more technical conclusions based on the results from the papers in the present thesis are as follows.

- **Inhomogeneous** linearized Euler equations (ILEE) on conservative form have been derived. The possibility to use the ILEE as a wave operator with source terms has been tested and the results show that the approach accurately predicts sound generation from turbulence as well as propagation of the generated sound. The accuracy of the noise prediction is shown to be determined by the correctness of the source term modeling where the space-time structure of the source field is the most important factor.

- **A method** to stochastically generate anisotropic synthesized turbulence has been proposed in the present work and is shown to be able to generate turbulence with an arbitrary specified Reynolds

stress field. The anisotropic method includes length scale anisotropy which is determined by the relative magnitude of the normal Reynolds stress tensor components. The largest and smallest length scales are thus found in the directions of the principal axes of the model Reynolds stress tensor. The proposed method to generate synthesized turbulence requires three scaling factors. These are the length scale, time scale and amplitude factors denoted by $f_L$, $f_\tau$ and $f_A$ respectively and are used to calibrate the level and spectral content in the generated sound from the synthesized turbulence.

- **From generic** test cases it is shown that the frequencies in the generated sound from the proposed SNGR method is strongly related to the length scales in the synthesized turbulence. The time scale in the generated turbulence affects the compactness of the turbulence and thus the level of the generated turbulence. The directivity of the generated sound from the anisotropic synthesized turbulence is determined by the relative magnitude of the normal Reynolds stress components. The highest level of the generated sound is found in the direction of the largest normal component of the Reynolds stress tensor and are thus found in one of the principal axes. The direction of the lowest generated sound is likewise found in the direction of the smallest normal Reynolds stress tensor component.

- **The jet noise** predictions using the proposed SNGR method are with properly calibrated model parameters within $3$ dB in sound pressure level directivity compared to measurements of the same flows. The method accurately predicts the increased noise generation from a Mach $0.75$ jet to a Mach $0.90$ jet using the same model parameters indicating that the method has the capability to be used for evaluation of changes in flow Mach numbers. This agreement was however not found when the Mach $0.75$ jet was heated. The reasons for this are believed to be related to an increased instability of the heated jet and that the source field in the stochastic method does not include high temperature effects.

  The spectral content in the far-field sound is not in satisfactory agreement with measurements. The emitted noise from the jet simulations has an under-prediction of the sound at low frequencies, even if the inclusion of anisotropy in the source field modeling slightly improved the spectral results.

- **The anisotropy** in the Reynolds stress tensor predicted from the Boussinesq assumption based the standard $k-\varepsilon$ RANS turbulence model for the Mach $0.75$ jet is in relatively good agreement with LES solution of the same flow and can be used as input to the proposed anisotropic SNGR method.

- **The noise** generation from the proposed SNGR method is too strong unless the amplitude factor $f_A$ is used to lower the kinetic energy of the synthesized turbulence. The reason for this is related to the time filter for the synthesized turbulence which needs to be improved for the method to be a general noise prediction method without calibration of the amplitude of the emitted sound.

- **An anisotropic** model for the two-point velocity correlation tensor for homogeneous turbulence has been proposed. The functional form of the correlation tensor is determined by six one-dimensional scalar correlation functions. A preliminary model for the scalar correlation functions is also presented but further development is required before a complete model can be presented. In the framework of statistical noise prediction methods, the proposed model may enable accurate modeling of the noise generated by anisotropic turbulence.

# Bibliography


[1] M.J. Lighthill. On sound generated aerodynamically, i. general theory. *Proc. Roy. Soc.*, A 211:564–587, 1952.

[2] M.J. Lighthill. On sound generated aerodynamically, ii. turbulence as a source of sound. *Proc. Roy. Soc.*, A 222:1–32, 1954.

[3] H.S. Ribner. Quadrupole correlations governing the pattern of jet noise. *Journal of Fluid Mechanics*, 38:1 – 24, 1969.

[4] J. Curle. The influence of solid boundaries upon aerodynamic sound. *Proc. Roy. Soc.*, A 231:505–514, 1955.

[5] J.E. Ffowcs Williams and D.L. Hawkins. Sound generation by turbulence and surfaces in arbitrary motion. *Philos. Trans. Roy. Soc.*, A 264, No. 1151:321–342, 1969.

[6] O.M. Philips. On the aerodynamic surface sould from a plane turbulent boundary layer. *Proc. Roy. Soc.*, A 234, no 1198:327–335, 1956.

[7] R.H. Kraichnan. Noise transmission from boundary layer pressure fluctuations. *J. Acoust. Soc. Am.*, 29:65–80, 1957.

[8] P.E. Doak. Acoustic radiation from a turbulent fluid containing foreign bodies. *Proc. Roy. Soc.*, A 254, no 1276:129–145, 1960.

[9] F. Pérot, J.-A. Auger, H. Giardi, X. Gloerfelt, C. Bailly. Numerical prediction of the noise radiated by a cylinder. Hilton Head, South Carolina, 2003. The 9th AIAA/CEAS Aeroacoustics Conference, AIAA 2003-3240.

[10] J.E. Ffowcs Williams. The noise from turbulence convected at high speed. *Philos. Trans. Roy. Soc.*, A 255 No. 1061:496–503, 1963.

[11] M. Goldstein and B Rosenbaum. Effect of anisotropic turbulence on aerodynamic noise. *J. Acoust. Soc. Am.*, 54 (3):630–645, 1973.

[12] A. Khavaran. Role of anisotropy in turbulent mixing noise. *AIAA Journal*, 37 , No. 7:832–841, 1999.

[13] W. Bechara, P Lafon, C. Bailly, and S. M. Candel. Application of a k-epsilon turbulence model to the prediction of noise for simple and coaxial free jets. *J. Acoust. Soc. Am.*, 97(6):3518–3531, 1995.

[14] C. Bailly, P. Lafon, and S. M. Candel. Subsonic and supersonic jet noise predictions from statistical source models. *AIAA Journal*, 35 , No. 11:1688–1696, 1997.

[15] P. Jordan and Y. Gervais. Modelling self and shear noise mechanisms in anisotropic turbulence. Hilton Head, South Carolina, 2003. The 9th AIAA/CEAS Aeroacoustic Conference, AIAA 2003-8743.

[16] W.J. Devenport, C. Muthanna, R. Ma, S. Glegg. Two-point descriptions of wake turbulence with application to noise prediction. *AIAA Journal*, 39 , No. 12:2302–2307, 2001.

[17] G.M. Lilley. On the noise from jets. *AGARD CP-131*, 1974.

[18] S.C. Crow and F.H. Champagne. Sound generation in a mixing layer. *Journal of Fluid Mechanics*, 48:547 – 591, 1971.

[19] C.K.W. Tam. Supersonic jet noise. *Annu. Rew. Fluid Mech.*, 27:17–43, 1995.

[20] H.H. Hubbard. *Aeroacoustics of Flight Vehicles, Volume 1: Noise Sources*. Acoustical Society of America, Woodbury, NY, 1995.

[21] W. Bechara, C. Bailly, P. Lafon, and S. M. Candel. Stochastic approach to noise modeling for free turbulent flows. *AIAA Journal*, 32 , No. 3:455–463, 1994.

[22] C. Bailly, P. Lafon, and S. M. Candel. A stochastic approach to compute noise generation and radiation of free turbulent flows. AIAA Paper 95-092, 1995.

[23] C. Bailly and D. Juvé. A stochastic approach to compute subsonic noise using linearized euler's equations. AIAA Paper 99-1872, 1999.

[24] M. Billson, L.-E. Eriksson, and L. Davidson. Jet noise prediction using stochastic turbulence modeling. Hilton Head, South Carolina, 2003. The 9th AIAA/CEAS Aeroacoustics Conference, AIAA 2003-3282, Revised and submitted for journal publication.

[25] M. Billson, L.-E. Eriksson, and L. Davidson. Modeling of synthetic anisotropic turbulence and its sound emission. Manchester, United Kindom, 2004. The 10th AIAA/CEAS Aeroacoustics Conference, AIAA 2004-2857.

[26] M. Billson, L.-E. Eriksson, and L. Davidson. Jet noise modeling using synthetic anisotropic turbulence. Manchester, United Kindom, 2004. The 10th AIAA/CEAS Aeroacoustics Conference, AIAA 2004-3028.

[27] L.-E. Eriksson. Deliverable 1.9, updated cfd models. Eu research programme - fp5, Volvo Aero Corporation, Trollhattan, Sweden, 2003.

[28] R.H. Kraichnan. Diffusion by a random velocity field. *J. Comp. Physics*, 13(1):22–31, 1970.

[29] M. Karweit, P. Blanc-Benon, D. Juvé, and G. Comte-Bellot. Simulation of the propagation of an acoustic wave through a turbulent velocity field: A study of phase variance. *J. Acoust. Soc. Am.*, 89(1):52–62, 1991.

[30] H. Tennekes and J. L. Lumley. *A First Cource In Turbulence*. MIT Press, 1994.

[31] P. Batten, U. Goldberg, and S. Chakravarthy. Reconstructed subgrid methods for acoustics predictions at all reynolds numbers. Breckenridge, Colorado, 2002. The 8th AIAA/CEAS Aeroacoustics Conference, AIAA 2002-2511.

[32] M. Billson, L.-E. Eriksson, and L. Davidson. Acoustic source terms for the linear euler equations on conservative form. Breckenridge, Colorado, 2002. The 8th AIAA/CEAS Aeroacoustics Conference, AIAA 2002-2582, Revised and submitted for journal publication.

[33] P. Huerre and P. A. Monkewitz. Local and global instabilities in spatially developing flows. *Annu. Rev. Fluid Mech.*, 22:473–537, 1990.

[34] C. Bogey, C. Bailly, and D. Juvé. Computation of flow noise using source terms in linearized euler's equations. *AIAA Journal*, 40 No. 2, 2002.

[35] X. Zhang, X. Cheng, and C. L. Morfey. Computation of fan noise radiation through a realistic engine exhaust geometry with flow. Hilton Head, South Carolina, 2003. The 9th AIAA/CEAS Aeroacoustics Conference, AIAA 2003-3267.

[36] R. Ewert and W. Schröder. Acoustic perturbation equations based on flow decomposition via source filtering. *J. Comp. Physics*, 188:365–398, 2003.

[37] R. Ewert, M. Meinke, and W. Schröder. Comparison of source term formulations for a hybrid cfd/caa method. Maastricht, The Netherlands, 2001. The 7th AIAA/CEAS Aeroacoustics Conference, AIAA 2001-2200.

[38] L.-E. Eriksson. Development and validation of highly modular flow solver versions in g2dflow and g3dflow. Internal report 9970-1162, Volvo Aero Corporation, Sweden, 1995.

[39] L.-E. Eriksson. Lecture notes, compressible cfd. Division of Thermo and Fluid Dynamics, Department of Mechanical Engineering, Chalmers University of Technology, Sweden, 2003.

[40] A. S. Lyrintzis. Review: The use of kirchhoff's method in computational aeroacoustics. *ASME: Journal of Fluids Engineering*, 116:665 – 676, 1994.

[41] C.K.W. Tam and J.C. Webb. Dispersion-relation-preserving finite difference schemes for computational acoustics. *J. Comp. Physics*, 107:262–281, 1993.

[42] L.-E. Eriksson. *Transfinite Mesh Generation and Computer-Aided Analysis of Mesh Effects*. PhD thesis, Department of Computer Sciences, Uppsala University, Sweden, 1984.

[43] J. B. Freund, S. K. Lele, and P. Moin. Calculation of the radiated sound field using an open kirchhoff surface. *AIAA Journal*, 34 No. 5:909 – 916, 1996.

[44] A.D. Pierce. *Acoustics. An Introduction to Its Physical Principles and Applications*. Acoustical Society of America, Woodbury, New York, 1991.

[45] M. Billson. Jet noise prediction based on large eddy simulation. Thesis for the degree Master of Science, 1999.

[46] K.W. Thompson. Time dependent boundary conditions for hyperbolic systems, $i$. *J. Comp. Physics*, 68:1–24, 1987.

[47] K.W. Thompson. Time dependent boundary conditions for hyperbolic systems, $ii$. *J. Comp. Physics*, 89:439–461, 1990.

[48] T. Colonius, S.K. Lele, and P. Moin. Boundary conditions for direct computation of aerodynamic sound generation. *AIAA Journal*, 31 No. 9:1574 – 1582, 1993.

[49] M. Billson and P. Jordan. Anisotropic formulation of the velocity correlation tensor. Internal report 04/02, Div. of Thermo and Fluid Dynamics , Dept. of Mechanical Engineering , Chalmers University of Technology, 2004.

[50] C. Bogey and C. Bailly. Three-dimensional non-reflective boundary conditions for acoustic simulations: far field formulation and validation test cases. *ACOUSTICA acta acoustica*, 88 (4):463 – 471, 2002.

[51] C.K.W. Tam and Z. Dong. Radiation and outflow boundary conditions for direct computation of acoustic and flow disturbances in a nonuniform mean flow. *J. Comput. Acoust*, 4:175–201, 1996.

[52] T. Colonius, S.K. Lele, and P. Moin. Sound generation in a mixing layer. *Journal of Fluid Mechanics*, 330:375 – 409, 1997.

[53] C. Bogey, C. Bailly, and D. Juvé. Numerical simulation of sound generated by vortex pairing in a mixing layer. *AIAA Journal*, 38 No. 12, 2000.

[54] A. Michalke. On the inviscid instability of the hyperbolic-tangent velocity profile. *Journal of Fluid Mechanics*, vol 19, 1964.

[55] M. Billson. Computational techniques for jet noise predictions. *Lic. Thesis, Department of Thermo and Fluid Dynamics, Chalmers University of Technology, Gothenburg*, 2002.

[56] A. S. Monin and A. M. Yaglom. *Statistical Fluid Mechanics*. MIT Press, 1971.

[57] G.K. Batchelor. *The theory of homogeneous turbulence*. Cambridge University Press, 1953.

[58] N. Andersson, L.-E. Eriksson, and L. Davidson. Large–eddy simulation of a mach 0.75 jet. Hilton Head, South Carolina, 2003. The 9th AIAA/CEAS Aeroacoustics Conference, AIAA 2003-3312.

[59] D. Crighton. Basic principles of aerodynamic noise generation. *Progress in Aerospace Sciences*, 16 No. 1:31–96, 1975.

[60] M. Billson, L.-E. Eriksson, and L. Davidson. Stochastic noise source modeling for turbulent jets. Chamonix, France, December, 2003. Computational Aeroacoustics : From Acoustic Sources Modeling to Far-Field Radiated Noise Prediction, Colloquium EUROMECH 449.

[61] S. Chandrasekhar. The theory of axisymmetric turbulence. *Philos. Trans. Roy. Soc.*, Vol 242. A 855:557–577, 1950.

# Chapter 7

# Appendix

## 7.1 The Linearized Euler Equations

This section presents the linearization of the Euler equations on conservative form. The Euler equations can be written in a compact conservative form as

$$\frac{\partial Q}{\partial t} + \frac{\partial E}{\partial x} + \frac{\partial F}{\partial y} + \frac{\partial G}{\partial z} = 0 \tag{7.1}$$

where

$$Q = \begin{pmatrix} \rho \\ \rho u \\ \rho v \\ \rho w \\ \rho e_0 \end{pmatrix}$$

$$E = \begin{pmatrix} \rho u \\ \rho uu + p \\ \rho uv \\ \rho uw \\ \rho h_0 u \end{pmatrix} \quad F = \begin{pmatrix} \rho v \\ \rho uv \\ \rho vv + p \\ \rho vw \\ \rho h_0 v \end{pmatrix} \quad G = \begin{pmatrix} \rho w \\ \rho uw \\ \rho vw \\ \rho ww + p \\ \rho h_0 w \end{pmatrix} \tag{7.2}$$

The solution vector can be decomposed into a reference solution and a disturbance.

$$Q = Q_0 + Q' \tag{7.3}$$

The reference solution is assumed to be an average of the solution variables, i.e. ensemble average of time-average which satisfies equation 7.1. A linearization of the equations around the reference solution

is given by

$$\begin{aligned} E(Q) &= E(Q)_0 + \left(\frac{\partial E}{\partial Q}\right)_0 Q' + \text{HOT} \\ F(Q) &= F(Q)_0 + \left(\frac{\partial F}{\partial Q}\right)_0 Q' + \text{HOT} \\ G(Q) &= G(Q)_0 + \left(\frac{\partial G}{\partial Q}\right)_0 Q' + \text{HOT} \end{aligned} \tag{7.4}$$

where subscript $(\cdot)_0$ indicates evaluation at reference solution. Using the relations above in equation 7.1 gives

$$\begin{aligned} &\frac{\partial Q_0 + Q'}{\partial t} + \\ &\frac{\partial}{\partial x}\left(E(Q)_0 + \left(\frac{\partial E}{\partial Q}\right)_0 Q'\right) + \\ &\frac{\partial}{\partial y}\left(F(Q)_0 + \left(\frac{\partial F}{\partial Q}\right)_0 Q'\right) + \\ &\frac{\partial}{\partial z}\left(G(Q)_0 + \left(\frac{\partial G}{\partial Q}\right)_0 Q'\right) = \text{HOT} \end{aligned} \tag{7.5}$$

The reference solution satisfies the Euler equations (equation 7.1). Thus, subtracting the reference solution and neglecting the higher order terms gives

$$\frac{\partial Q'}{\partial t} + \frac{\partial}{\partial x}\left(A_0 Q'\right) + \frac{\partial}{\partial y}\left(B_0 Q'\right) + \frac{\partial}{\partial z}\left(C_0 Q'\right) = 0 \tag{7.6}$$

where $A_0 = (\partial E/\partial Q)_0$, $B_0 = (\partial F/\partial Q)_0$, $C_0 = (\partial G/\partial Q)_0$. Equations 7.6 are the Linearized Euler Equations (LEE) on compact conservative form. In tensor notation the equations are

$$\begin{aligned} \frac{\partial \rho'}{\partial t} + \frac{\partial (\rho u_j)'}{\partial x_j} &= 0 \\ \frac{\partial (\rho u_i)'}{\partial t} + \frac{\partial}{\partial x_j}(\widetilde{u}_j(\rho u_i)' + \widetilde{u}_i(\rho u_j)' - \rho'\widetilde{u}_i\widetilde{u}_j + p'\delta_{ij}) &= 0 \\ \frac{\partial (\rho e_0)'}{\partial t} + \frac{\partial}{\partial x_j}(\widetilde{h}_0(\rho u_j)' + \widetilde{u}_j(\rho h_0)' - \rho'\widetilde{h}_0\widetilde{u}_j) &= 0 \end{aligned} \tag{7.7}$$

The $(\cdot)'$ is a fluctuation associated with an ordinary time-average $\overline{(\cdot)}$ and $(\cdot)''$ is is a fluctuation associated with a Favre time-average $\widetilde{(\cdot)} = \overline{\rho(\cdot)}/\overline{\rho}$.

The use of pressure and enthalpy in equation 7.7 is consistent with the decomposition of the conservative solution variables in $Q$ and are introduced to enable a shorter notation. These auxiliary variables are expressed in the solution variables as

$$\begin{aligned} p &= (\gamma - 1)\left(\rho e_0 - \frac{1}{2}\frac{(\rho u_k)(\rho u_k)}{\rho}\right) \\ \rho h_0 &= \rho e_0 + p \end{aligned} \tag{7.8}$$

The linearized Euler equations can also be written in primitive form with solution vector $q' = [\rho', u'', v'', w'', p']$. The transformation of equations 7.6 to primitive form starts with the Taylor expansion

$$Q = Q(q_0 + q') = Q_0 + \left(\frac{\partial Q}{\partial q}\right)_0 q' + \mathrm{HOT} \tag{7.9}$$

which in linear theory is the same as

$$Q' = Q - Q_0 = \left(\frac{\partial Q}{\partial q}\right)_0 q' \tag{7.10}$$

Using the definitions

$$M_0 = \left(\frac{\partial Q}{\partial q}\right)_0 \quad \text{and} \quad M_0^{-1} = \left(\frac{\partial q}{\partial Q}\right)_0 \tag{7.11}$$

we can rewrite equations 7.6 as

$$\frac{\partial q'}{\partial t} + M_0^{-1}\frac{\partial}{\partial x}\left(A_0 M_0 q'\right) + M_0^{-1}\frac{\partial}{\partial y}\left(B_0 M_0 q'\right) + M_0^{-1}\frac{\partial}{\partial z}\left(C_0 M_0 q'\right) = 0 \tag{7.12}$$

Equations 7.12 are the linearized Euler equations on compact primitive form. The resulting equations are quite large in tensor notation and are therefore not presented.

## 7.2 Stability Analysis of Hyperbolic Equations

In this section Fourier analysis is used for a semi-discrete stability analysis of a one-dimensional convection equation. Relations for the dispersion relation and the dissipation relation for an even-order space

discretization are derived. Artificial dissipation through upwinding is also taken into account in the analysis. Also a fully-discrete stability analysis is performed for a four-stage Runge-Kutta time discretization. Last, the correct way to introduce source terms in a 4:th order Runge-Kutta time marching technique is presented.

### 7.2.1 Semi-Discretization

Start with the model equation (one-dimensional convection equation with constant coefficient, $c$).

$$\frac{\partial u}{\partial t} + c\frac{\partial u}{\partial x} = 0 \tag{7.13}$$

Assuming that the spatial solution to equation 7.13 is known, the exact solution to this equation can be written as

$$u(x,t) = u_0 \exp(st) \exp(-ikx) \tag{7.14}$$

where $u_0$ is a constant amplitude and $k$ is the wave number. The solution is decomposed into a time-dependent part and a space-dependent part as shown in equation 7.14. Since the spatial dependence is known, $\exp(-ikx)$, the time-dependence is to be determined, i.e. $s$ in the time dependent part of the solution. Inserting the equation 7.14 into equation 7.13 results in

$$su_0 \exp(st) \exp(-ikx) - ikcu_0 \exp(st) \exp(-ikx) = 0 \tag{7.15}$$

which in turn gives a relation for $s$ as

$$s = ikc \qquad \text{or} \qquad s = i\omega \qquad \text{where} \qquad \omega \equiv kc \tag{7.16}$$

where $\omega$ is the angular velocity by which the solution varies in a given point in space.

Reinserting this into the time dependent part of the solution, equation 7.14 gives that

$$z \equiv \exp(st) = \exp(ikct) \tag{7.17}$$

which has a purely imaginary exponent. The result is that the exact solution to equation 7.13 will have a periodic behaviour in time without damping or amplification. Furthermore, $\omega$ is in direct proportion to the wave number $k$, because the phase velocity, i.e. the velocity of propagation defined by $c = \omega/k$, is the same for all wave numbers.

Now, an expression for $s$ will be derived in the case of a semi-discretization of the one-dimensional convection equation 7.13. The equation is discretized in space using a finite difference approximation. Discretized, equation 7.13 becomes.

$$\frac{\partial u_j}{\partial t} + c\frac{\partial u_j}{\partial x_j} = 0 \tag{7.18}$$

where $j$ is the number of the cell over which the equation is to be analyzed, see figure 7.1. Now we introduce a finite difference approximation of the space derivative on a equidistant mesh.

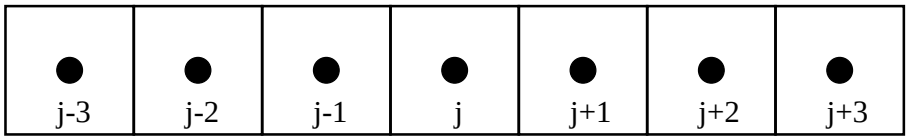


Figure 7.1:

$$\frac{\partial u_j}{\partial x_j} = \frac{1}{\Delta x}\sum_{l=-N}^{M} a_l u_{j+l} \tag{7.19}$$

and limit this analysis to $N = M$ and let $a_l = -a_{-l}$ with $a_0 = 0$. We can then construct a central difference scheme, i.e. an even-order approximation of the spatial derivative. Equation 7.18 then becomes

$$\frac{\partial u_j}{\partial t} + \frac{c}{\Delta x}\sum_{l=-M}^{M} a_l u_{j+l} = 0 \tag{7.20}$$

We can write the solution to equation 7.18 on the form

$$u_j = u_0 \exp(st)\exp(-ik\Delta x j) \tag{7.21}$$

Insert this into equation 7.20 above. The space-dependent part has been modified according to the space discretization. Observe that the time dependent part of the solution is still continuous, i.e. not discretized. This gives

$$su_0 \exp(st)\exp(-ik\Delta x j) + u_0 \exp(st)\frac{c}{\Delta x}\sum_{l=-M}^{M} a_l \exp(-ik\Delta x(j+l)) = 0 \tag{7.22}$$

which can be rewritten as

$$s = -\frac{c}{\Delta x} \sum_{l=-N}^{M} a_l \exp(-ik\Delta xl) \tag{7.23}$$

Using the fact that $a_l = -a_{-l}$ allows us to rewrite the above expression for $s$ to

$$s = -\frac{c}{\Delta x} \sum_{l=1}^{M} a_l (\exp(-ik\Delta xl) - \exp(ik\Delta xl)) \tag{7.24}$$

With the identity

$$\sin(\Theta) = \frac{\exp(i\Theta) - \exp(-i\Theta)}{2i} \tag{7.25}$$

we get

$$s = \frac{2ic}{\Delta x} \sum_{l=1}^{M} a_l \sin(k\Delta xl) \tag{7.26}$$

The approximation of $z = \exp(st)$ (equation 7.17) in the semi-discretized case is then

$$z(k,t) = \exp\left(\frac{2ict}{\Delta x} \sum_{l=1}^{M} a_l \sin(k\Delta xl)\right) \tag{7.27}$$

In this case with an even-order discretization, the expression in the exponent of equation 7.27 is also purely imaginary giving a numerical scheme with zero numerical dissipation. Semi-discretized $\omega$ is however not directly proportional to $k$ any more (cf. equation 7.16). The relation between $\omega$ and $k$ is called the phase velocity or dispersion relation and is defined by

$$c^* = \frac{\mathrm{Im}(s)}{k} = \frac{\omega}{k} \tag{7.28}$$

where $\omega$ and $c^*$ are dependent on $k$. The discretization of the spatial derivative in equation 7.13 results in an incorrect dispersion relation, and the phase velocity will be dependent on the wave number. Higher-order schemes generally result in more accurate dispersion relation for a larger range of wave numbers than lower-order methods.

As an example, the resulting dispersion relation for a 4:th order space discretization is plotted in figure 7.2. The figure shows the phase

velocity as a function of wave number. The wave number is scaled with $\frac{1}{\Delta x}$ to give the quantity $\theta = k\Delta x$. The phase velocity is scaled with $\frac{c}{k\Delta x}$. This gives a periodic function $\frac{\Delta x}{c}\mathrm{Im}(s)$ with period $\pi$. This can be seen by using the definition of wave number $k = \frac{2\pi}{\lambda}$ where $\lambda$ is a wavelength. By writing the wavelength as a factor $\xi$ times $\Delta x$, $\lambda = \xi\Delta x$, we can write

$$\xi = \frac{2\pi}{\theta} \qquad \text{where} \qquad 0 \leq \theta \leq \pi \tag{7.29}$$

The $\xi$ represents the number of grid points per wavelength that correspond to a certain $k\Delta x$. For example, a value of $k\Delta x = \theta = \pi$ corresponds to a spatial resolution of 2 points per wavelength, $k\Delta x = \theta = \pi/2$ corresponds to a spatial resolution of 4 points per wavelength and so on. The exact solution is linear in $k$ (see equation 7.16) and is shown as the dashed line in figure 7.2. The phase velocity of the 4:th order semi-discretization is shown as the solid line in figure 7.2. For low values of $k\Delta x$ corresponding to a high resolution (many points per wavelength) the approximation follows the analytical solution but at $k\Delta x \approx \pi/4$ the phase velocity of the semi-discretized solution starts to deviate from the analytical. To achieve a good numerical solution in this case the required resolution according to this semi-discrete analysis should be at least 8 points per wavelength ($k\Delta x \leq \pi/4$).

### 7.2.2 Artificial Numerical Dissipation

High even-order central numerical approximations to first-order derivatives have no inherent numerical dissipation. This is the reason why they are used in numerical solvers instead of odd-order approximations. But to ensure that numerical stability is retained, some kind of numerical dissipation has to be added to the solution. This is done by adding an even-order derivative times a small coefficient $\varepsilon$ to the model equation (equation7.13). The model equation becomes

$$\frac{\partial u}{\partial t} + c\frac{\partial u}{\partial x} = (-1)^{n+1}\varepsilon\frac{\partial^{2n} u}{\partial x^{2n}} \tag{7.30}$$

where the sign of the term is given by $(-1)^{n+1}$. To be dissipative, a second-order derivative, $n = 1$, is added with a positive sign or a fourth-order derivative $n = 2$ is added with a negative sign, and so on. The semi-discretized model equation is then written as

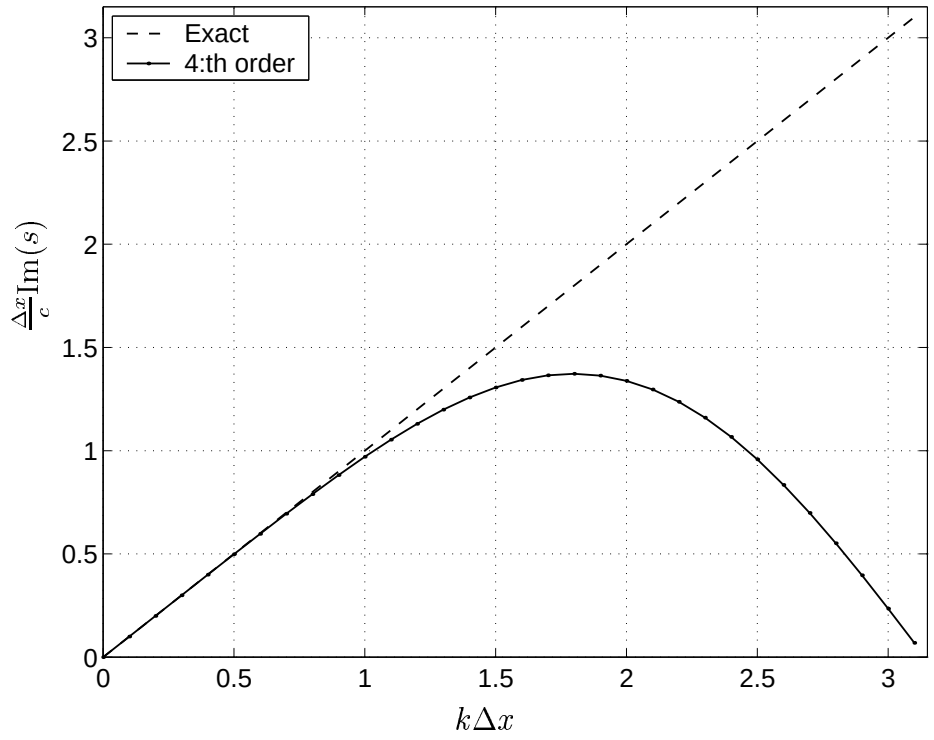


Figure 7.2: Dispersion relation for semi-discretization, 4:th order scheme

$$\frac{\partial u_j}{\partial t} + \frac{c}{\Delta x}\left(\sum_{l=-N}^{M} a_l u_{j+l} + \varepsilon \sum_{l=-N}^{M} d_l u_{j+l}\right) = 0 \tag{7.31}$$

The coefficients $d_l$ in equation 7.31 determine the order of the approximated term. The coefficients for a central difference approximation of a sixth-order derivative are given in Section 7.5. The amount of dissipation added is controlled by the factor $\varepsilon$. The expression for $s$ in this case becomes

$$s = \frac{c}{\Delta x}\left[2i\sum_{l=1}^{M} a_l \sin(k\Delta x l) - \varepsilon\left(d_0 + 2\sum_{l=1}^{M} d_l \cos(k\Delta x l)\right)\right] \tag{7.32}$$

and

$$z(k,t) = \exp(st) = \exp\left(\frac{ct}{\Delta x}\left[2i\sum_{l=1}^{M} a_l \sin(k\Delta x l) - \varepsilon\left(d_0 + 2\sum_{l=1}^{M} d_l \cos(k\Delta x l)\right)\right]\right) \quad (7.33)$$

When adding a dissipative term in this way, the exponent in the expression for $z$ is no longer purely imaginary but also includes a real part. The effect of this can be seen if we rewrite equation 7.33 as

$$z(k,t) = \exp\left[\frac{2ict}{\Delta x}\sum_{l=1}^{M} a_l \sin(k\Delta x l)\right] \exp\left[-\frac{c\varepsilon t}{\Delta x}\left(d_0 + 2\sum_{l=1}^{M} d_l \cos(k\Delta x l)\right)\right] \quad (7.34)$$

If the exponent in the real part of equation 7.34 is positive for a certain $k$ then the corresponding wave will be amplified in time and if the exponent is negative for a certain $k$ the corresponding wave will decrease in time. Observe that including dissipation with this technique does not affect the dispersion, only the dissipation. As an example the dispersion relation and dissipation relation of the standard 4:th order scheme and the "Dispersion Relation Preserving" scheme (DRP) by Tam[41] are shown in figure 7.3. A 4:th order derivative is used to add dissipation to the 4:th order scheme and a 6:th order derivative for the DRP. Figure 7.3(a) shows a clear difference between the standard 4:th order scheme and the DRP. The DRP scheme shows a negligible error in the dispersion relation up to $k\Delta x \approx \pi/2$ while the standard scheme gives the same amount of error at $k\Delta x \approx \pi/4$. Figure 7.3(b) shows the real part of $s$ as a function of $k\Delta x$. Negative values of $\mathrm{Re}(s)$ for a certain $k\Delta x$ correspond to dissipation of waves with wave number $k$. The ideal form of the curves in figure 7.3(b) would be a zero value for all wave number $k\Delta x$ up to $k\Delta x \approx \pi$ and then a very large negative value of $\mathrm{Re}(s)$ at $k\Delta x \approx \pi$. With this in mind one can see that the sixth-order derivative added in the DRP scheme gives slightly better distribution of the dissipation over different wave number $k$ than the fourth-order derivative added in the 4:th order scheme.

### 7.2.3 Full Discretization

When stability analysis is based on the semi-discretized equations the time variable is assumed to be continuous and the time derivative is

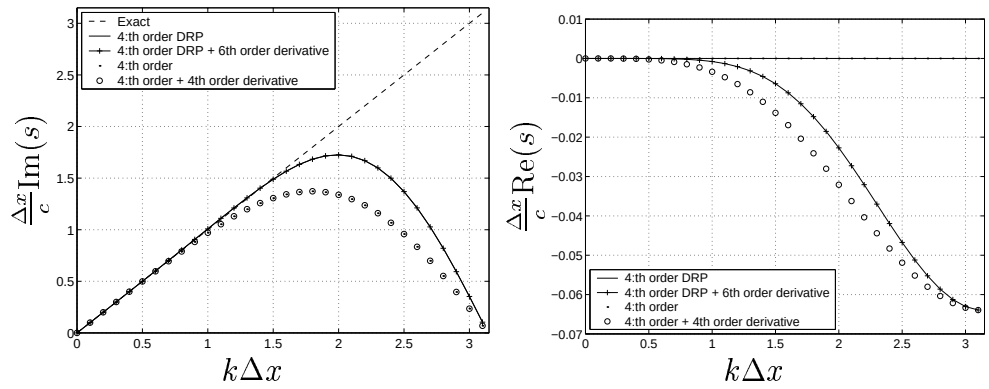


(a) Dispersion relation

(b) Dissipation relation

Figure 7.3: Dispersion relation and dissipation relation for semi-discretization

assumed to be evaluated exactly. In a numerical solver, however, the time marching is not exact. When using a Runge-Kutta time marching technique the time dependent part of equation 7.21 is approximated by a Taylor expansion of $z = \exp(st)$. To see this, begin by rewriting the model equation, equation 7.18 on the form

$$\frac{\partial u_j}{\partial t} = Au_j \tag{7.35}$$

where $Au_j$ is an approximation of the spatial derivative $-c\frac{\partial u}{\partial x}$ at location $j$. For a linear operator $A$, a four-stage 4:th order Runge-Kutta applied on the model equation can be written as

$$\begin{aligned} u_j^* &= u_j^n + \frac{1}{4}\Delta t A u_j^n \\ u_j^{**} &= u_j^n + \frac{1}{3}\Delta t A u_j^* \\ u_j^{***} &= u_j^n + \frac{1}{2}\Delta t A u_j^{**} \\ u_j^{n+1} &= u_j^n + \Delta t A u_j^{***} \end{aligned} \tag{7.36}$$

where $u_j^n$ is the solution at time step $n$ and $u_j^{n+1}$ is the solution at time step $n+1$ and $j$ is the the current space location. This gives a 4:th order time stepping in terms of the Taylor expansion

$$u_j^{n+1} = [1 + At + \frac{1}{2}A^2t^2 + \frac{1}{6}A^3t^3 + \frac{1}{24}A^4t^4]u_j^n + \mathrm{HOT} \tag{7.37}$$

or equivalently

$$z = \exp(st) \approx 1 + st + \frac{1}{2}s^2t^2 + \frac{1}{6}s^3t^3 + \frac{1}{24}s^4t^4 + \text{HOT} \tag{7.38}$$

By inserting the resulting expression for $s$ from the semi-discrete analysis into equation 7.38 an expression is given for how the solution develops in time when the time marching is done through a 4:th order time marching technique. Two quantities will now be defined. The amplitude error and the relative phase velocity. The amplitude error of the approximation of $z$ is defined by

$$\varepsilon_A = \frac{|z| - 1}{\Delta t} \tag{7.39}$$

and the relative phase velocity is defined by

$$\frac{c*}{c} = \frac{-\angle z}{kc\Delta t} \tag{7.40}$$

where $\angle z$ is the phase of $z$ and $|z|$ is the amplitude. Although not obvious here, $c^*$ is now not only a function of $k\Delta x$, but also of the CFL number and hence has a dependence on $\Delta t$. This was not the case in the semi-discrete analysis and this is the main difference between the semi-discrete and the fully discrete analysis. The amplitude error and relative phase velocity for a 4:th order space discretization and the 4:th order DRP scheme combined with a 4:th order Runge-Kutta time marching with $\text{CFL} = 0.5$ are shown in figure 7.4. The amount of dissipation added is the same as in the semi-discrete case above.

The dependence of the amplitude error and the relative phase velocity on CFL-number is shown in figure 7.5. As can be seen in figures 7.5(a) and 7.5(b) the difference is small for all CFL-numbers in terms of relative phase velocity and also for CFL-number up to $0.5$ in terms of amplitude error. For $\text{CFL} = 0.6$ there is a clear increase in amplitude error. Based on this the conclusion is that the solution is more or less independent of CFL-number up to approximately $\text{CFL} = 0.5$ with an increase of numerical dissipation for higher values of the CFL-number.

### 7.2.4 Introducing Source Terms

Introducing source terms into the fully discretized equation 7.35 gives an equation as

$$\frac{\partial u_j}{\partial t} = Au_j + \sigma \tag{7.41}$$

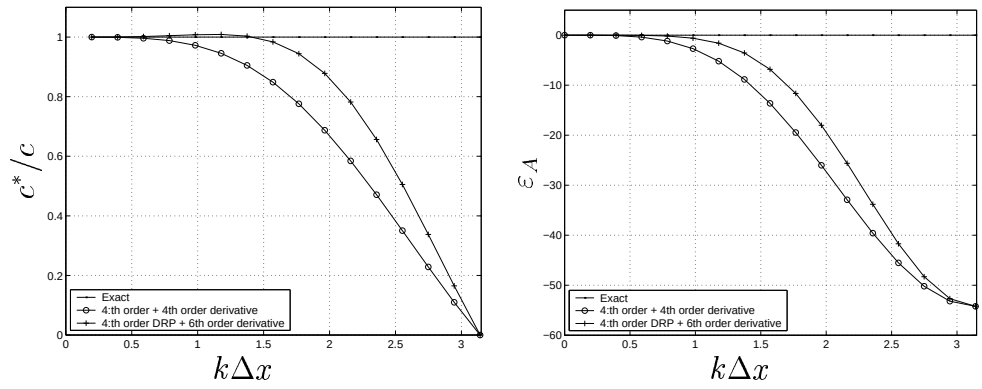


(a) Relative phase velocity

(b) Amplitude error

Figure 7.4: Relative phase velocity and amplitude error for full discretizations

where $\sigma$ is an arbitrary source. A four-stage 4:th order Runge-Kutta applied to this equation will be on the form

$$\begin{aligned} u_j^* &= u_j^n + \frac{1}{4}\Delta t A u_j^n + \Delta t f_1(\sigma) \\ u_j^{**} &= u_j^n + \frac{1}{3}\Delta t A u_j^* + \Delta t f_2(\sigma) \\ u_j^{***} &= u_j^n + \frac{1}{2}\Delta t A u_j^{**} + \Delta t f_3(\sigma) \\ u_j^{n+1} &= u_j^n + \Delta t A u_j^{***} + \Delta t f_4(\sigma) \end{aligned} \tag{7.42}$$

where $f(\sigma)$ is some linear combination of $\sigma$ evaluated at different times. Expanding the expression 7.42 and identifying the linear combinations to restore a 4:th order time marching scheme gives

$$\begin{aligned} u_j^{n+1} = &\left[1 + At + \frac{1}{2}A^2t^2 + \frac{1}{6}A^3t^3 + \frac{1}{24}A^4t^4\right] u_j^n \\ &+ \left[\frac{1}{6}\Delta t + \frac{1}{6}A(\Delta t)^2 + \frac{1}{12}A^2(\Delta t)^3 + \frac{1}{24}A^3(\Delta t)^4\right] \sigma^n \\ &+ \left[\frac{2}{3}\Delta t + \frac{1}{3}A(\Delta t)^2 + \frac{1}{12}A^2(\Delta t)^3\right] \sigma^{n+\frac{1}{2}} \\ &+ \frac{1}{6}\Delta t \sigma^{n+1} + \text{HOT} \end{aligned} \tag{7.43}$$

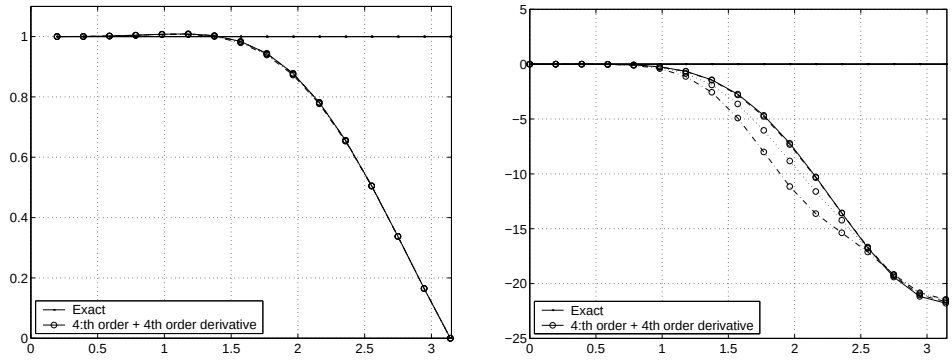


(a) Relative phase velocity (b) Amplitude error

Figure 7.5: Relative phase velocity and amplitude error for full discretizations. For CFL numbers equal to: solid: 0.1; dashed: 0.3; dotted: 0.5; dash-dotted: 0.6

or in terms of Runge-Kutta time marching

$$
\begin{aligned}
u_j^* &= u_j^n + \frac{1}{4}\Delta t A u_j^n + \frac{1}{4}\Delta t \sigma^n \\
u_j^{**} &= u_j^n + \frac{1}{3}\Delta t A u_j^* + \frac{1}{3}\Delta t \left(\frac{1}{2}\sigma^n + \frac{1}{2}\sigma^{n+\frac{1}{2}}\right) \\
u_j^{***} &= u_j^n + \frac{1}{2}\Delta t A u_j^{**} + \frac{1}{2}\Delta t \left(\frac{1}{3}\sigma^n + \frac{2}{3}\sigma^{n+\frac{1}{2}}\right) \\
u_j^{n+1} &= u_j^n + \Delta t A u_j^{***} + \frac{1}{6}\Delta t \left(\sigma^n + 4\sigma^{n+\frac{1}{2}} + \sigma^{n+1}\right)
\end{aligned}
\tag{7.44}
$$

By evaluating the source terms in the manner as in expression 7.44 the numerical accuracy of the time marching technique is restored to 4:th order. $\sigma$, $\sigma^{n+\frac{1}{2}}$ and $\sigma^{n+1}$ is the source evaluated at times $n$, $n+\frac{1}{2}$ and $n+1$, respectively.

## 7.3 Numerical Issues in Lighthill's Analogy

Lighthill's acoustic analogy on both time derivative and divergence formulation[59] have been implemented into the numerical code for the linearized Euler equations. In the present form the source terms are evaluated based on the synthesized velocity field in the SNGR method.

There has been identified a problem which can occur when using the time derivative (Lighthill-time) formulation of the Lighthill analogy. Besides the physical noise prediction which is based on the time-space distribution of sources in the method there can arise large amplitude high frequency noise when the integral is solved over a discretized grid.

In a 1D test case with a stagnant mean fluid the generated noise frequencies have been identified to relate to the cell size and the ambient speed of sound as

$$f_s = m\frac{c_0}{\Delta x} \tag{7.45}$$

where $m$ is any positive integer.

The cause of this spurious sound generation can be illustrated in figure 7.6. For simplicity, let's assume that the source term in the Lighthill equation is constant in space but a function of time. The constant space assumption will be lifted eventually but with the same conclusions as in the present example. For a source terms which varies

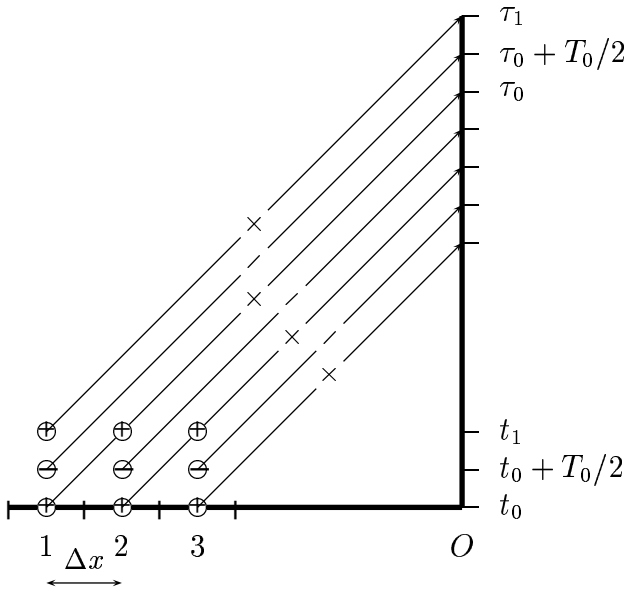


Figure 7.6: 1D case of forward time integration of Lighthill source. Source locations (cells) $1, 2, 3$ at times $t_0$ to $t_1$ and observer location $O$ at times $\tau_0$ to $\tau_1$.

with the frequency $f_s$ the peak positive value is said to occur at time $t_0$. After a time delay of $T_0/2$ the source will have a peak negative value

and after another time delay of $T_0/2$ the peak positive value is reached again. The forward time integration will from source location $1$ at time $t_0$ add a positive value to the far-field sound at time $\tau_0$ and a negative at time $t_0 + T_0/2$ to forward time $\tau + T_0/2$. The same contributions will be added from source location $2$ but shifted in time by $T_0/2$ and so on for each source location $3, 4, 5, ....$ The net result is that the far-field sound at frequency $f_s$ will be amplified by the coherence of the source distribution and similar amplification will occur for multiples of the first spurious frequency $f_s$. For lower frequencies than $f_s$ this amplification can not take place since there will be a canceling effect from the different source locations. This numerical phenomenon was illustrated with a constant source in space in order to simplify the analysis. For a source with finite spatial extent this amplification will of course be localized to a typical correlation length.

A numerical example of this is shown in figure 7.7. The Lighthill time formulation was integrated in a tube of $128$ cells oriented in the $x$-direction and the observer was located at $100$ tube lengths from the tube center point. The source was constant in space but consisted of filtered white noise as in equation 3.13. The spurious frequency for this case was $f_s = c_0/\Delta x = 341.56/(1/128) = 43720$ Hz and is clearly visible as the first sharp peak in the power spectrum in figure 7.7. Two higher modes are visible as well at frequencies $87440$ and $131160$ Hz. To compare this effect of amplification with a case where the effect is not present the far-field noise was recorded at a location $100$ tube lengths above the tube in the $y$-direction, see figure 7.8. In this case only the background noise from the response of the source terms is visible.

In a more general case with convection the first spurious frequency is a function not only on the ambient speed of sound but also on the local convection velocity. This also introduces directivity in the value of the spurious frequency. A simple estimation of the spurious frequency in a convected flow is

$$f_s = m\frac{(c_0 + \mathbf{u}\cdot\mathbf{n})}{|\Delta\mathbf{x}\cdot\mathbf{n}|} \tag{7.46}$$

The effect is that the spurious frequency is lower in the direction opposing the convection and higher in the direction of the convection.

It is obvious from this simple test that care has to be taken to ensure that the integrand in the analogy does not experience such high frequencies otherwise the noise prediction could be polluted by these spurious contaminant waves.

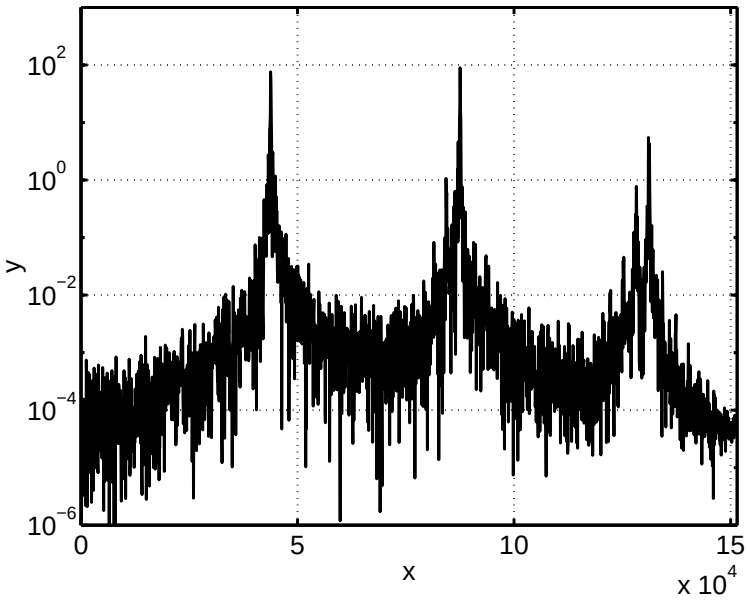


Figure 7.7: Power spectrum of far-field pressure. Observer location 100 units in the $x$-direction

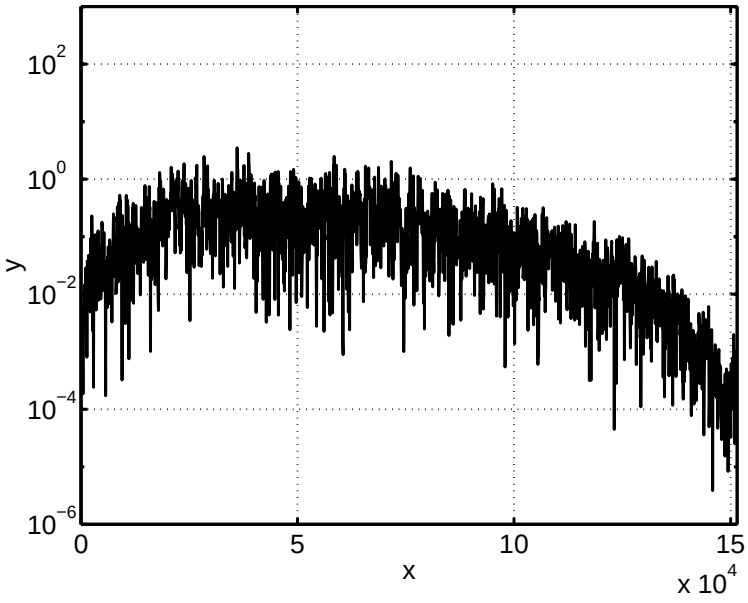


Figure 7.8: Power spectrum of far-field pressure. Observer location 100 units in the $y$-direction

## 7.4 Transformation of Solution to Characteristic Variables

For a locally homogeneous flow the linearized Euler equations can be written on the following quasi-linear form

$$\frac{\partial Q'}{\partial t} + \left(\frac{\partial E}{\partial Q}\right)_0 \frac{\partial Q'}{\partial x} + \left(\frac{\partial F}{\partial Q}\right)_0 \frac{\partial Q'}{\partial y} + \left(\frac{\partial G}{\partial Q}\right)_0 \frac{\partial Q'}{\partial z} = 0 \tag{7.47}$$

where the derivatives of $E$, $F$ and $G$ with respect to $Q$ are the flux Jacobian matrices evaluated at the reference solution $Q_0$. Consider a linear combination of the flux Jacobians in some direction $\mathbf{n} = (\alpha, \beta, \gamma)$ such that

$$\tilde{A}_0 = \alpha \left(\frac{\partial E}{\partial Q}\right)_0 + \beta \left(\frac{\partial F}{\partial Q}\right)_0 + \gamma \left(\frac{\partial G}{\partial Q}\right)_0 \tag{7.48}$$

Assuming that fluctuations are planar waves aligned with the vector $\mathbf{n}$ they are governed by a one-dimensional equation in the $\mathbf{n}$-direction.

$$\frac{\partial Q'}{\partial t} + \tilde{A}_0 \frac{\partial Q'}{\partial \xi} = 0 \tag{7.49}$$

where $\tilde{A}_0$ is defined as above and $\xi$ is the the spatial variable in the $\mathbf{n}$-direction. Equations 7.49 consists of five coupled equations. These cannot be solved independently without decoupling. This is done by introducing characteristic variables, $W$. Let

$$Q' = TW \qquad \text{where} \qquad W = \begin{bmatrix} W^{(1)} \\ W^{(2)} \\ W^{(3)} \\ W^{(4)} \\ W^{(5)} \end{bmatrix} \tag{7.50}$$

where $T$ and $T^{-1}$ are chosen to diagonalize $\tilde{A}_0$ according to

$$T^{-1}\tilde{A}_0 T = \Lambda = \text{diag}\left[\lambda^1, \lambda^2, \lambda^3, \lambda^4, \lambda^5\right] \tag{7.51}$$

Inserting the above relation into equation 7.49 gives

$$\frac{\partial W}{\partial t} + \Lambda \frac{\partial W}{\partial \xi} = 0 \tag{7.52}$$

Equations 7.52 are now decoupled and govern propagation of waves in the $\xi$-direction. The columns of the matrix $T$ are the eigenvectors to

the matrix $\tilde{A}_0$ and $\lambda^i$ are the corresponding eigenvalues. The eigenvalues are also called characteristic speeds. The characteristic speeds can be computed analytically and are given by

$$\begin{aligned} \lambda^1 = \lambda^2 = \lambda^3 &= \alpha\overline{u} + \beta\overline{v} + \gamma\overline{w} \\ \lambda^4 &= \alpha\overline{u} + \beta\overline{v} + \gamma\overline{w} + c\sqrt{\alpha^2 + \beta^2 + \gamma^2} \\ \lambda^5 &= \alpha\overline{u} + \beta\overline{v} + \gamma\overline{w} - c\sqrt{\alpha^2 + \beta^2 + \gamma^2} \end{aligned} \tag{7.53}$$

where $(\overline{u}, \overline{v}, \overline{w})$ is the local reference velocity vector. The sign of the characteristic speed $\lambda^i$ gives information about the direction the characteristic variable $W^{(i)}$ is traveling. A characteristic variable $W^{(i)}$ with characteristic speed $\lambda^i > 0$ is traveling in positive n-direction and vice versa.

The physical interpretation of the characteristic variables is

$$\begin{aligned} W^{(1)} &= \text{entropy wave} \\ W^{(2)}, W^{(3)} &= \text{vorticity waves} \\ W^{(4)}, W^{(5)} &= \text{acoustic waves} \end{aligned} \tag{7.54}$$

The solution can be transformed back to physical variables $Q'$ using equation 7.50. For more details on the characteristical variables, see Eriksson.[39]

## 7.5 Numerical Coefficients for FVM and FDM

A centered finite difference approximation of a volume-averaged first-order derivative can be written as

$$\left.\frac{\partial\overline{\phi}}{\partial x}\right|_i = \frac{1}{\Delta x}\sum_{l=-N}^{N} c_l\overline{\phi}_{i+l} \tag{7.55}$$

where the coefficients are defined as in figure 7.9. The finite volume approximation of the same volume-averaged first-order derivative is

$$\left.\frac{\partial\overline{\phi}}{\partial x}\right|_i = \frac{1}{\Delta x}\int_{x_{i-1/2}}^{x_{i+1/2}} \frac{\partial\phi}{\partial x}\mathrm{dx} = \frac{1}{\Delta x}\left(\phi_{i+1/2} - \phi_{i-1/2}\right) \tag{7.56}$$

$\phi_{i+1/2}$ and $\phi_{i-1/2}$ are point values (or face averages) of $\phi$ and the known degrees of freedom are the volume-averaged $\overline{\phi}$ in the cells. The estima-

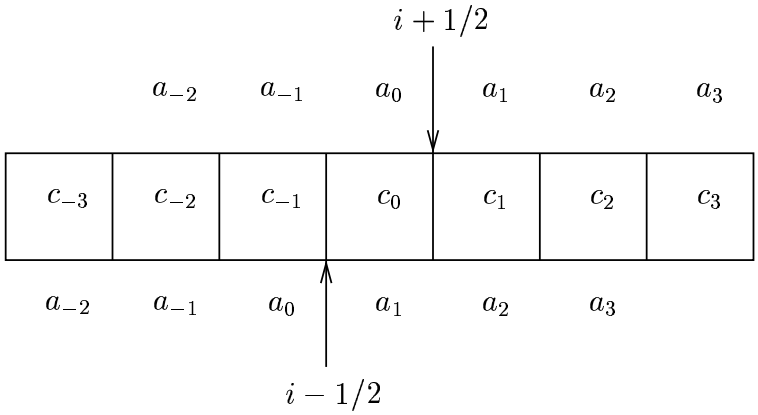


Figure 7.9: Definitions of coefficients.

tion of a face value must be given by the volume-averages and is given by

$$\phi_{i+1/2} = \sum_{l=-(N-1)}^{N} a_l \frac{1}{\Delta x} \int_{x_{i+l-1/2}}^{x_{i+l+1/2}} \phi \mathrm{dx} = \sum_{l=-(N-1)}^{N} a_l \overline{\phi}_{i+l} \tag{7.57}$$

Inserting equation 7.57 into equation 7.56 gives

$$\begin{aligned} \left.\frac{\partial \overline{\phi}}{\partial x}\right|_i &= \frac{1}{\Delta \mathrm{x}} \left( \sum_{l=-(N-1)}^{N} a_l \overline{\phi}_{i+l} - \sum_{l=-(N-1)}^{N} a_l \overline{\phi}_{i+l-1} \right) = \\ &\frac{1}{\Delta \mathrm{x}} \left( a_N \overline{\phi}_{i+N} + \sum_{l=-(N-1)}^{N-1} (a_l - a_{l+1}) \overline{\phi}_{i+l} - a_{-(N-1)} \overline{\phi}_{i-N+2} \right) \end{aligned} \tag{7.58}$$

By comparing equations 7.55 and 7.58 the following relation can be found between the finite difference and finite volume coefficients.

$$\begin{aligned} c_{-N} &= -a_{-(N-1)} \\ c_l &= a_l - a_{l+1} \qquad -(N-1) \leq l \leq (N-1) \\ c_N &= a_N \end{aligned} \tag{7.59}$$

Using the relations 7.59 the coefficients of a centered finite volume approximation $a_i$ can be transformed to coefficients of the corresponding finite difference approximation $c_i$ and vice versa.

The coefficients for a standard 4:th order approximation of a first-order derivative are given in table 7.1, and the coefficients for the 4:th order DRP scheme by Tam[41] are given in table 7.2.

| | | | |
|---|---|---|---|
| $c_2 = -c_{-2} =$ | $-\frac{1}{12}$ | $a_2 = a_{-1} =$ | $-\frac{1}{12}$ |
| $c_1 = -c_{-1} =$ | $\frac{8}{12}$ | $a_1 = a_0 =$ | $\frac{7}{12}$ |
| $c_0 =$ | 0 | | |

Table 7.1: Coefficients for 4:th order approximation of a first-order derivative. Left: finite difference scheme; Right: finite volume scheme

| | | | |
|---|---|---|---|
| $c_3 = -c_{-3} =$ | 0.02651995 | $a_3 = a_{-2} =$ | 0.02651995 |
| $c_2 = -c_{-2} =$ | −0.18941314 | $a_2 = a_{-1} =$ | −0.16289319 |
| $c_1 = -c_{-1} =$ | 0.79926643 | $a_1 = a_0 =$ | 0.63637324 |
| $c_0 =$ | 0 | | |

Table 7.2: Coefficients for 4:th order DRP approximation of a first-order derivative. Left: finite difference scheme; Right: finite volume scheme

The coefficients in table 7.3 relate to the addition of artificial numerical dissipation by the addition of a dissipative term to the system of equations, see Section 7.2.2. The coefficients for a central difference approximation of 4:th and 6:th order derivatives are given in table 7.3.

| | | | |
|---|---|---|---|
| $d_2 = d_{-2} =$ | 1 | $d_3 = d_{-3} =$ | −1 |
| $d_1 = d_{-1} =$ | −4 | $d_2 = d_{-2} =$ | 6 |
| $d_0 =$ | 6 | $d_1 = d_{-1} =$ | −15 |
| | | $d_0 =$ | 20 |

Table 7.3: Coefficients for central difference approximations. Left: 4:th order derivative; Right: 6:th order derivative.